



-

Mustafa Abdullah Hilal
University Of Baghdad

Zaid Jamel Musa AL-Najar
University Of AL- Kufa

.()

Comparison Study between Iraqi Conditions of Contract and FIDIC Conditions- The Red Book

Abstract

Reconstruction in Iraq requires coherent legitimate frameworks that are able to detail obligations, rights and responsibilities of the parties participating in reconstruction projects, regardless their type or delivery system. Conditions of Contract can be considered an important component of these frameworks. This paper investigates flexibility and appropriateness of the application of Iraqi conditions of contract in reconstruction projects. These conditions were compared to FIDIC Conditions. The objective wasn't comparing individual clauses, but rather exploring the principles and philosophy laying behind each conditions, and to what extent each conditions care about realizing equity between main contract parties. Validity of application on various project delivery systems was also investigated. The structure of Iraqi and FIDIC conditions were compared to determine how the efficiency of use will be effected by the layout, presentation, organization, and detailing of the contents of each conditions. Moreover, some clauses related to the project parties were compared in order to further illustrate the disparity in efficiency of each conditions. The paper concludes that Iraqi conditions of contract in its current state was, and will continue, hindering the reconstruction efforts in Iraq, as well as being a cause of money waste and bad quality of project outputs.

"

"

-

-:

-

.

-

.

-

.

.

-

.

-

[2008]

-:

-

"

-

"

.

-

()

: 1999

Conditions of Contract for Construction for
Building and Engineering Works Designed by
the Employer

-

.

(Delivery Systems)

(Design/Build) /

(Turnkey)

1995

/

:

[05 Overview]

" " " " " "

1999

1913

-.[FIDIC 1999 a]

-1

)

)

.(

.(

Conditions of Contract for
Construction for Building and
Engineering Works Designed by the
Employer (Red Book).

1957

-2

[Shnookal 2010]

/

(ICE 4th edition)

.1955

)

.(

Conditions of Contract for Plant and
Design/Build Contract (Yellow Book).

-3

1963

1987

)

:

.(

-1

Conditions of Contract for EPC/Turnkey
Projects (Silver Book).

.(

/

)

-2

-4

/

)

.(

)

.(

Short Form of Contract (Green Book).

11 11

• • •

11 11

2005

)

(

"Conditions of Contract for Construction for Building and Engineering Works Designed by the Employer- Multilateral Development Banks (MDB) Harmonized Edition"

.2010

2008

// //

[FIDIC Bookshop (Standard Practices)]

.2010]

MDB Harmonized)

.(Addition

1

/

1987

1972



[2008]

.(Institution of Civil Engineers)

1987

) 1999
.(

68 57

-1999

[2010]

" " " " " " " " " " " "

-1999

1999

[Wade 2005]

"

"

(4.4)

(-4.4)

"

1999

"

-4.4)

(-4.4) (

-4.4) (-4.4)

(

%0.01

1999



" "

"

"

!

•

..

"

"

"

"

•

"

"

(-1)

"

"

"

"

"

"

"

"

III

11

•

—

: (11-8)

(14.8)

.. 84

-1

28

-2

(13)

-3

(2-16)

$$.(-1)$$

II

Delivery]

[Systems



(/)
" .(

" [Wade 2005]

- / 1995
.()

[Project Delivery System]

/

./

- !

/

..

- 1999

/

"

."

-

2008

..

/ /

(Design/Bid/Build) / /

/ /

.(BOT)

.. ..

.

)



-

()

-

-

"

"

-:

-1)

:

.(

-

(1999)

()

-

(72)

" (Lump Sum) "

(Cost Plus Percentage/fee) " /

(20)

-

-:

. (12) -

. (8) -

. (9) -

. (58)

. (17)

-

-

" "

(1)

-

-

-

.

-

-

•

-:

:

(10)

(10)

()

(9)

" "

.

(5.2)

)

(-

.(3.2)

.

-

:

(1999)

" " " "

[Bunni (-3.1) 2005]

(3.5)

" "

[Bateson 2000]



✓

✓

✓

✓

✓

/

✓

1999

/ /

✓

" .(2008)

(1

✓

"

" .(2008)

(2

"

" .(2010)

(3

✓

28

"2007

.157-140

5

- 10) FIDIC (International Federation for Consultant Engineers) (1999c). "Conditions of Contracts for EPC/Turnkey Projects". Switzerland. (4)
- 11) FIDIC Bookshop (2010). POBox 86, CH-1000 Lausanne 12, Switzerland. (5)
<http://www.fidic.org>
- 12) Shnookal, T., (2010). "Standard Form Contracting: The Role for FIDIC Contracts Domestically and Internationally". Proceedings of the Society Law conference, 30ps.
- 13) Wade, C., (2005). "An Overview of FIDIC Contracts". Proceedings of International Construction Contracts and Dispute Resolution ICC-FIDIC, Cairo, Egypt, 9 ps.
- 14) Nobbs, R., and Masons, P., (2004). "The NEC Engineering and Construction Contract- Some Issues for the 3rd Edition". Captured on March 25th, 2010 from:
http://www1.fidic.org/resources/contracts/ibc_feb2004/nobs_feb04.asp
- 6) Bateson, D., (2000). "FIDIC- New 1999 Edition of Red Book: Impartiality of the Engineer". Captured on July, 8th, 2010 from:
http://www1.fidic.org/resources/contracts/bateson_aug00.asp
- 7) Bunni, N., (2005). "The FIDIC Forms of Contract" 3rd Ed., Blackwell Publishing, UK.
- 8) FIDIC (International Federation for Consultant Engineers) (1999a). "Conditions of Contract for Construction for Building and Engineering Works Designed by the Employer". Switzerland.
- 9) FIDIC (International Federation for Consultant Engineers) (1999b). "Conditions of Contracts for Plant and Design-Build". Switzerland.



(1)

(-1)	1.1.4.1		(-1)	1.1.1.1	
	1.1.4.2			1.1.1.2	
	1.1.4.3			1.1.1.3	
	1.1.4.4			1.1.1.4	
	1.1.4.5		(-1)	1.1.1.5	
(9)	1.1.4.6		(-1)	1.1.1.6	
(62)	1.1.4.7			1.1.1.7	
	1.1.4.8			1.1.1.8	
(62)	1.1.4.9			1.1.1.9	
(59)	1.1.4.10		(-1)	1.1.1.10	
(62)	1.1.4.11			1.1.2.1	
(62)	1.1.4.12		(-1)	1.1.2.2	
(-1)	1.1.5.1		(-1)	1.1.2.3	
	1.1.5.2		(-1)	1.1.2.4	
	1.1.5.3		(15)	1.1.2.5	
(-1)	1.1.5.4			1.1.2.6	
	1.1.5.5		(35)	1.1.2.7	
(-1)	1.1.5.6		(-1)	1.1.2.8	
(-1)	1.1.5.7		(69)	1.1.2.9	
(-1)	1.1.5.8			1.1.2.10	
	1.1.6.1			1.1.3.1	
	1.1.6.2		(42)	1.1.3.2	
	1.1.6.3		(-1)	1.1.3.3	
(2- 20)	1.1.6.4			1.1.3.4	
	1.1.6.5		(49)	1.1.3.5	
(10)	1.1.6.6			1.1.3.6	
(-1)	1.1.6.7		(50)	1.1.3.7	
(12)	1.1.6.8		(1 64)	1.1.3.8	
(52)	1.1.6.9			1.1.3.9	

Implementation of Digital Image processing in Calculating Normal Approach for Spherical Indenter Considering Elastic/Plastic Contact

Rana Abdul Rahman Lateef
Baghdad college of economics
Science university
Dep. Of computer science

and

Ahmed Abdul Hussein
university of Baghdad
mech. engineering department

Abstract:

In this work a study and calculation of the normal approach between two bodies, spherical and rough flat surface, had been conducted by the aid of image processing technique. Four kinds of metals of different work hardening index had been used as a surface specimens and by capturing images of resolution of 0.006565 mm/pixel a good estimate of the normal approach may be obtained the compression tests had been done in strength of material laboratory in mechanical engineering department, a Monsanto tensometer had been used to conduct the indentation tests.

A light section measuring equipment microscope BK 70x50 was used to calculate the surface parameters of the texture profile like standard deviation of asperity peak heights, centre line average, asperity density and the radius of asperities.

A Gaussian distribution of asperity peak height was assumed in calculating the theoretical value of the normal approach in the elastic and plastic regions and where compared with those obtained experimentally to verify the obtained results.

الخلاصة:

في هذا البحث تم دراسة التقارب العمودي بين جسمين ، كروي وسطح مستوي خشن، باستخدام تقنية المعالجة الصورية . أربع انواع من المعادن استخدمت كل منها له معامل تصليد بالتشغيل مختلف عن الآخر لأجل استخدامها كعينات سطوح، ومن خلال ألتقاط صور بدقة 0.006565 ملم لكل نقطة ضوئية (pixel) يمكن حساب التقارب العمودي بدقه مقبولة. اختبار الضغط تم اجراءه في مختبر مقاومة المواد في قسم الهندسه الميكانيكيه وباستخدام جهاز (tenso-meter Monsanto) تم اجراء فحص الخرق .

أستخدم جهاز ميكروسكوب قياس الأسقاط المقطعي (BK.70X50) في ايجاد متغيرات ومواصفات السطح مثل الانحراف المعياري لأرتفاعات النتوءات ومعدل الخط المركزي وكثافة النتوءات وكذلك أنصاف أقطارها .

تم افتراض التوزيع العشوائي لأرتفاع النتوءات في أحتساب القيم النظرية للتقارب العمودي في منطقتي المرونه واللدونه وتمت مقارنتها مع تلك المحسوبه عملياً.

Introduction:

Digital image correlation (DIC) is a non-contacting measuring technique that has been developed to obtain full field surface displacements and their gradients (strains) of objects under stress. The DIC method has evolved over the last decade and its usefulness for measuring small displacements as occurs in engineering materials in tension and compression has been demonstrated by several investigators. The theory of digital image correlation has been described in detail by several researchers but a detailed treatment of the subject can be found in Sutton et al., 1983 the underlying principle of DIC and its application to obtain displacement fields can be found in Samarasinghe and Kvasiri, 2000.

All surfaces are microscopically rough. Therefore when two surfaces are in contact the load is borne by the discrete spots at the tip of surface asperities and the real contact area is only a small function of the apparent contact area.

The phenomena of contact surfaces are of fundamental importance in the study of tribology and other applications [Halling, J and Nuri.K.A 1988]. Therefore there have been numerous efforts to relate surface roughness to the stresses and deformation when two surfaces are pressed together. The Hertz elastic contact mechanics governs the deformation of each asperity. An experimental study conducted by Powierza et al. 1992 verified the theoretical results of the Greenwood

model for elastic deformation and for isotropic surfaces. However, when there are substantial amount of asperities deformed plastically the theoretical results deviate distinctly from the experimental data.

Several investigations have been conducted to deal with the plastic deformation of asperities Pullen and Williamson 1972 showed that for the plastic deformation of asperities, volume is conserved by a uniform rise in the non-contacting part of the surface. Results from finite element analysis performed by Kucharski et al. 1994 for an asperity with elasto-plastic deformation agree well with the observation of Pullen and Williamson. Zhao et al. 2000 proposed a model that considers the continuity and smoothness of variables across different modes of deformation. Their results show that this model is more complete in describing the contact of rough surfaces and is consistent with experimental observation and physical intuition.

The deformational models deal with rough surfaces with isotropic contacts. However rough surfaces can have elliptical contacts because engineering surfaces have asperities with various curvatures for various directions.

The present study propose a spherical micro contact model taking in account the elastic, elsto-plastic and fully plastic deformation.

In the proposed model, every asperity is assumed to have the same radii just as Greenwood model like many other models which assume that all asperities are circular. The proposed model is useful for surface with a pronounced grain in one direction.

Analysis Based on Constant Indenter Radius

It is necessary to define the normal approach of a sphere to the normal load and the consequent deformation, considering the contact of a sphere and a plane, fig.1.

It is easily seen that the separation u of the surfaces at a distance r from the centre of the contact zone is given by

$$u = R - (R^2 - r^2)^{1/2} = R - R \left(1 - \frac{r^2}{R^2}\right)^{1/2}$$

If r is small compared to R then

$$u = \frac{r^2}{2R}$$

If a is the radius of the contact zone and w is the displacement of the sphere at the boundary of this zone then the normal approach δ will be given by

$$\delta = u + w = \frac{a^2}{2R} + w$$

At the center of the contact zone δ is given by the degree of deformation and it is therefore reasonable to assume that the normal approach will be proportional to the flattening of the sphere. In other words

$$\delta \propto \frac{a^2}{R}$$

From the results given by Hertzian contact [Halling J. 1975]

$$a \propto \left(\frac{NR}{\bar{E}}\right)^{1/3} \text{ or } a = \left(\frac{3NR}{4\bar{E}}\right)^{1/3}$$

$$\text{Where } \frac{1}{\bar{E}} = \frac{1-\nu_1^2}{E_1} + \frac{1-\nu_2^2}{E_2}$$

$$\text{So that } \delta \propto \left(\frac{N^2}{E^2 R}\right)^{1/3}$$

The exact result show that [Halling J. 1975]

$$\delta = \left(\frac{9N^2}{16E^2 R}\right)^{1/3}$$

$$\text{Or } N = \frac{4}{3} \bar{E} R^{1/2} \delta^{3/2}$$

The area of contact, A , will be given by

$$A = \pi a^2 = \pi R \delta$$

The theoretical analysis employed in the present work for determining the load-normal approach relationship of a sphere in contact with a rough plane is based on the model shape of the rough surface as shown in fig.2.

In this figure the flat surface is considered to be covered with similar asperities having randomly varying heights. The chosen asperity peak heights form a small sample from a large population of a random deviate following the Gaussian distribution about a mean plane, and the asperities are assumed to be spherical caps all with the same radius.

The elastic deformation of the surfaces will be neglected and the asperities will be assumed to deform with ideal plastic mode under a constant flow pressure. Each individual load will be taken as a point force acting on a semi-infinite plane and the collective effect of these forces is then considered

We shall use the results which ensue from the contact of a sphere of a material having a stress strain behavior of the form

$$\bar{\sigma} = B \bar{\epsilon}^n \quad (1)$$

Where $\bar{\sigma}$ and $\bar{\epsilon}$ are the effective stress and strain values based on the assumption that the strain ratios are constant and that the principal axes do not rotate. This is admissible for spherical contacts if we assume a geometrical similarity of contact with its scale being defined simply by the size of the contact radius. Thus, [William F. Hosford 1983]

$$\bar{\sigma} = \left[\frac{1}{2} (\sigma_1 - \sigma_2)^2 + (\sigma_2 - \sigma_1)^2 + (\sigma_3 - \sigma_1)^2 \right]^{1/2} \quad (2)$$

$$\bar{\epsilon} = \frac{1}{3} [2 (\epsilon_1 - \epsilon_2)^2 + (\epsilon_2 - \epsilon_3)^2 + (\epsilon_3 - \epsilon_1)^2]^{1/2} \quad (3)$$

It is apparent that the $\bar{\sigma}$ is the yield stress in simple tension and that when $n=0$ the material behaves in a perfectly plastic fashion and B is the constant yield stress, Y . When $n=1$ the behavior may be considered as perfectly elastic and $B = E/(1 + \nu)$.

For the contact of a material defined by eq. (1) with a rigid sphere of the same size we shall assume that $\bar{\sigma}$ is a linear function of the contact pressure, thus.

$$\bar{\sigma} = \frac{1}{c} \frac{p}{\pi a^2} \quad (4)$$

Where p is the load, a is the radius of the contact zone and c is a constant. For

metals it is known that c has a value of about 2.8 being the relation between the current yield stress and the current hardness of the material, see fig.3. [Halling J. 1975]

The strain must be some function of a/β where β is the radius of the sphere. Expanding such a function as a power series and, since $\beta \gg a$, neglecting all but the first term gives,

$$\bar{\epsilon} = D \frac{a}{\beta} \quad (5)$$

Where D is some unknown constant. Combining eqn. (1), (4) and (5) yields

$$P \beta_{1/2}^n = K a^{(2+n)} \quad (6)$$

$$\frac{K}{B} = \pi c D^n \quad (7)$$

We would therefore anticipate that K/B would be a constant for a given material characteristic n . Known solutions to eqn. (6) are the elastic case when $n=1$ and $K_e = 4/3 \dot{E}$ where, $1/E' = (1 - \nu^2)/E$

And the perfectly plastic case when $n=0$ and $K_p = \pi H$ where H is the indentation hardness of the material. Equation (5) may now be written,

$$\bar{\epsilon} = \left(\frac{K}{\pi B c} \right)^{1/n} \left(\frac{a}{\beta} \right) \quad (8)$$

Finally we shall be interested in the normal approach δ of a loaded sphere so that we shall assume a relationship of the form,

$$a^2 = \lambda \beta \delta \quad (9)$$

Since we know that $\lambda = 1$ for the elastic case when $n=1$ and $\lambda = 2$ for the perfectly plastic case when $n=0$. Equation (8) may be written in the more useful form.

$$\bar{\epsilon} = \left(\frac{K}{\pi B c} \right)^{1/n} \left(\frac{\lambda \delta}{\beta} \right)^{1/2} \quad (10)$$

In the foregoing sequence of equations we note that we require a knowledge of such constant as c, B, n, K and λ . These constants are determined in ref. [Halling J. 1975] and from those results may obtain the empirical relationship

$$\frac{K}{B} = \pi \cdot c (1 - 0.9n)$$

$$\text{Or } D = \frac{K}{\pi B c} = (1 - 0.9n) \quad (11)$$

The variation of λ for materials with various values of n may be obtained from the empirical expression mentioned in ref. [Halling J. 1975] which is shown in fig.5 [Halling J. 1975].

$$\lambda = 2 - n^{1/2} \quad (12)$$

The Contact of Rough Surfaces

Consider a surface containing a point distribution of rigid spherical asperities against a rough surface consisting of an array of spherical asperities of a material defined by eq.(1). All the asperities are assumed to be spherical of radius β and it is tacitly assumed that an asperity on the upper surface is aligned with each asperity on the rough surface,

Fig. (2). Following the arguments used by Greenwood and Williamson, but using the foregoing results we may define each discrete area of contact A_i as, [Powierza Z.H. et.al. 1992]

$$A_i = \lambda \pi R \delta = \pi a^2 \quad (13)$$

Using eqns(6) and (9) defines the load at any contact as

$$P_i = K \lambda^{(1+\frac{n}{2})} \delta^{(1+\frac{n}{2})} \beta^{1-\frac{n}{2}} \quad (14)$$

Let the surfaces be separated by a distance d at any total load P where d is measured from some datum in the rough surface to the tips of the rigid spherical asperities. For any contacting asperity on the rough surface of initial height z above the datum the normal approach will be $= z - d$. The probability of contact for any asperity of height z is,

$$\text{prob.}(z > d) = \int_d^\infty \phi(z) \cdot dz \quad (15)$$

Where $\Phi(z)$ is the probability function of the heights and the number of asperity contacts will be,

$$N \int_d^\infty \Phi(z) dz \quad (16)$$

N being the total number of asperities within the contact region. The total real area of contact A and the total load P thus become. [Nuri K.A. 1974]

$$A = \lambda \pi \beta N \int_d^\infty (z - d) \Phi(z) dz \quad (17)$$

$$P = K \lambda^{1+\frac{n}{2}} \beta^{1-\frac{n}{2}} N \int_a^{\infty} (z-d)^{1+\frac{n}{2}} \Phi(Z) dz \quad (18)$$

Equation (17) and (18) reduce to the well known solution for the spherical case of $n=0$ and $n=1$, i.e. perfectly plastic or perfectly elastic contact.

Point Detection in Image Processing:

Digital image detection is a measuring technique has been used to obtain full field surface displacements. This is done by applying two white points on the specimens under test and applying the point detection technique on the image of interest, according to this a distance or a displacement between these two points are calculated using Euclidean distance between two n-dimensional (row or column) vector x and y to evaluate the normal approach between the spherical smooth surface and rough flat surface.

In this work, an image with size (2700 × 2300) pixel JPEG format has been captured by a Ginex CCD (charge Couple Device) video camera and a lens with ×8 magnifications.

A calibration process has been done to estimate the precision of the measurement by capturing picture for bodies with defined dimension.

The result shows that a precision of 152 pixels per 1 mm have been achieved, this equals to 0.006565 mm/pixel.

Experimental Procedure:

Four kinds of test metals had been used in this work namely steel ck45,

Aluminum and two types of Brass. Their chemical composition analysis is given in table (1).

The test specimens were polished with emery paper having different grades 200,400 and 600 to have their surfaces smooth, those specimens where fully annealed in an oven under the temperature of 650C⁰ for steel , 550C⁰ for Brass and 400C⁰ for Aluminum for about 1.5 hour. The specimens were kept in the oven for one day to cool down slowly and evenly to room temperature. The annealing process had been done in the mechanical engineering laboratory for metals.

A Monsanto tensometer had been used where a hand driven gear box of high mechanical advantage applies a force of up to 20kN to the test piece. The tensometer can be used for compression and indentation tests simply by using the compression cage shown in fig (6)

Precision alignment enables the dies used for the compression to be mounted directly to the tables of the compression cage.

For many ductile metals which have not been cold worked prior to the tensile test (i.e. that are fully annealed) the behavior from initial yield to ultimate load is adequately described by an expression of the form [William F. Hosford 1983]

$$\sigma = B \epsilon^n \quad (19)$$

Where for an induced strain ϵ , the corresponding value of σ is the new yield strength caused by the degree of

cold working that induced the strain . The tensile results are, in fact, descriptive of an effective stress-strain plot. For that reason eq(19) can be written as

$$\bar{\sigma} = B\bar{\epsilon}^n \quad (20)$$

The numerical values of B and n are determined in ref. [Ahmed A.A. 1993] where the same test specimens had been used in this work. The following relation ships were found to correlate with the experimental results

Steel ck 45 $\bar{\sigma} = 2387.76 \bar{\epsilon}^{0.73085}$

Brass1

$$\bar{\sigma} = 691.498576 \bar{\epsilon}^{0.43764}$$

Brass 2

$$\bar{\sigma} = 545.8925 \bar{\epsilon}^{0.5336}$$

Aluminum

$$\bar{\sigma} = 184.7311 \bar{\epsilon}^{0.25456}$$

Alight section measuring equipment (microscope BK70X50) shown in fig. (7) had been used to measure tip heights of asperities for the specimens under test. The BK 70x50 measuring microscope operates on the basis of Pof-schamaltz light section method. A thin light strip is brought to section at 45° with the horizontally arranged surface to be measured so that the generated profile of intersection between light strip and surface to be checked becomes visible, the visible light strip had been captured using digital camera with a resolution of 7 megapixel a sample of this picture are shown in fig. (8)

Lenses of magnification of 30x12.5 had been used in BK 70x50 microscope

which enable to capture photos with precession of 0.00004347 mm/pixel and with lenses of 60x12.5 a precession of 0.0000224 mm/pixel may be achieved . The first set of lenses had been used to study the surface texture height and distribution while the second set of lenses is used to calculate the radios of asperities for the various test specimens surfaces.

A Hough transform method for edge detecting and linking had been applied on images obtained from microscope BK 70x50, to detect the tips and valleys of the rough surface in the test specimens.

A Hough transform in this work used to detect curves or peaks. Because of the quantization in space of the digital images, the quantization in parameter space of Hough transform as well as the fact that edges in typical images are not perfectly straight. Hough transform peaks tend to lie in more than Hough transform cell.

The algorithm or the strategy is as follows:

- 1- Find the Hough transform cell containing the highest value and record its location.
- 2- Suppress (set to zero) Hough transforms cells in the immediate neighborhood of the maximum found in step 1.
- 3- Repeat until the desired number of peaks has been found, or until a specified threshold has been reached.

Once a set of candidate peaks has been identified in Hough transform, it remains to be determined if there are line segments associated with those peaks, as well as where they start and end. For each peak, the first step is to find the location of all nonzero pixels in the image that contributed to that peak.

As the pixels associated with the location found it must be grouped into line segments with the following steps:

- 1- Rotate the pixel locations by 90° so that they lie approximately along a vertical line.
- 2- Sort the pixel location by their rotated X-values.
- 3- Merging adjacent line segments. That is separated by a small space.

The procedure for obtaining the normal approach in this work experimentally is based on taking several images for the two approaching bodies (spherical and specimen) using LCD camera for each step of loading with a resolution of 0.006565mm/pixel and by calculating the distance between two specific points one on the specimen and the other on the spherical indenter, for each loading case, the normal approach between the approaching bodies may be specified.

Calculating the normal approach is based on the application of Euclidean distance between two points which is defined as [Gonzalez R. C. 2008]

$$D_s(p, q) = [(x - s)^2 + (y - t)^2]^{1/2}$$

Where (x, y) are the coordinates of the two pixels p and q so, by taking arbitrary two points each of lies on one of the approaching bodies the distance between these points are calculated using the equation mentioned above.

The distance between those points in the first image for the case of no load is compared with the other cases for the step loading and the difference between the distances for each step of loading is compared with the first case of no load. A typical kind of the images used in calculating the normal approach is shown in fig.(9)

Results and Discussion:

From the analyzed images of the four test specimens may obtain the parameters shown in table 2 which are used in calculating the theoretical relation between the applied load and deformation (normal approach) which were used for comparison with the experimental results. A Gaussian distribution of asperity heights had been assumed in plotting theoretical curves with a limit of 3σ , those curves are shown in figs.(10-17). Two steel balls of diameter 10mm and 5mm had been used in the indentation tests for calculating normal approach the results of tests for the four kinds of metals used are shown as crosses in figures (10-17).

In figs. (10-17) the normal approach for 5mm diameter spherical indenter is bigger than for 10mm diameter sphere having the same load, this is due to the high pressure at the contact zone which causes deformation of asperities.

Metals that have low work hardening index, like aluminum, deforms plastically compared with those having higher work hardening index, like steel, at the same load as shown in fig.(10-17) where the normal approach decreases while the work hardening index increases for the same load.

Surfaces having a high center line average (C.L.A.) of asperity height and high standard deviation of all ordinate height deformed more than those having lower C.L.A. and lower standard deviation as shown when comparing between fig.(12) and fig.(14) for 10mm diameter indenter and between fig.(13) and fig.(15) for 5mm diameter indenter

Conclusions:

Experimental results seems to lie between the theoretical curves of elastic and plastic regions even though the load applied is higher than the load needed for plastic deformation which means that the theoretical analysis for predicting the normal approach did not conform the experimental results. These results agree with the work of Powerza et.al. 1992 where in their experimental study they showed that when there are substantial amount of asperities deformed plastically the theoretical results deviate distinctly from experimental data.

The predicted theoretical elastic and plastic region limits depend on the assumed kind of distribution of asperity height which is assumed here as Gaussian distribution, this assumption plays a big rule in the deviation of the experimental results from the bands of

elastic and plastic limits although most of the experimental results at high loads lie within those bands.

References:

- Ahmed A.A. "Contact mechanics of rough engineering surfaces" a thesis submitted to the college of engineering university of Baghdad 1993.
- Halling J., and Nuri K.A. 1988, "the elastic – plastic contact of rough surfaces and its relevance in the study of wear" Proc. Inst. Mech. Eng. Part c; J. Mech. Eng. Sci., 202(c4)pp. 269-274.
- Halling J. "A contribution to the theory of mechanical wear" 1975, wear, 34, pp239-249.
- Halling J. "Principles of tribology" 1975, Macmillan press LTD.
- Kucharski S., Kilmezak T., Palijanink J. and Kaczmarck J., 1994 "Finite element model for the contact of rough surfaces." Wear 177, pp1-13.
- Nuri K.A., 1974, "The normal approach between curved surfaces in contact" Wear, 30, pp.321-335.
- Powierza Z.H., Klimezak T., and Polijanink A., 1992, "On the experimental verification of the Greenwood-Williamson model for the contact of rough surface" Wear, 154, pp. 115-124.
- Pullen J., and Williamson J.B.P., 1972 "On the plastic

of rough surface” Proc. R. Soc. London Ser. A: A327 pp159-173.

Rafael C. Gonzalez , Richard E. Woods and Steven L. Eddins“digital image processing using Matlab” 2004, Pearson international edition.

Rafael C. Gonzalez and Richard E. Woods “digital image processing” 2008, Pearson international edition, third edition.

Samarasinghe S., & Kvaslari,G.D. 2000, displacement fields of wood in tension based on image processing . Silva Fennica 34(3);251-273.

Sutton , M.A., Wolters , W.J., Peters, W.H., Rawson , W.F. & Mc Neill, S.R., 1983, Determination of displacements using an improved digital image correlation method. Image and vision computing 1(3); 133-139.

William F. Hosford and Robert M. Caddel “ Metal forming mechanics and metallurgy” 1983,Prentice-Hall, Inc., Englewood Cliffs
Zhao Y., Maletia D.M. , and Chi I. , 2000 “ An asperity micro contact model incorporating the transition from elastic deformation to fully plastic flow.”ASME, J., Tribol., 122(1),pp.86-93.

Nomenclatures

symbol	definition	units
u	Separation of the surfaces	mm
a	Radius of contact zone	mm
R	Radius of sphere	mm
δ	Normal approach	mm
A	Area of contact	Mm ²
β	Radius of asperity	mm
$\bar{\sigma}$	Effective stress	N/mm ²
$\bar{\epsilon}$	Effective strain	-
n	Work hardening index	-
p	load	N
ν	Poisons ratio	-
λ	Area factor	-
$\Phi(z)$	Probability function of height distribution	-
N	Total number of asperities within the contact zone	-

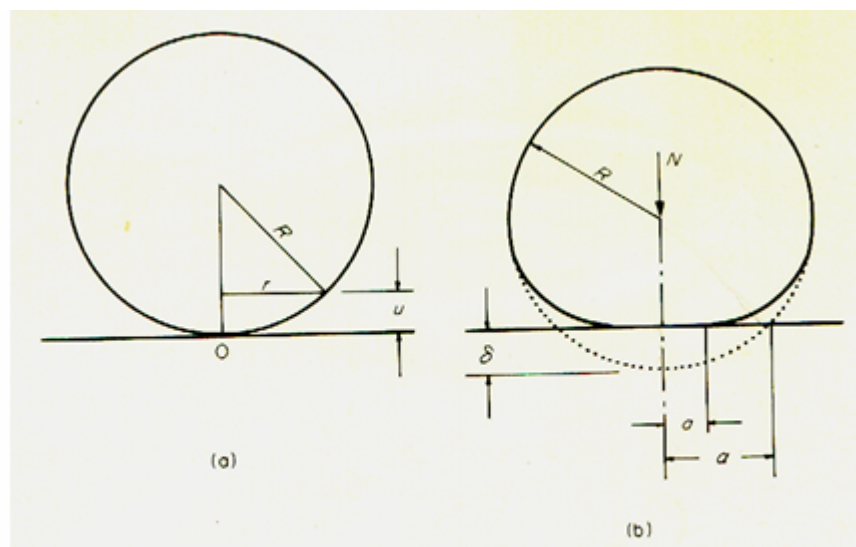


Table(1) chemical composition analysis of test specimens

Comp.	Steel ck45	Aluminum	Brass 1	Brass 2
C	0.42-0.5			
Si	0.15-0.35	0.235		
Mn	0.5-0.8	0.007		0.012
P	<0.035			
S	<0.035			
Cr				0.004
Fe	Remainder	0.174	0.021	2.333
Zn		0.008	0.192	26.31
Pb		0.003	21.69	
Mg		0.444		
Cu		0.013	remainder	69.45
Ni			0.351	0.069
Al		remainder		

Table(2) surface parameters obtained by image processing analysis

	Aluminum	Brass 1	Brass 2	Steel ck45
Density η asp./mm ²	255.178	399.408	175.78	285.714
Standard deviation of all height $\sigma \times 10^{-3}$ mm	5.617	7.75	2.079	3.812
Radius of asperities $\beta \times 10^{-3}$ mm	2.402	0.6207	1.741	0.5703
Center line average C.L.A. $\times 10^{-3}$	4.56978	5.71246	1.55	3.21147



Fig(1) Elastic contact between a sphere and a plane [Halling J. 1975]

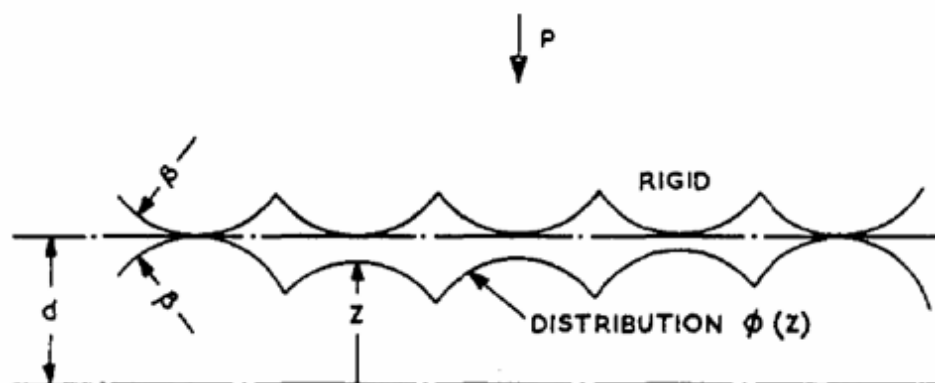


Fig.(2) Normal contact of rough surfaces.

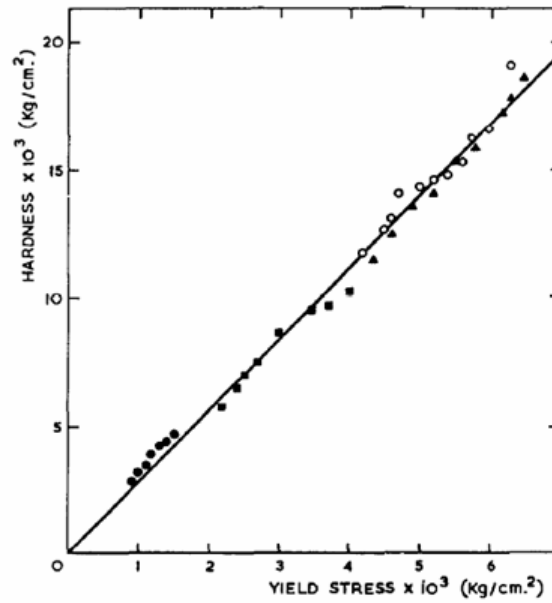
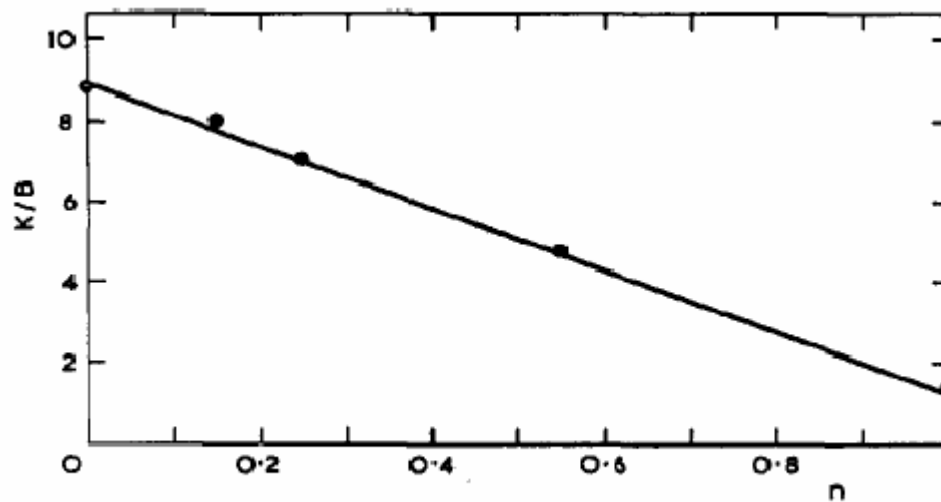


Fig.(3) Variation of the hardness with yield stress for various metals, \circ aluminum,

\blacksquare copper, \diamond brass, \triangle mild steel



Fig(4) Variation of K/B with degree of work hardening [3]

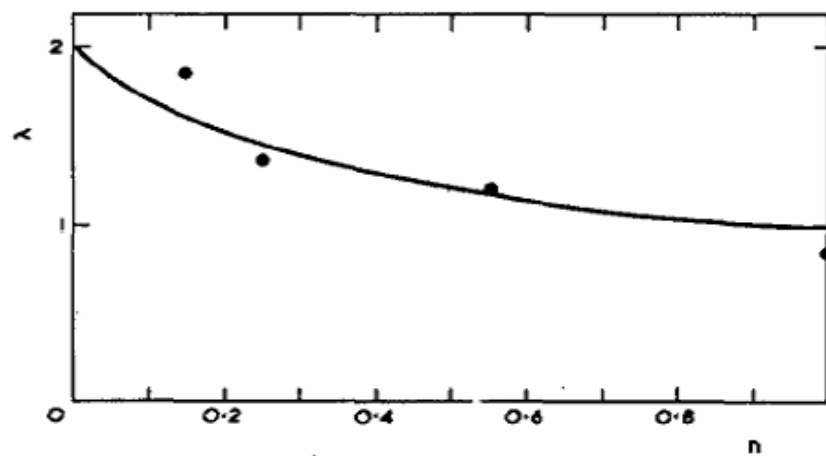
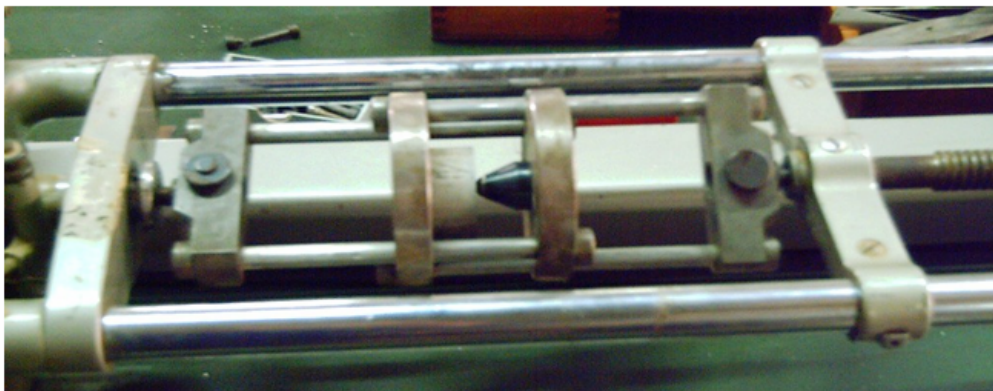


Fig.(5) Variation of the area factor with degree of work hardening. [3]



Fig(6) Monsanto tensometer and its compression cage.



Fig.(7) Light section measuring equipment (Microscope BK 70x50)



Fig.(8) Profile for Aluminum specimen magnified 375 times by microscope BK 70x50



Fig(9) Image for compression of a spherical indenter of diameter 10mm on a steel specimen to calculate the normal approach, image size 2976x2232 pixels.

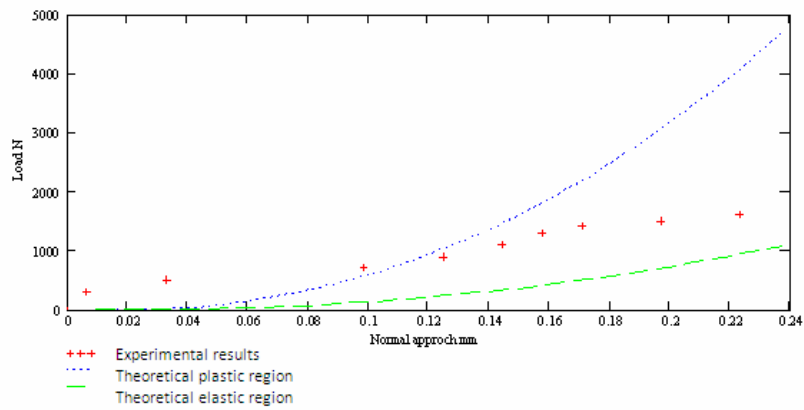


Fig.(10) Relation between applied load and normal approach for aluminum with spherical indenter (D=10mm)

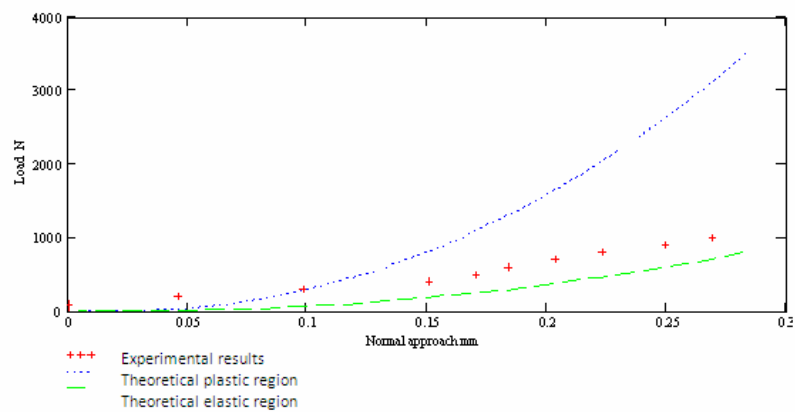


Fig.(11) Relation between applied load and normal approach for aluminum with spherical indenter (D=5mm)

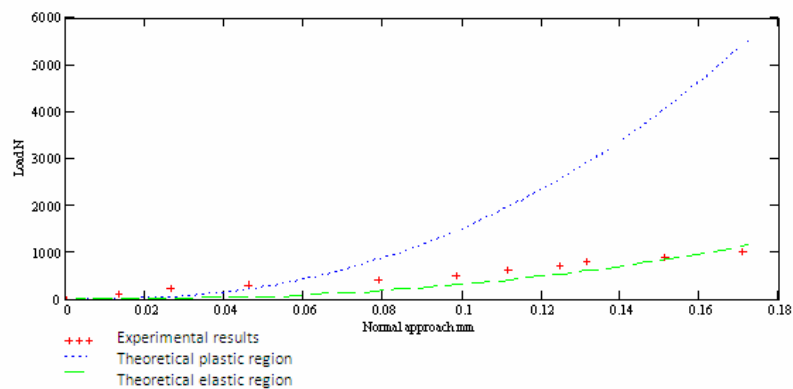


Fig.(12) Relation between applied load and normal approach for Brass2 with spherical indenter (D=10mm)

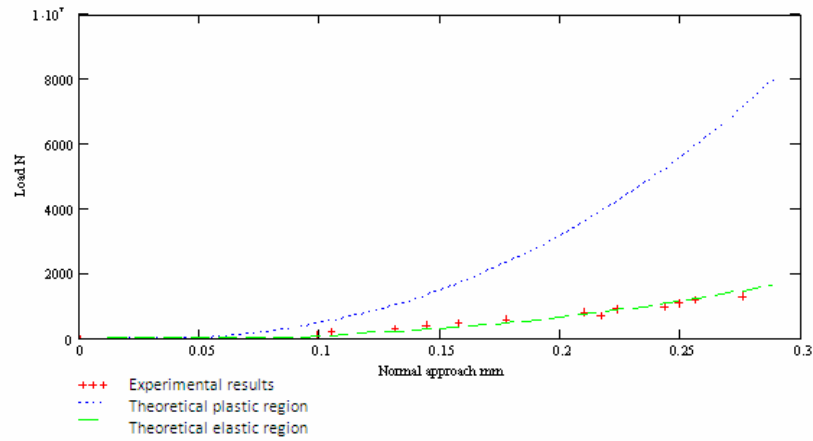


Fig.(13) Relation between applied load and normal approach for Brass2 with spherical indenter (D=5mm)

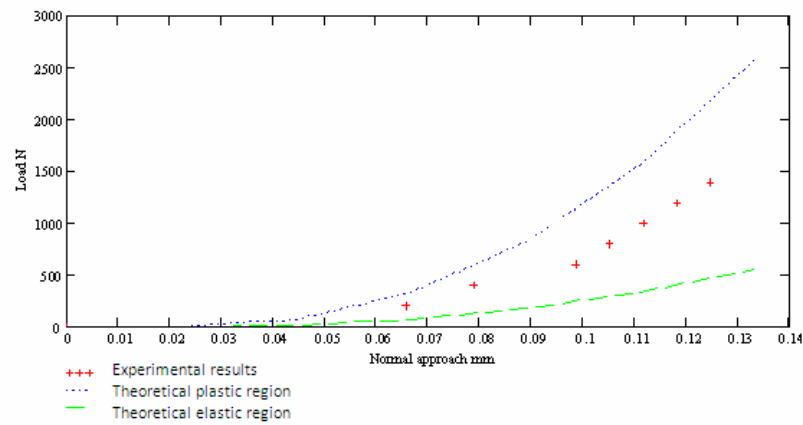


Fig.(14) Relation between applied load and normal approach for Brass1 with spherical indenter (D=10mm)

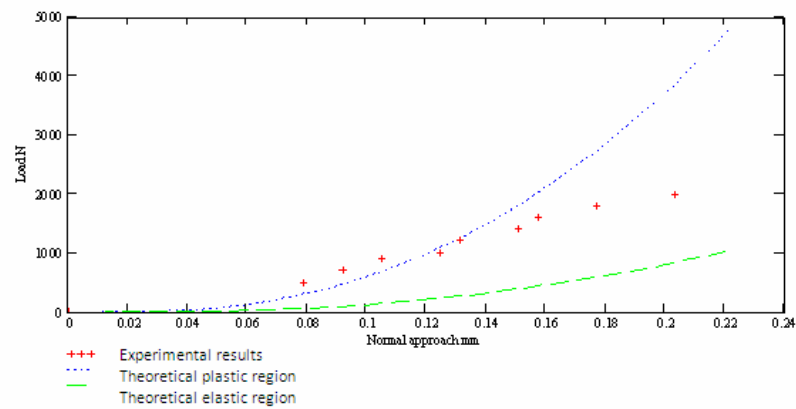


Fig.(15) Relation between applied load and normal approach for Brass1 with spherical indenter (D=5mm)

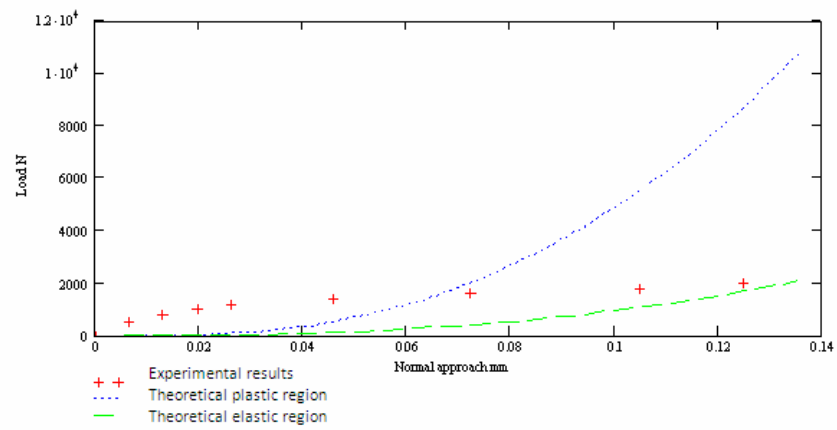


Fig.(16) Relation between applied load and normal approach for steel ck45 with spherical indenter (D=10mm)

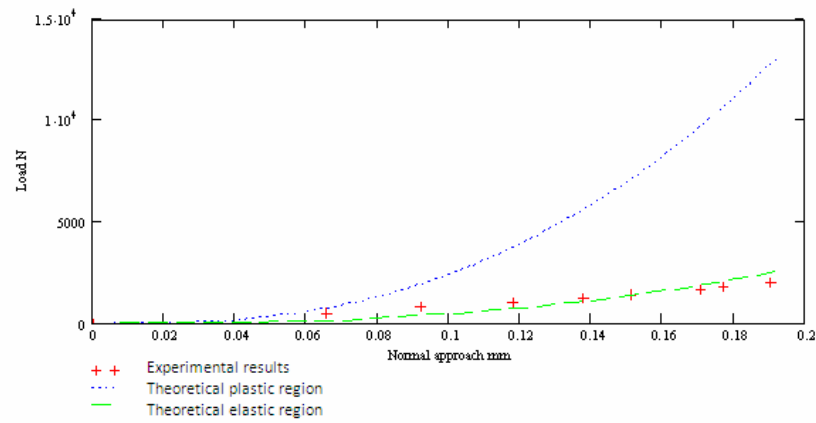


Fig.(17) Relation between applied load and normal approach for steel ck45 with spherical indenter (D=5mm)



(300 Length*100 Width*3 thickness mm)

. (W/m^2 1500 – 250)

. (90° , 60° , 45° , 30° , 0°)

, (7.16 – 1.63 mm) (a)

(16 – 2 Hz) (f)

. ($138.991 < Ra < 487.275$)

(60° 0°)

($\theta = 90^\circ$) (13%)

(7.6 %)

ABSTRACT

The aim of this work is to perform an experimental study for the effect of forced vertical vibrations on free convection heat transfer coefficient, from flat plate made of Aluminum with dimension (300 Length*100 Width*3 thickness mm). It's heated under a constant heat flux of (250-1500 W/m^2) upward. The flat plate was located horizontally or inclined in multiple angles at range of (0° , 30° , 45° , 60° , 90°). The experimental study is carried out at a range of frequency (2-16 Hz), the amplitude at the range of (1.63-7.16 mm), and the Rayleigh number at the range ($138.991 < Ra < 487.275$).

The results of this study show that, the relation between the heat transfer coefficient and the amplitude of vibration is incrementally for inclination angles from (0° - 60°), and reaches a maximum ratio of (13%) in the horizontal position, except at the vertical position ($\theta=90^\circ$) the heat transfer coefficient decreases as the vibration response increases and the maximum decrease ratio occurs at (7.6 %).

m^2		A_s
m		a
m/s^2		$acc.$
Hz		f
m/s^2	(9.81)	g
$W/m^2.C$		h
$W/m^2.C$		h_v
$W/m^2.C$		$h_{av.}$
$W/m^2.C$		$hr_{av.}$
$Amp.$		I
$W/m.C$		k
$W/m.C$		k_p
m		L
$-$		Nu
m		P
$-$		Pr
W/m^2		Q
W		$Q_{conv.}$
W		$Q_{gen.}$
W		$Q_{rad.}$
$-$		Ra
$-$		Re_v
K		T_{air}
K		T_f
K		$T_{sur.}$
m/s		u_v
$Volt$		V
m		w
$1/K$		β

:

(Ra)

.(Nu)

Rodrig,) (2003)

[3] (et al

(315 mm height * 35 mm width)

) W/m²

10000,5000,3000,2500,2000,1500,10

560) (00

mm long * 470 mm height * 130 mm

(width

. (10¹²)

:

. [1]

$$Nu = \frac{2}{360^{1/5}} \times \left[\frac{Pr}{\frac{4}{5} + Pr} \right]^{1/5} \times Ra_y^{1/5} \quad (1)$$

Fohanno &) (2005)

[4](Polidori

. [2]

$$Nu = 118.6350 * Ra_v^n \quad (8)$$

$$Nu = 118.6350 * Ra^{0.53506} * Re_v^{-0.11269} * \theta^{-1.30968} \quad (9)$$

) (2009)

[6] (

$$Nu_x = 0.496(Ra_x)^{1/5} \quad (2)$$

$$(16\text{mm}) \quad Nu_x = 0.073(Ra_x)^{2/7} \quad (3)$$

(48mm)

$$Ra_x > 6.3 \times 10^9$$

() (2007)

[5]

(45°, 0°)

(f)

2.2 – 0) (a) (16-2 Hz) (300mm)

(mm

(16mm)

.(1500-500 W/m²)

(48mm)

(1500-500)W/m²

(13.34%)

(f)

(60°-0°)

1.79-) mm (a)

(20-2 Hz)

. (0

(Re_v)

(Ra)

$$h = [(2 * 10^{-3}) - (2 * 10^{-5} * Re)] * \theta + 0.004 * Re + 3.98 \quad (10)$$



.(Teflon)

:

(U)

300mm)

(long * 100mm width * 3mm height

(30)

(1000 W) (V*I)

(1mm)

.(1)

(1.5mm)

(Varic)

.(super glue)

(K)

(30)

(0.3mm)

(0.06mm)

Selector)

(Mica)

(Switch

(0.5mm)

(Thermometer)

)

. (3.5 3

Random)

)

(Function Generator

(

(Digital Oscilloscope)

(Power Amplifier)

(Vibration Exciter)

Vibration

(18mm)

(330mm*125mm)

(Meter)

$$:(A_t)$$

$$(0.003\text{ m}^2)$$

$$A_t = W * L \tag{15} \tag{3} \tag{2}$$

:

$$T_{sav} = (T_1 + T_2 + + T_n)/N \tag{16}$$

$$(T_f)$$

$$T_f = \frac{T_{sav} + T_{air}}{2} \tag{17} \tag{Q_{gen}}$$

$$(\quad)$$

$$(Q_{conv})$$

$$\cdot (Q_{rad})$$

$$Q_{gen} = Q_{conv} + Q_{rad} \tag{11}$$

:

$$\beta = 1/(T_f + 273) \tag{18}$$

$$Q_{gen} = I * V \tag{12}$$

:

$$\cdot (11)$$

$$Q_{rad} = \sigma * \varepsilon * S_{sur} * A_t * (T_{sav}^4 - T_{air}^4) \tag{13}$$

: ε

$$\cdot (0.04)$$

$$\cdot (15)$$

$$\cdot [7] (1)$$

$$: S_{sur}$$

(Dimensionless)

Parameter

$$(T_f)$$

$$h = \frac{Q_{conv}}{A_t * \Delta T} \tag{14}$$

Vibration Reynolds)

:

(225)

(1500,1000,750,500,250 W/m²)

(90°,60°,45°,30°,0°)

Rayleigh number) (number

. (Nusselt number) (

$$Re_v = \frac{2 \cdot \pi \cdot f \cdot a \cdot \delta}{v} \quad (19)$$

$$Ra = \frac{\beta \cdot g \cdot (T_{sav} - T_{air}) \cdot \delta^3}{v^2} \cdot Pr \quad (20)$$

$$Nu = \frac{h \cdot \delta}{k_f} \quad (21)$$

(θ)

[5]

$$Ra = \frac{\beta \cdot g \sin \theta \cdot (T_{sav} - T_{air}) \cdot \delta^3}{v^2} \cdot Pr \quad (22)$$

:

(5,4)

(Amp.)

(u_v)

(250W/m²)

:(8)

$$\delta = \frac{W \cdot L}{2(W + L)} \quad (23)$$

:(90°)

(0°)

$$\delta = \frac{W \cdot L \cos \theta}{2(W + L \cos \theta)} \quad (24)$$

6)

(Hz

16)

$$\delta = L = 300 \text{ mm} \quad (25)$$

.(Hz

(Re_v)

(δ) تمثل الطول المميز للصفحة.

$$Pr = \frac{\mu \cdot Cp}{k_f} \quad (26)$$

:(h_vav.)

(Vibration Velocity)

(6)

$$u_v = a \times f \quad (27)$$

$$a = \frac{acc. \cdot \sqrt{2}}{(2\pi \cdot f)^2} \quad (28)$$

(16,10,6,2 Hz)

(6 Hz)
(30°)
(16 Hz)

:

:

$$Nu = C * Ra^m * Re_v^n * \theta^l$$

(29)

(C , m , l) (Nu)

:

(DGA-V1)

(11,10,9,8,7)

%)

(2.5-1

(16,10,6 ,2 Hz)

:

(29)

(2)

.

(60°,45°,30°,0°) (1)

°

- ")
- (1981).
- [2] M.C.Charrier Mojtabi, Y.P.Razi, K.Maliwan and A.Mojtabi, "Heat transfer due to high frequency vibration ", Int. J. Heat and mass transfer, (2003). -1
- [3] Rodrigo G.L. , Jose' A.F. And Douglas M.R. "Natural convection of Vertical flat plates" from Internet, (2003). (13%) -2
- [4] S. Fohanno, G. Polidori "Modeling of natural convective heat transfer at an internal surface "from Internet, (2005) . (7.6 %) -3
- " [5]
- "
- "
- " (2007) -4
- " [6]
- "
- " -5
- "
- " (2009)
- [7] K.L.Kumar, "Engineering Fluid Mechanics", 5th.Edition, Boston, 1990.
- :
- [8] P.K.Nag, "Heat and Mass Transfer", Second Edition, Tata McGraw-Hill Publishing Company Limited, 2007. [1]

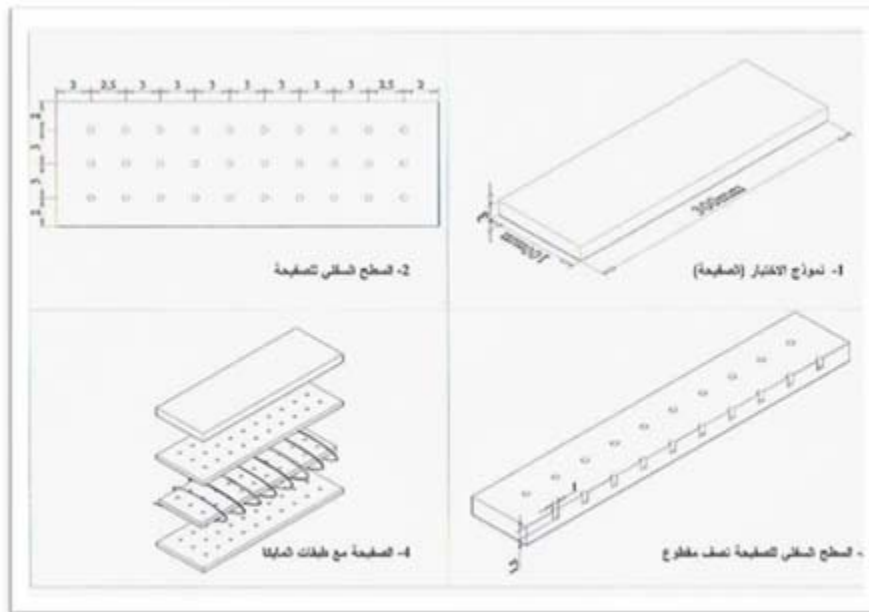
الجدول (1) يوضح النسب المئوية لقيم معامل انتقال الحرارة بوجود الاهتزاز إلى عدم وجوده.

θ	$f = 2 \text{ Hz}$	$f = 6 \text{ Hz}$	$f = 10 \text{ Hz}$	$f = 16 \text{ Hz}$
0°	12.0977	13.2894	11.3854	11.4888
30°	10.6678	4.0475	5.0203	5.386
45°	0.967	1.3721	1.0203	3.0976
60°	3.5358	2.5849	4.1174	5.3575
90°	7.1267	6.6189	7.6475	7.049

(29)

(2)

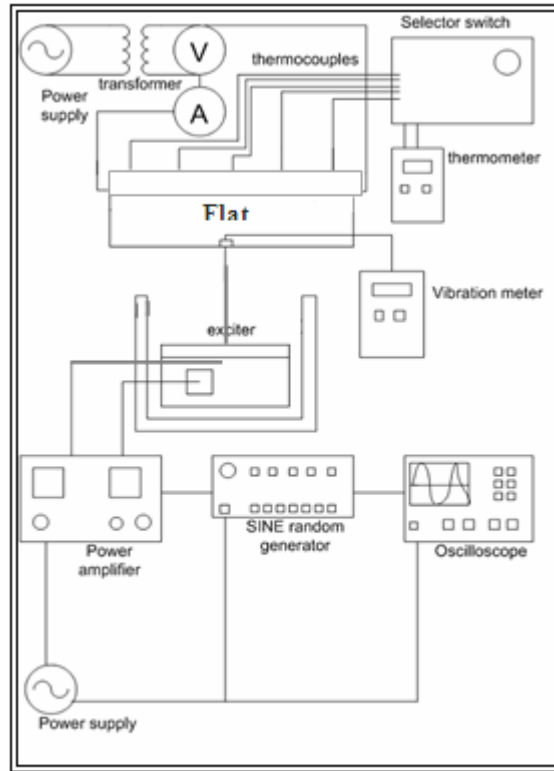
$f = 2 \text{ Hz}$				
Q (W/m^2)	C	m	n	l
250	1.433E-93	23.735	37.027	-0.8125
500	2.639	1.147	-0.693	6.92E-02
750	0.232	1.154	-0.703	-7.6325E-02
1000	11165.57	9.350E-02	-0.703	4.489E-02
1500	1.847E-12	4.53	4.42	-8.78E-02
$f = 6 \text{ Hz}$				
Q (W/m^2)	C	m	n	l
250	2.2E+71	-13.968	-27.448	0.556
500	4.75E-25	8.095	7.595	-0.1711
750	5.6E-02	1.841	-0.369	-0.0762
1000	527.155	0.746	-1.8155	5.409
1500	1.327E-13	4.457	4.5127	-7.9744
$f = 10 \text{ Hz}$				
Q (W/m^2)	C	m	n	l
250	573.7996	-0.000977	-0.2709	0.000329
500	4.799E-25	7.917	8.166	-0.146
750	0.447	1.587	-0.673	-7.235
1000	53.23	0.891	-1.2522	1.035
1500	0.0338	1.187	0.7966	0.1559
$f = 16 \text{ Hz}$				
Q (W/m^2)	C	m	n	l
250	8.65E-04	2.168	4.516	-6.485
500	3.127E-54	15.782	18.337	-0.939
750	0.4929	1.546	-0.601	-0.072
1000	0.276	1.67	-0.704	-1.667
1500	1.095E-11	4.044	3.75	-0.12155



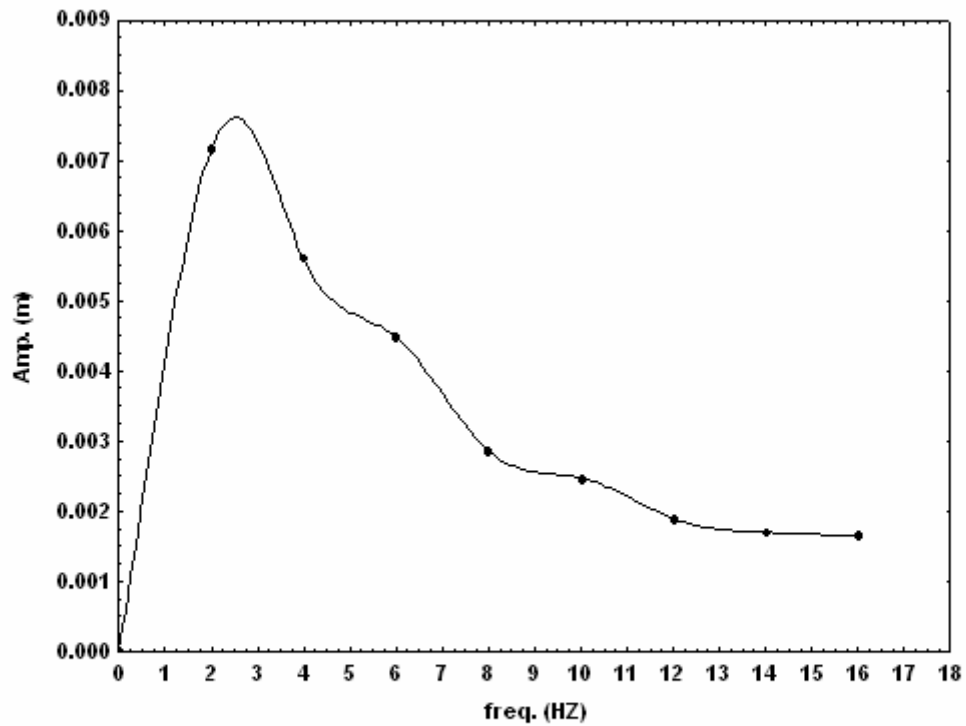
شكل (1) مخطط يوضح نموذج الاختبار المستخدم في البحث



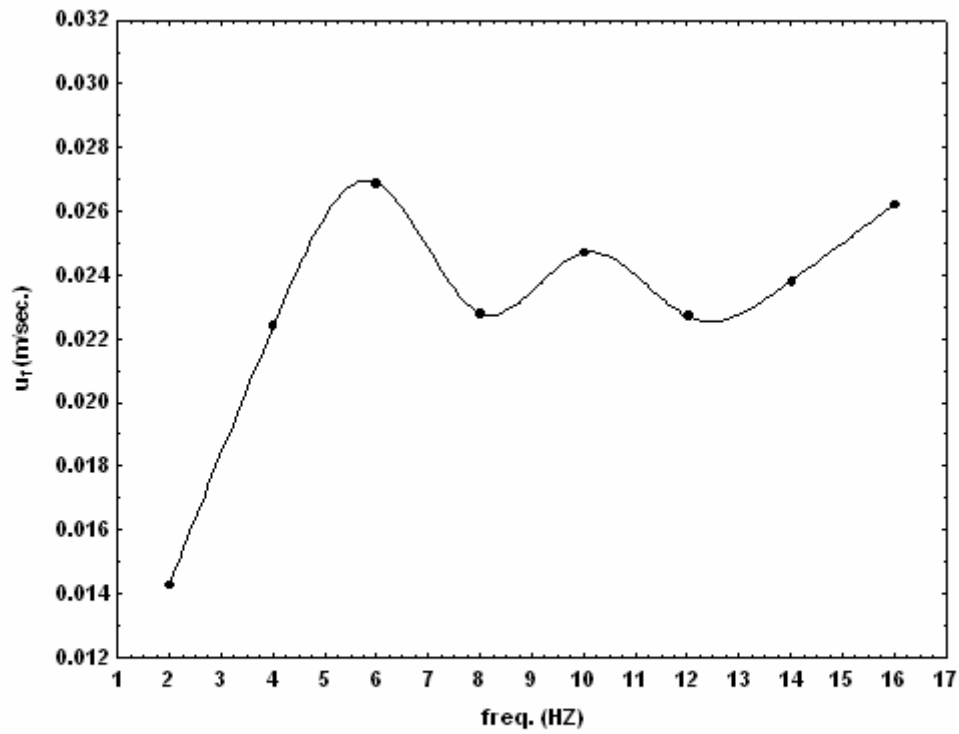
الشكل (2) صورة فوتوغرافية لمنظومة الاختبار



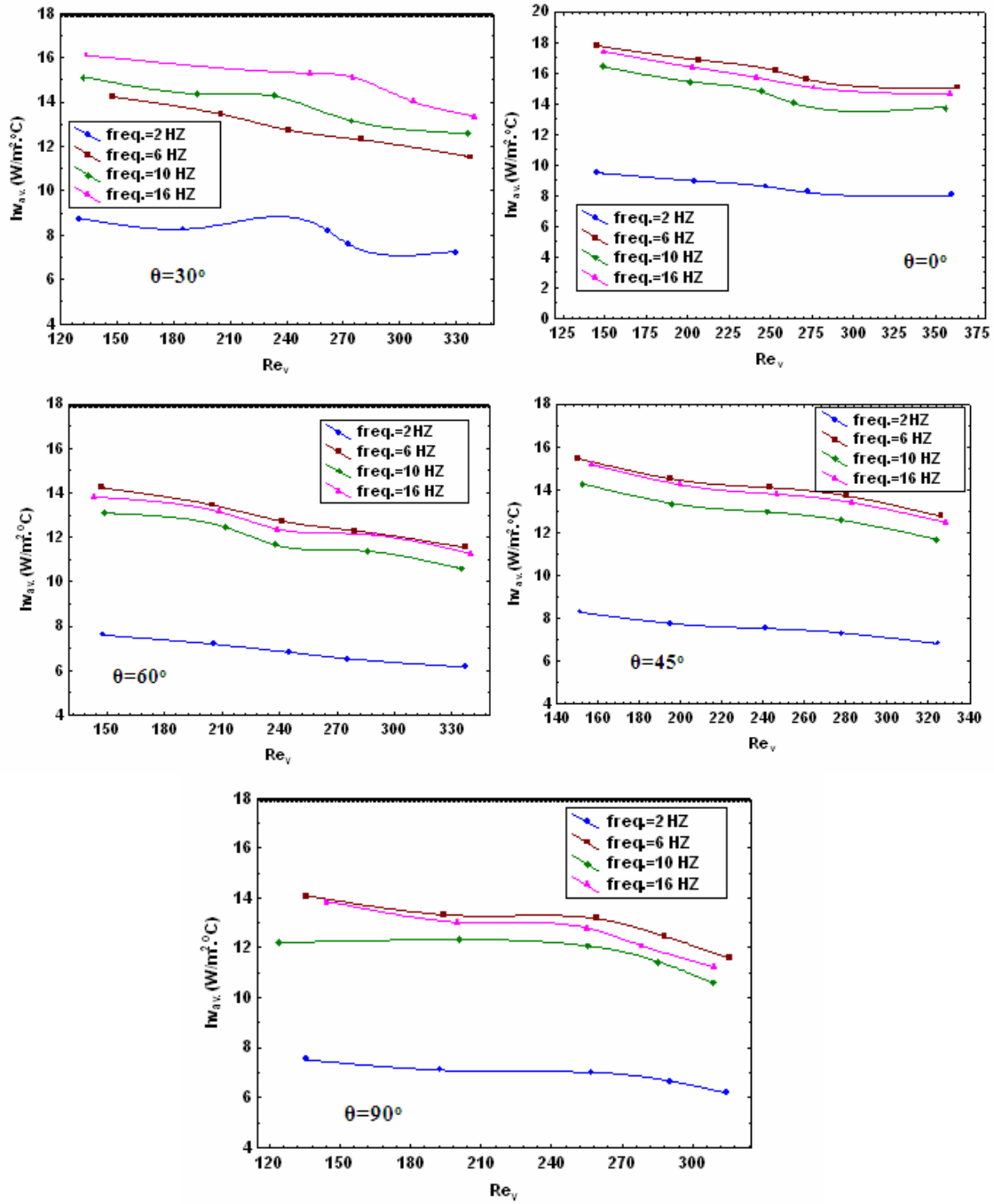
الشكل (3) يوضح منظومة الاختبار المستخدمة



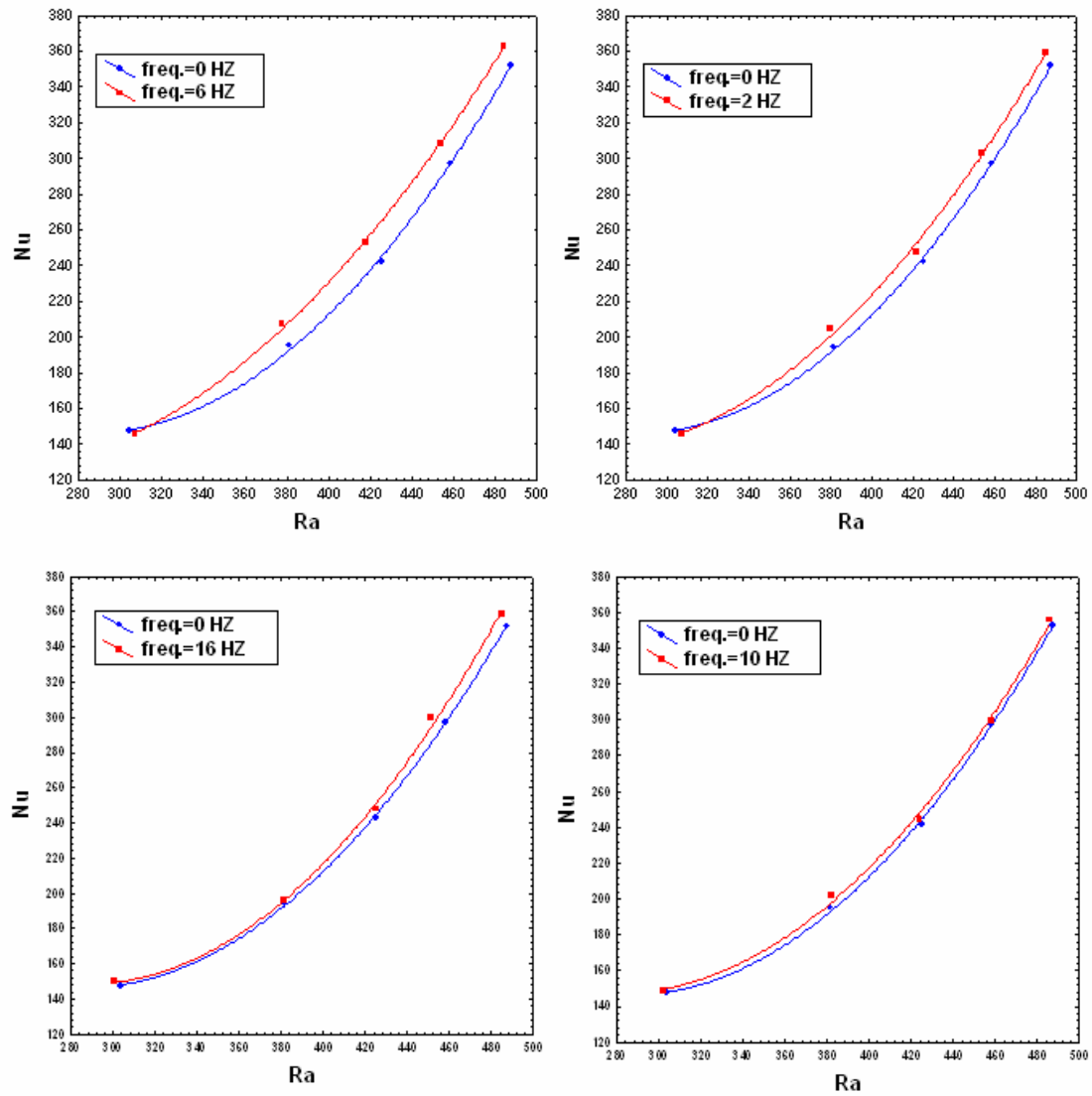
الشكل (4) يوضح تأثير تردد الاهتزاز في السعة لفيض حراري (250 W/m^2) ولزاوية ($\theta=0^\circ$)



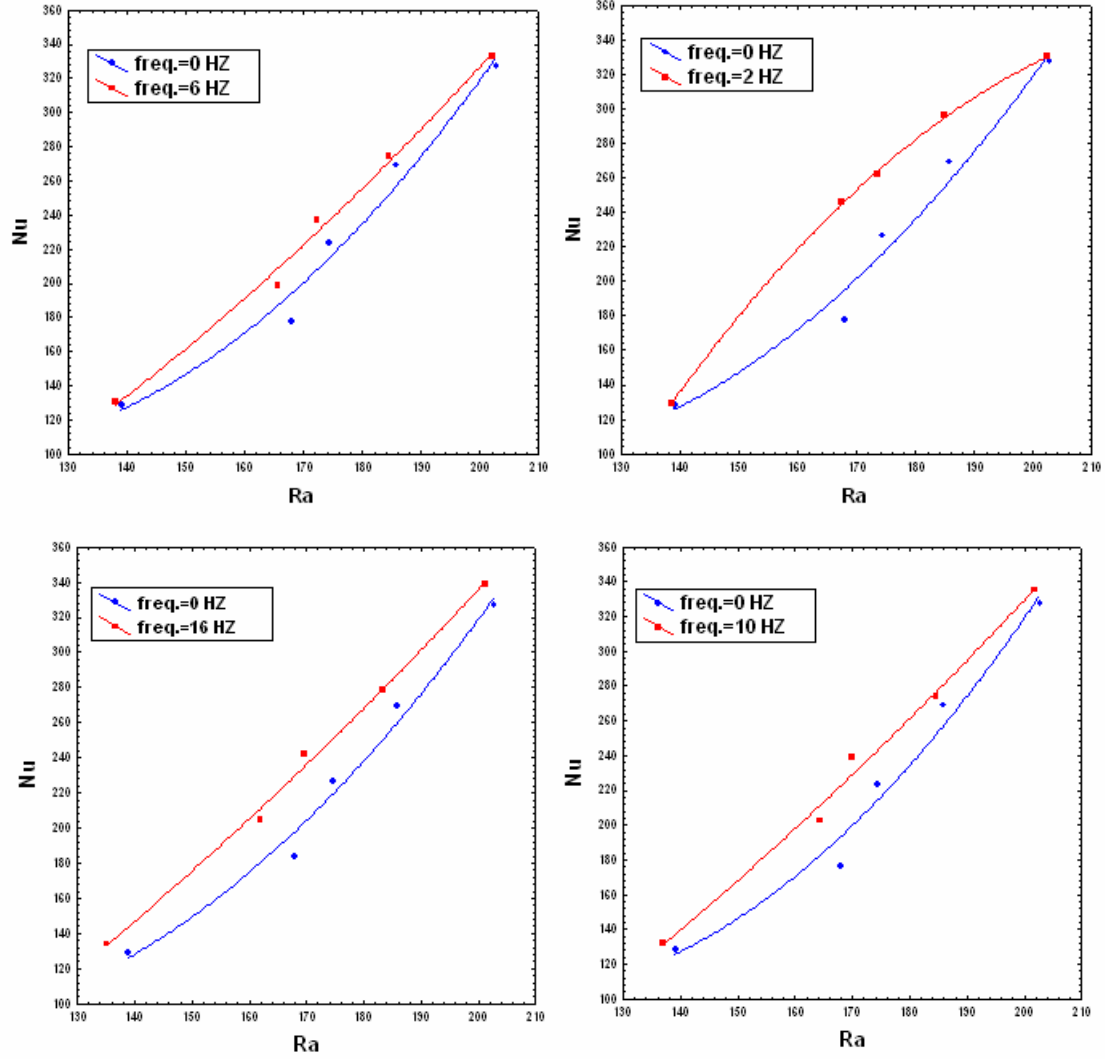
الشكل (5) يوضح تأثير تردد الاهتزاز في سرعة الاهتزاز لفيض حراري (250 W/m^2) ولزاوية ($\theta = 0^\circ$)



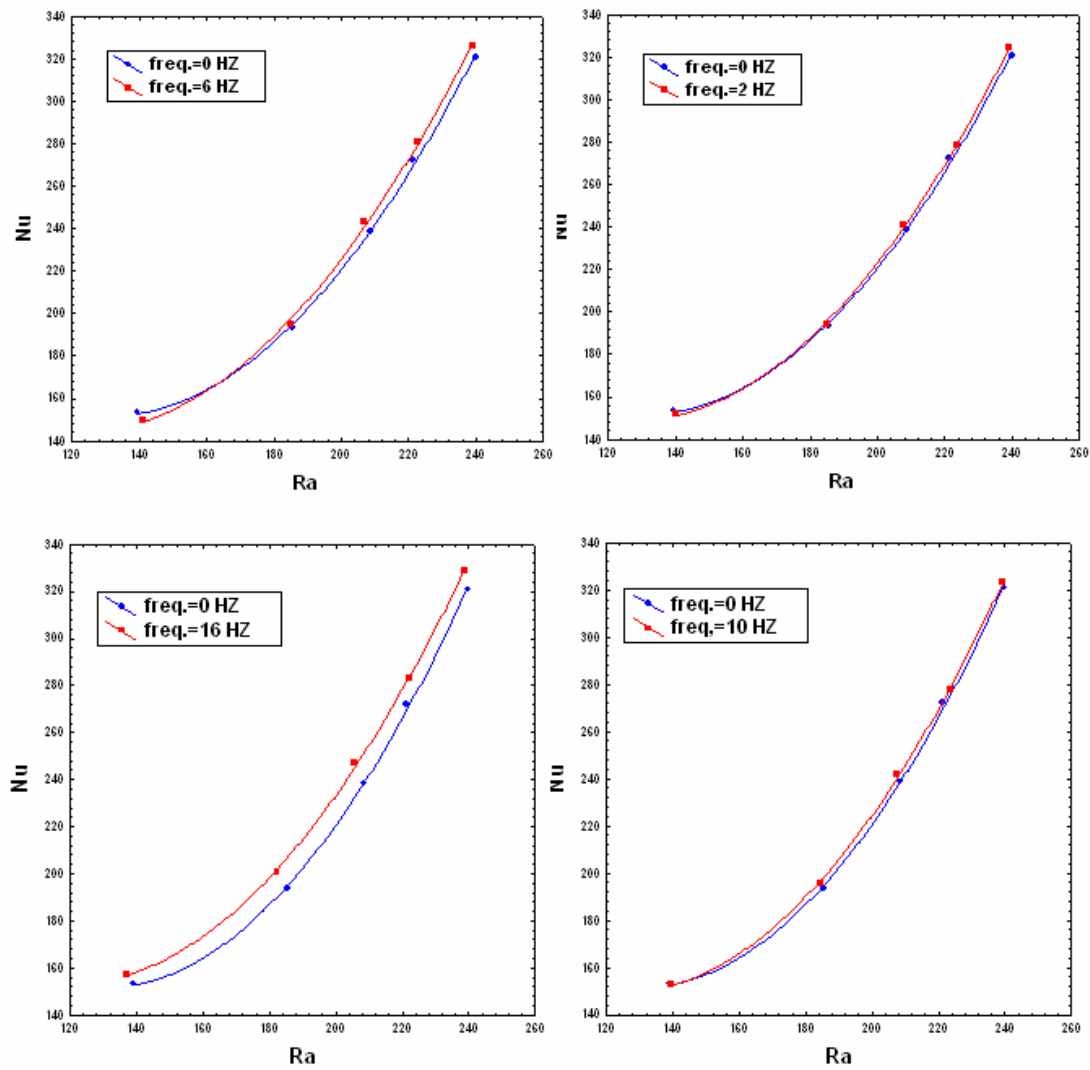
الشكل (6) يبين تأثير عدد رينولدز في معامل انتقال الحرارة الإجمالي الاهتزازي لمختلف مستويات الفيض الحراري



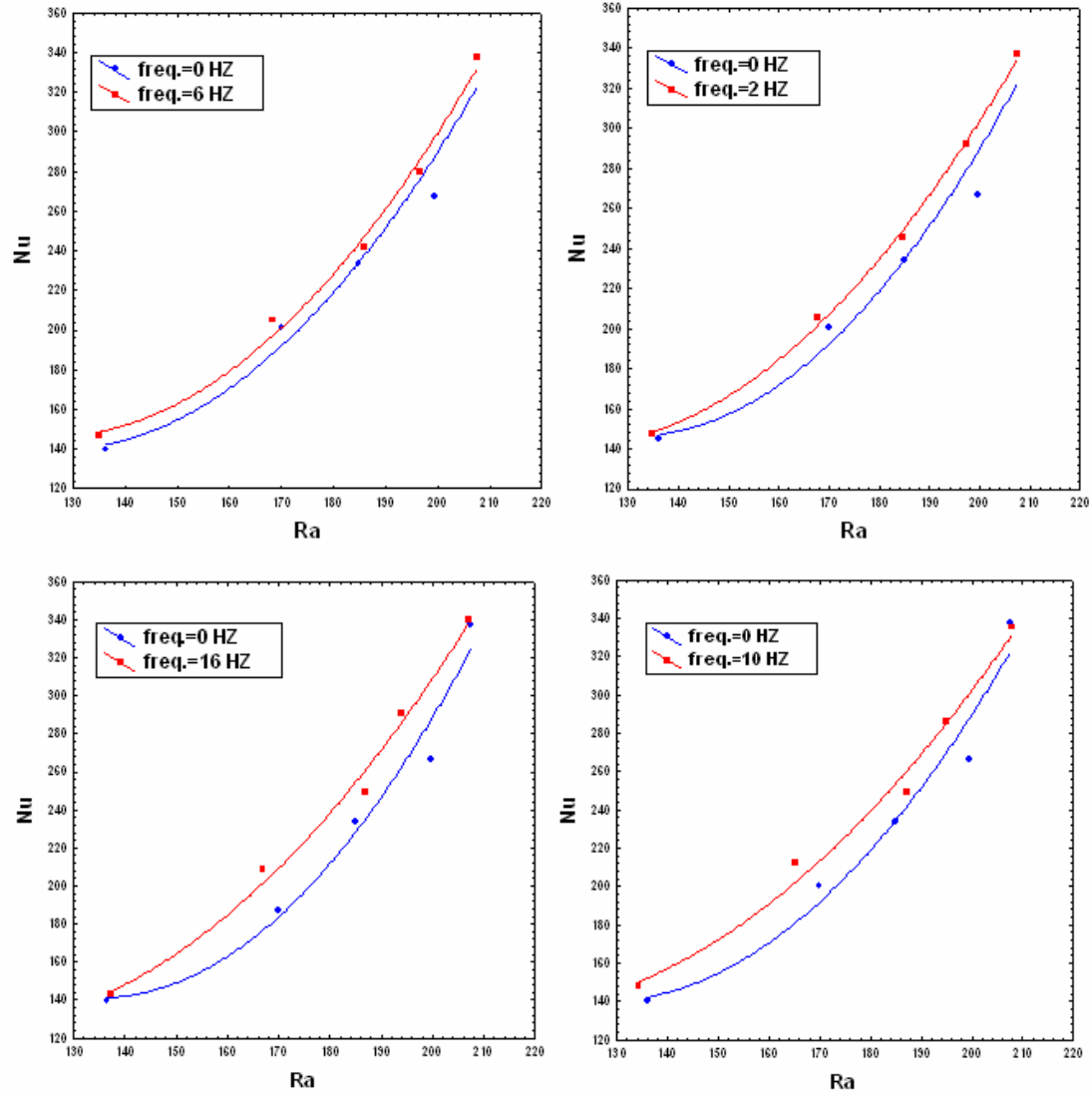
الشكل (7) يبين تأثير عدد راييلي في عدد نسلت الاجمالي بوجود وعدم وجود الاهتزاز للزاوية $\theta=0^\circ$ ولمختلف مستويات القبض الحراري



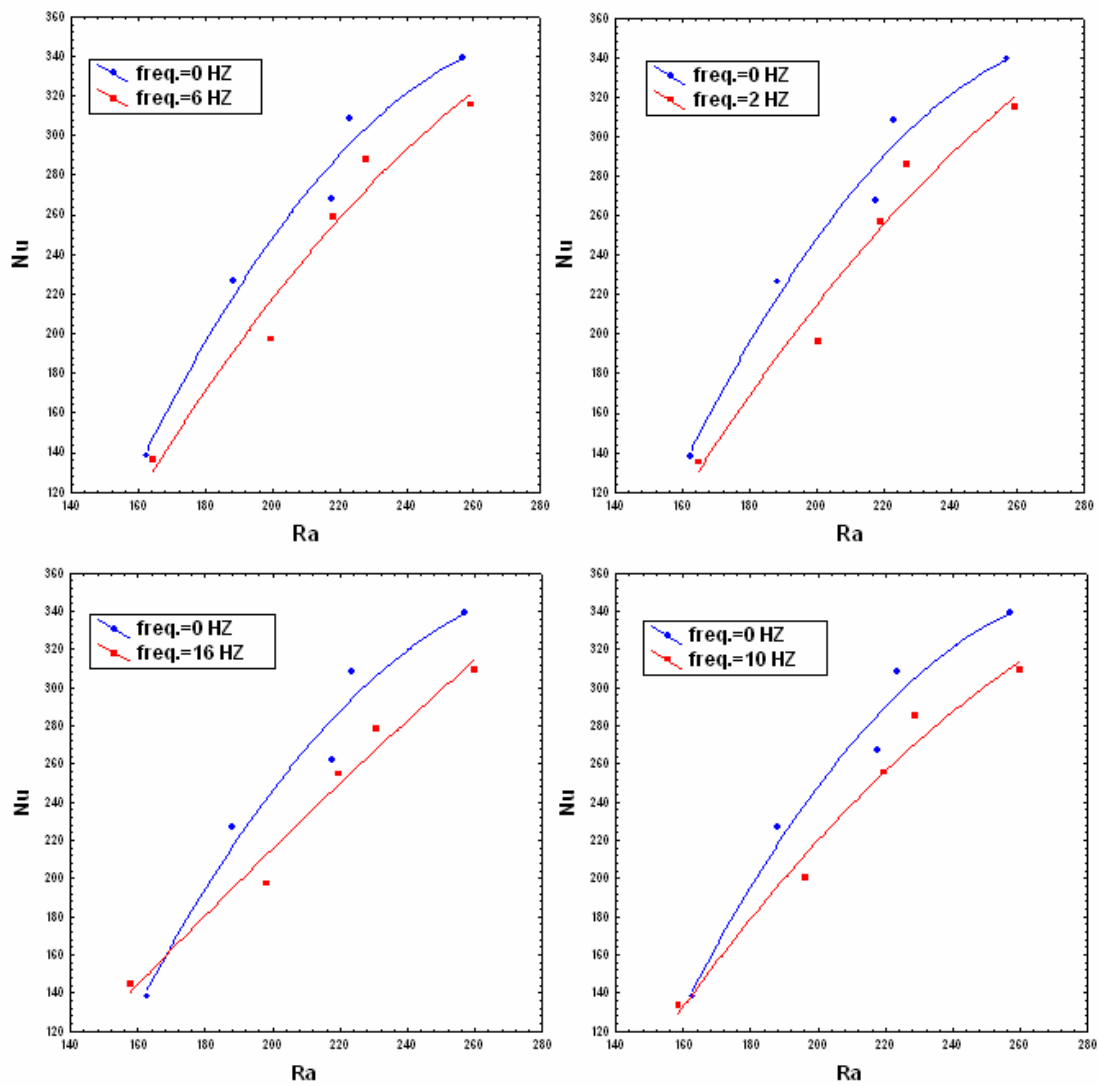
الشكل (8) يبين تأثير عدد راييلي في عدد نسلت الاجمالي بوجود وعدم وجود الاهتزاز للزاوية $\theta=30^\circ$ ولمختلف مستويات الفيض الحراري



الشكل (9) يبين تأثير عدد راييلي في عدد نسلت الإجمالي بوجود وعدم وجود الاضطراب للزاوية $\theta=45^\circ$ ولمختلف مستويات الفيض الحراري



الشكل (10) يبين تأثير عدد راييلي في عدد نسلت الإجمالي بوجود وعدم وجود
الاهتزاز للزاوية $\theta=60^\circ$ ولمختلف مستويات الفيض الحراري



الشكل (11) يبين تأثير عدد رايلى في عدد نسلت الإجمالي بوجود وعدم وجود الاهتزاز للزاوية $\theta=90^\circ$ ولمختلف مستويات الفيض الحراري

BEARING CAPACITY OF SHALLOW FOOTINGS RESTING ON DUNE SAND

Dr. Bushra S. Albusoda
Lecturer, Civil Eng. Department
University of Baghdad
E-Mail: albusoda@yahoo.com

Lubna A. Kh. Salem
B.Sc. Civil Eng. Department
University of Baghdad
E-Mail: lubnasalem_1986@yahoo.com

ABSTRACT

As a result of the growth of economic, demographic and building activities in Iraq, that necessitates carrying out geotechnical investigations for the dune sand to study behavior of footings resting on these soils. To determine these properties and to assess the suitability of these materials for resting shallow foundation on it, an extensive laboratory testing program was carried out. Chemical tests were carried out to evaluate any possible effects of the mineralogical composition of the soil on behavior of foundation rested on dune sands. Collapse tests were also conducted to trace any collapse potential. Loading tests were carried out for optimum water content and different shapes of footing. Loading test recommends manufacturing of steel box and footing models with different shapes and dimensions. The results indicated that, Affek dune sand is predominantly fine sand with non-plastic fines. Because the content of sulphate (as SO_3) is only 0.05%, and the alkalinity of dune sand, which reduces the corrosion potential, ordinary Portland cement can be used in concrete foundation construction in/on dune sands. The results of collapsing tests showed that Affek dune sand exhibit a slight to moderate potential depending on stress level. Due to Soaking by water, the reduction in bearing capacity of optimum state was about 45%. The bearing capacity of square footing was greater than those of the circular and rectangular footings.

المستخلص

نتيجة للنمو الاقتصادي والبشري وفعاليات البناء في العراق، أصبح من الضروري إجراء تقييم لرمال الكثبان من النواحي الجيوتكنيكية وكفاية تصرف هذه الرمال على تحمل الاسس الضحلة. تم وضع برنامج للفحوصات المختبرية الاساسية وشمل ايضا الفحوص الكميائية لتحديد تأثير المحتوى المعدني للرمال على تصرف الاسس الضحلة. اجريت كذلك فحوص الانهيار بطرق مختلفة. واجريت بعد ذلك فحوصات التحميل على اسس مختلفة الاشكال وبترية محدوله لحاله الرطوبه المثلى. ان رمال الكثبان في منطقته عفاك تتكون من رمال ناعمه ومواد غير لدنه انعم منها. واطهرت النتائج ايضا ان المحتوى الجبسي قليل جدا ($SO_3=0.05\%$) وعليه فان رمال الكثبان المفحوصة ملائمة لانشاء الاسس من الخرسانه باستعمال السمنت العادي بدون اي ضرر. اظهرت نتائج فحوص الانهيار ان الرمل المفحوص قد ابدى إمكانية الانهيار تتراوح من ضئيله الى متوسطة حسب مستوى الاجهاد عليه واطهرت النتائج ايضا ان تحمل الاسس قد انخفض نتيجة الغمر بالماء بحدود 45% وان تحمل الاساس المربع اعلى من تحمل الاسس الدائريه والمستطيله تحت نفس الظروف.

Keyword: bearing capacity, shallow footings, dune sand, loading test

INTRODUCTION

Dune sands usually have a single-sized grading curve. They occur frequently in loose state with low in situ densities. That is due to the poor packing of uniformly graded materials deposits in a sub-arid environment. They also have low bearing capacity and large settlement due to their low density. Das (2007) mentioned some of typical properties of dune sands as follows:

1. Grain size distribution of the sands at any particular location is uniform. The uniformity can be attributed to the sorting action of the winds
2. The general grain size percentages decrease with distant from the source, because the wind carries the small particles farther than the large ones.
3. The relative density of sand deposited on the windward side of the dunes is as high as (50-65) % and decrease to about (0-15) % on the leeward.

Ismael (1994) presented a review of the geotechnical properties, composition nature and spatial variability in three main soil deposits in Kuwait (surface windblown sands was one of them). The researcher concluded that:

1. The surface windblown dune sands are sensitive to saturation. It may collapse at some location due to ground wetting, and
2. The collapse will be evident for compacted sand at low relative density.

So, that research reflected how important is to determine the collapse potential for such soils

Al-Taie (2002) assessed the suitability of “real” sand and “pseudo” dune sand as a construction material. The results showed that the real sand dune is considered suitable for use in backfilling and embankments construction. On the other hand, for construction purposes on pseudo dune sands, a combination of placement densities in lower than the maximum values and placement moisture higher than the optimums are required. That is to insure low expansion and to reduce the loss of strength. It is worth to remind that the real sand dunes are defined as the dunes that their soil have more than 90% of sand, while pseudo-sand dunes have appreciable amount of clay and silt.

MATERIAL PROPERTIES

Dune Sand

Affek dune sand was chosen in this study. It is located between Diwaniya and Kut governorates, more precise, it is 15 km away from the town “Affek” or “Effech” as the local people use to call it. The grain size distribution curves of the soil sample are shown in Fig. 1

Affek dune sand is predominantly fine sand with non-plastic fines. According to the Unified Soil Classification System, the soil is classified as SP-SM material.

Physical properties, shear strength and compressibility parameters could be seen in Table 1, while the Chemical tests results are shown in Table 2. Chemical tests were done in the State Company for Geological Survey and Mining, and National Center for Construction Laboratories and Research (NCCLR).

Also, small difference can be noticed between the maximum and minimum unit weights, this may attributed to the poorly grading of dry soil. On the basis of permeability, the soil may be classified as low permeability soil (Terzaghi and peck, 1967).

Also, small difference can be noticed between the maximum and minimum unit weights, this may attributed to the poorly grading of dry soil. On the basis of permeability, the soil may be classified as low permeability soil (Terzaghi and peck, 1967).

The results showed that the silica is the main component in the dune sand. Because the low content of sulphate (as SO_3) and the alkalinity of dune sand, which reduces the corrosion potential, Ordinary Portland cement can be used in construction of foundations in/on the dune sand tested.

Collapse Tests

Collapse is a typical feature of unsaturated, loose and low plasticity soils, which are typical features of dune sand. Collapse is defined as the significant volume reduction observed when wetting an unsaturated sample under load. Janning and Knight discussed the problem in 1957. Then, in 1963, they proposed a test method by which they determined the collapse potential for one specimen under an applied vertical stress of 200 kPa, after one day of soaking. ASTM-D5553-00 were used to determine the magnitude of one-dimensional collapse that occurs when the soil inundated with fluid (water). The expended Knight's criterion, the Double Oedometer Method, was followed to estimate the amplitude of possible collapse as below:

$$C_p = \frac{\Delta e}{1 + e_o}$$

C_p = collapse potential (%)

e_o = initial void ratio

Δe = change in void ratio due to soaking.

The relation of collapse potential to the severity of foundation problems according to ASTM-D5333, is shown in Table 3

The results showed "slightly collapsible" trends of behavior as shown in Table 3 and Fig. 2. The results of single collapse tests

on compacted soil following Janning and Knight (1975) procedure are shown in Figure 3. This Behavior may be attributed to two reasons: **first**, the effect of compaction, which decrease the void ratio of soil and make it more dense and **second**, the effect of initial water content of compacted specimens. It is clearly shown that an increase in collapse potential (C_p) with the decrease of initial water content.

In order to determine the collapse potential of the dune sand in loose and dense states, and to show the effect of compaction on such soils, single collapse tests were carried out. The results of these tests are shown in Fig. 4. The loose state specimens exhibited higher collapse potential than the dense state. In accordance with the Janning and Knight (1975) procedure the results show that "Moderate collapsing" behavior. The collapse potential was about 6%, while the collapse potential of dense state was about 2%. This collapse behavior could be attributed to the dry, uncompacted, cohesionless, natural state of the dune sand.

The results of double Oedometer tests are shown in Fig. 6, which indicate that the level of stress plays a major role compared to that of compaction, Fig. 5. The Figure also shows that the collapse potential increase with increase of level of stress for both dry and wet side conditions. While on the optimum, the collapse potential did not show the same trend. The effect of compaction is an accepted reason for that behavior.

LOADING TESTS

A shallow footing model tests were carried out in a test box having dimensions of (360 × 360) mm in plane and 250 mm in depth. The size of the box was decided suitable for the size of footing and the range of load influence. (Depending on Bossineq's approach; three footing models were used to fulfill the objectives of this work: square(S) 60*60 mm, circular (C) 60 mm in diameter, and rectangular(R) 30*60mm).

It is known that the method of sample preparation can have a major influence on the measured response of soil. To place the soil in the box reliable as much as possible, static compaction method was used by compression machine of (10,000 kg). The preparation of the soil was done in two stages:

- (1) Soil was compacted in dense, dry unit weight as in (ASTM D2049-64T), then
- (2) Layer with 1.5B thickness at three unit weights and the corresponding water contents, (Fig. 7).

Samples were tested and compacted as quickly as possible, to avoid losing the water. The inside of the box was lined by plastic sheets to lessen the friction between the soil and the box sides.

Through the preparation of soil and loading test performance, the following points were considered:

1. When soaking conditions were conducted, the box was left to soak for 24 hours to ensure that all the soil was completely soaked.
2. After the test completed, the sand was spread for air drying over night (It looked enough in hot Summer days where the temperature was more than 42C°) and the soil lumps were crashed by rubber hammer.

Model loading tests were carried out on dune sand as given in the test program. To evaluate the bearing capacity in this work, the failure point considered at settlement equal to 10% of the width of footing (B) as ASTM (D1194-94) recommended. Also, the effects of the following factors were taken in consideration:

1. Effect of Soaking

It is important to carry out a model test in soaking condition to trace any susceptible collapse potential in soil. Model tests were carried out with optimum initial water content and different shapes of footing. Fig. 8

The results showed that the reduction in bearing capacity ratio of the dry side and optimum states were about 45%. It is further recommend that for non-cohesive soils, the values shall be reduced by 50% if the water table expected to be above or near the base of footing.

2. Effect of Shape of Foundation

From the Terzaghi equations, it's clear that for granular soil, the bearing capacity of square footing is greater than that of circular footing by 33%. These results coincide with the results of this research work (Fig 9) .The bearing capacity of square footing is greater than that of circular footing in the present work by about 12%-27%.

In addition, the rectangular footing showed a smaller bearing capacity than both of the circular and square footings. This behavior may be attributed to the scale effect that depends directly on B (width of footing). Since B= 60 mm for circular and square footings, while B= 30 mm for rectangular footing. Accordingly, the bearing capacity for rectangular footing was smaller, Fig. 10.

Comparison between the Ultimate Bearing Capacity from the Model Loading Test and Its Values From Well-known Theories

In comparison with the well known theories of ultimate bearing capacity determinations, the ultimate bearing capacity from the loading tests are shown in Table 4

The results showed a lack of agreement between theoretical and experimental findings. By re-examining Table (4-8), same trend can be seen between the different shapes and different initial water content. The large differences between theoretical and experimental finding, which may be attributed to:

1. It was found that theoretical solution based on plane strain angle of internal friction which is

higher than that based on direct shear. A variation in friction angle of only 2° may result in a variation in the value of $N \gamma$ 50% (White, 2008). Consequently, the bearing capacity will be increased.

2. The above mentioned theories are more conservatives. Meyerhof (1963) and De Beer (1970) propose a conservative estimate for shape factor acceptable for design only for low internal friction angle and a small aspect ratios (Zhu and Michalowski, 2005).
3. The physical model for shallow footing have many short comings included: 1 the self weight variations between actual self weights of the model elements, 2 temperature also different to assess in different levels in the models, 3 moisture movements cannot model with time.

CONCLUSIONS

1. Affek dune sand is predominantly fine sand with non-plastic fines. Water effectively influenced the cementation agents between the particles.
2. The results showed that silica is the main component in Affek dune sand. Because the low content of sulphate (as SO_3) and the alkalinity of dune sand, which reduces the corrosion potential. Ordinary Portland cement can be used in construction of foundations in/on dune sand.
3. Compacted dune sand showed a slight collapse potential when tested by single collapse test, while it showed moderate collapse potential under high stress level.
4. The reduction in bearing capacity ratio due to soaking of the dry side and optimum states were about 45%.
5. The results showed a lack of agreement with theoretical and experimental findings, as these theories are more conservatives.

REFREANCES

1. Aiban, S. A. (1995): "Centrifugal Verification of Bearing Capacity and Shape Factors of Shallow Foundations on Sands", *The fourth Saudi Engineering Conference*, November, Volume 2, pp 361-367.
2. Al-Taie, A. J. (2002): "Properties and Behavior of Dune Sands as a Construction Material", M.Sc. thesis, Civil Engineering Department, University of Baghdad, Iraq.
3. ASTM D1194-94: "Standard Test Method for Bearing Capacity of Soil for Static Load and Spread Footings", (Withdrawn 2003).
4. ASTM D2049-69: "Test Method for Relative Density of Cohesionless Soils". (Withdrawn 1993).
5. ASTM D2434-64T: "Standard Test Method for Permeability of Granular Soils, (Variable Head).
6. ASTM D3080-64T: "**Standard Test Method for Direct Shear Test of Soils Unconsolidated Undrained Conditions**".
7. ASTM D4253-00: "**Standard Test Method for Maximum Index Density and Unit Weight of Soils Using a Vibratory Table**".

8. ASTM D4254-00: **"Standard Test Method for Minimum Index Density and Unit Weight of Soils and Calculation of Relative Density"**.
9. ASTM D5333-00: **"Standard Test Method for Measurement of Collapse Potential of Soils"**.
10. ASTM D698-00a: **"Standard Test Methods for Laboratory Compaction Characteristics of Using Standard Effort (600 kN-m/m³)"**.
11. ASTM D854-00: **"Standard Test Method for Specific Gravity of Soil Solids by Pycnometer"**.
12. Das, B. M. (2007): **"Principle of Foundation Engineering"**, Sixth Edition, Adapted International Student Edition, Nelson a Division of Thomson Canada Limited.
13. Jannings, J. E. and Knight, K. (1975) : **"A Guide to Construction on or with Materials Exhibiting Additional Settlement Due to 'Collapse' of Grain Structure"**, *Proceedings, Sixth Regional Conference for Africa on Soil Mechanics and foundation Engineering Johannesburg*, South Affrica, pp 99-105.
14. Ismael, N. F. (1994): **"Properties and Behavior of Arid Climate Soil Deposits in Kuwait"**, Civil Engineering Department, University of Kuwait.
15. Terzaghi, K. (1943): **"Theoretical Soil Mechanic"**, John Wiley and Sons, New York.

16. Terzaghi, K. and Peck, R. (1967): **"Soil Mechanics in Engineering Practice"**. Second Edition, John Wiley and Son, NY.
17. White, D. J. (2008): **"Contributions to G'eotechnique 1948-2008: Physical Modeling"**, *G'eotechnique* 58, No. 5, pp. 413-421.

SYMBOLS	DEFINITION
B	Width of Footing
c	Cohesion
C	Circular Footing
C _c	Compression Index
C _p	Collapse Potential
C _r	Rebound Index
e	Initial Void Ratio of Soil
G _s	Specific Gravity
k	Coefficient of Permeability
L.L	Liquid Limit
N _γ	Bearing Capacity Factors
NP	Not Plastic
R	Rectangular Footing
S	Square Footing
ø	Angle of Internal Friction
γ	Unite Weight of the Soil

**Table 1** Physical properties, shear strength and compressibility parameters

Property	Value	Type of test	Standard
L.L	23%	Atterberg limits	BS 1377:1975 test No.2
PI	NP		
Gs	2.67	Specific Gravity of Solids	ASTM D-854
γ_{\max}	15.9 kN/m ³	Maximum Unit Weights	ASTM D4253
γ_{\min}	13.0 kN/m ³	Minimum Unit Weights	ASTM D4254
γ_{dmax}	18.5 kN/m ³	Standard Compaction	ASTM 698-70
k	1.6×10^{-4} cm/s	Coefficient of Permeability	ASTM D2434-64T
e_o	0.508	One-dimension Compression	ASTM D2435
C_c	0.120		
c	0	Direct Shear Tests	ASTM D3080-72
ϕ	42.7°		

Table 2 Results of Chemical Tests

Chemical Composition	Percentage (%)
SiO ₂	41.25
CaO	16.39
MgO	6.70
SO ₃	0.05
Cl ⁻¹	0.11
CaCO ₃	30.60
Gypsum Content	0.09
Organic Material	0.20
T.S.S	0.21
L.O.I	15.34
pH	8.7

Table 3 Relation of Collapse Potential to the Severity of Foundation Problems

Degree of Collapse	Collapse Potential %
None	0
Slight	0.1 to 2.0
Moderate	2.1 to 6.0
Moderately severe	6.1 to 10.0
Severe	>10

Table 4 Ultimate Bearing Capacity (kPa) from the Model Loading Test and Well-Known Theories

The Shape	Terzaghi	Meyerhof	Model Loading Tests
Square	107	154	400
Circular	80	154	350
Rectangular	-	64	335

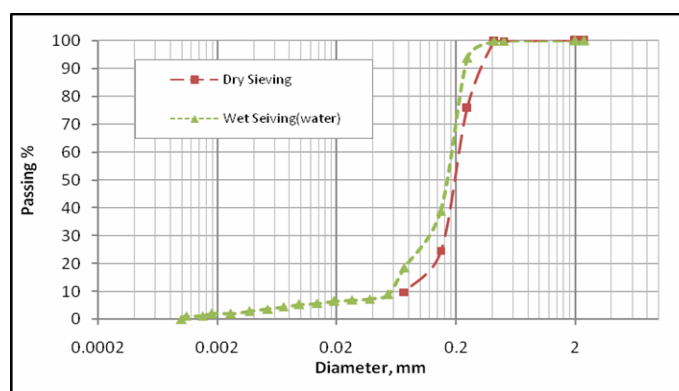


Fig. 1 Grain Size Distribution Curves

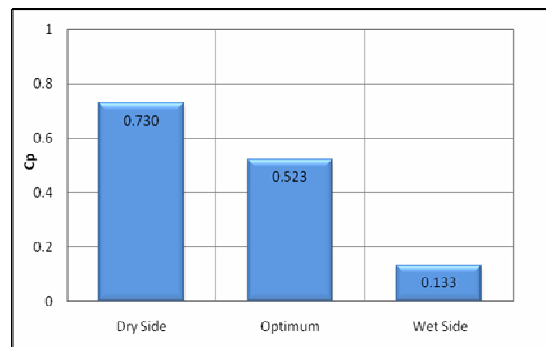


Fig 2 Results of Single Collapse Tests:
Variation of Collapse Potential with Initial water contents

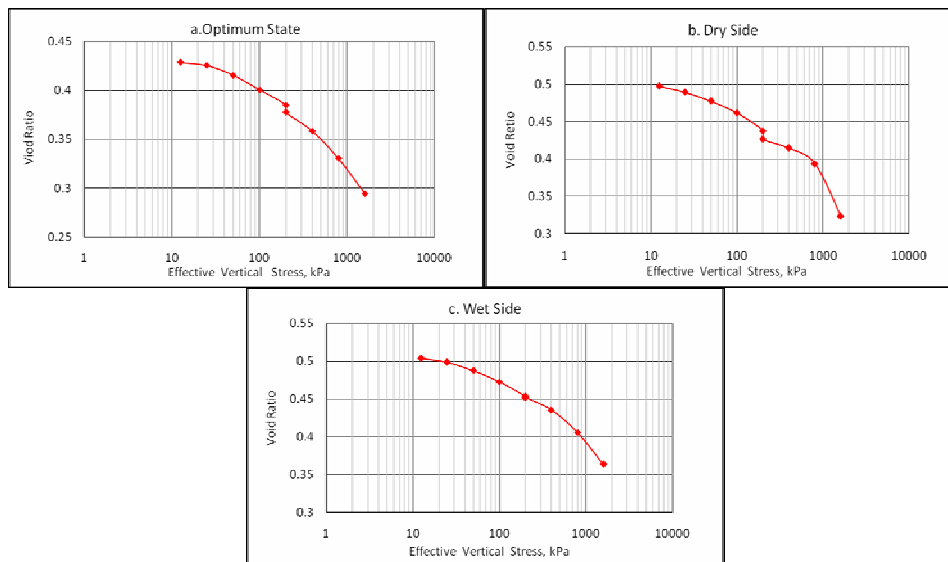


Fig. 3 Results of Single Collapse Tests at Different Initial Water Contents

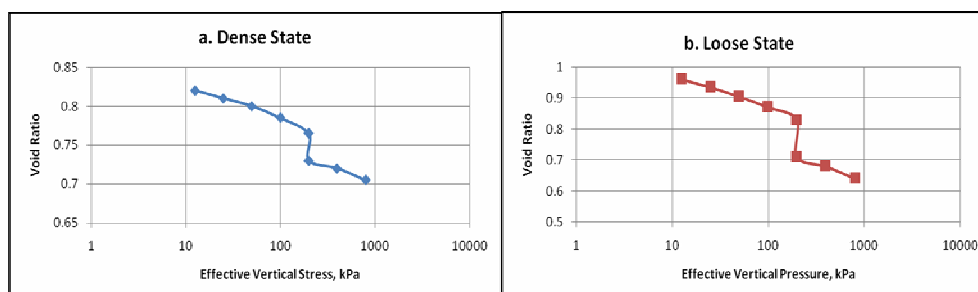


Fig. 4 Single Collapse Test Results of Dune Sand (**a.** Dense, **b.** Loose)

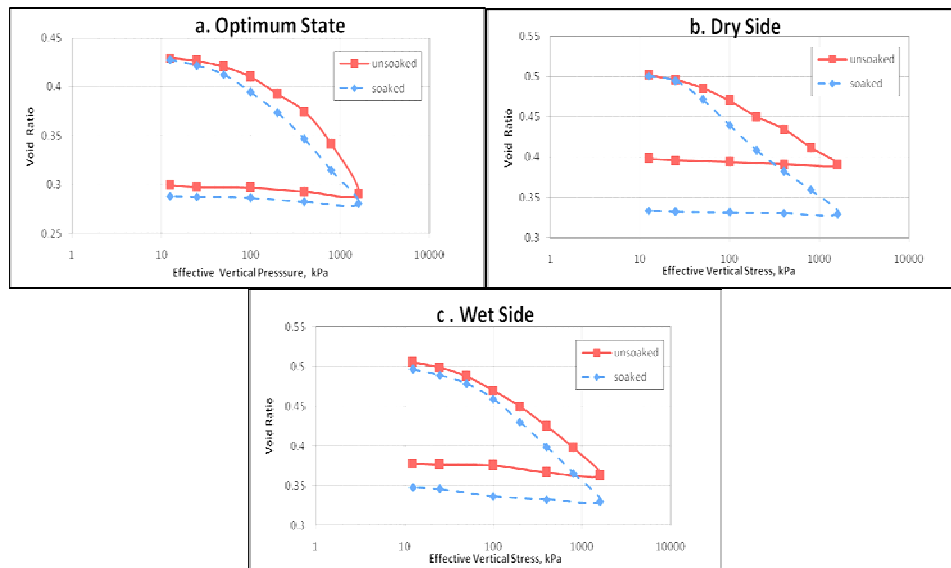


Fig. 5 Results of Double Oedometer Test at Different Initial Water Contents

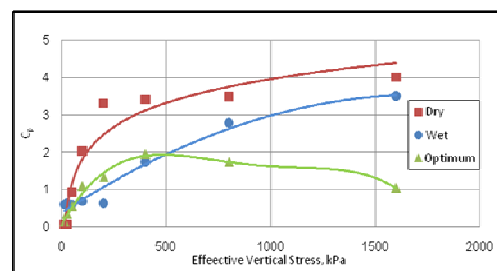


Figure 6 Results of Double Oedometer Tests: Variation of Collapse Potential with Effective Stress Level at Different Initial Water Content

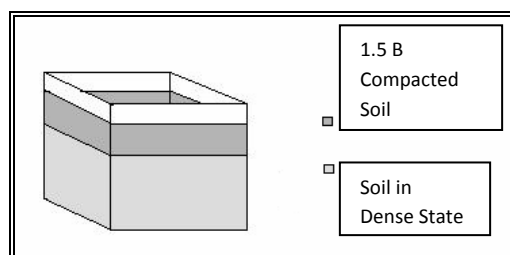


Fig. 7 Box Preparation

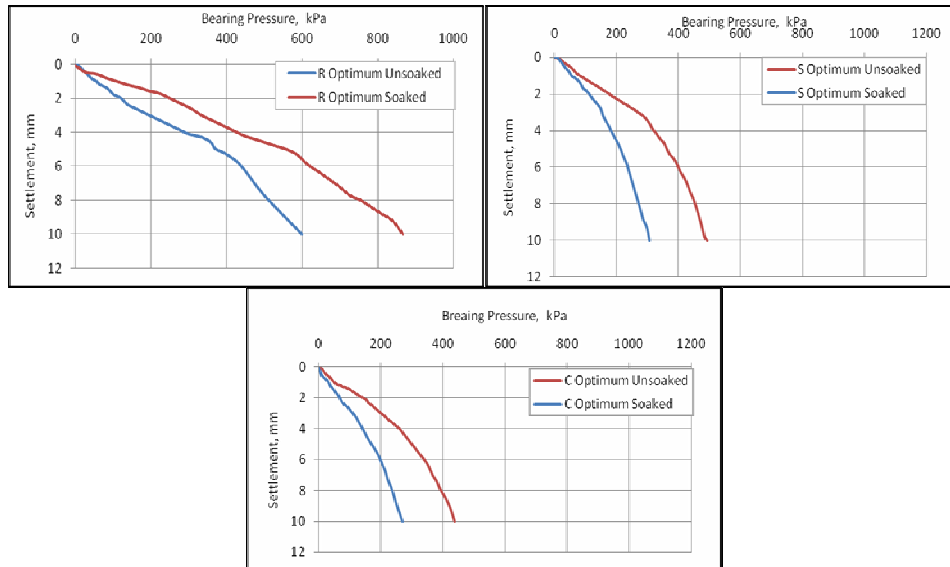


Fig. 8 The results of the Model Test on Soaked Soil in Relative with Unsoaked Soil (Optimum State)

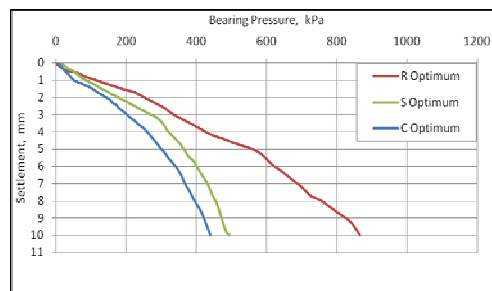


Fig. 9 Bearing Pressure-Settlement Curves for Different Shapes of Footing on Soil with Different Initial Water Contents

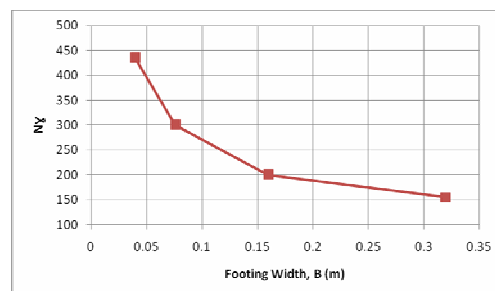


Fig. 10 Influence of Footing Size on Bearing Capacity Factors N_γ (From Cerato and Lutenege, 2007)



DESIGN OF A VARIABLE GAIN NONLINEAR FUZZY CONTROLLER AND PERFORMANCE ENHANCEMENT DUE TO GAIN VARIATION

Omar W. Abdul-Wahab
University of Baghdad
College of Engineering
Computer Engineering Department

ABSTRACT

In this paper, variable gain nonlinear PD and PI fuzzy logic controllers are designed and the effect of the variable gain characteristic of these controllers is analyzed to show its contribution in enhancing the performance of the closed loop system over a conventional linear PID controller. Simulation results and time domain performance characteristics show how these fuzzy controllers outperform the conventional PID controller when used to control a nonlinear plant and a plant that has time delay.

الخلاصة

في هذا البحث تم تصميم مسيطرين ضبابيين لا خطيين ذوا ربح متغير الاول (تناسبي - تكاملي) والثاني (تناسبي - تفاضلي) وتم تحليل تأثير خاصية الربح المتغير واسهامه في تحسين عمل النظام الكلي مقارنة بمسيطر تقليدي (تناسبي - تكاملي - تفاضلي). النتائج التمثيلية وخصائص العمل في مجال الزمن اوضحت كيف يتفوق هذان المسيطران الضبابيان على المسيطر التقليدي عند استخدامهم للسيطرة على نظامين الاول نظام لا خطي والثاني نظام يمتلك زمن تأخير.

KEYWORDS

Variable gain nonlinear fuzzy controller, plant with time delay, nonlinear plant.

INTRODUCTION

Revealing explicit structure of fuzzy controllers is important primarily because it provides insightful information about what a fuzzy controller is, how it works, and how it relates to and differs from a classical controller. A fuzzy controller is not fuzzy anymore (i.e., not a black-box controller anymore) once its explicit structure is disclosed and it just becomes a conventional nonlinear controller (Ying 2000 -1) (Ying 2000 -2).

A fuzzy controller is called a linear (or nonlinear) fuzzy controller if its output is a linear (or nonlinear) function of its inputs. In most cases, whether or not a fuzzy controller is linear cannot be judged directly from its configuration. The explicit structure of the fuzzy controller must be derived to accurately determine its type (Ying 2000 -2).

There are three sources of nonlinearity in a fuzzy controller. First, the rule base. The position, shape, and number of membership functions on the premise side, as well as nonlinear input scaling, cause nonlinear characteristics. Even the rules themselves can express a nonlinear control strategy. Second, the inference engine. If the connectives are implemented as min and max respectively, they are nonlinear. The same applies to min-activation and max-accumulation. Third, the defuzzification method. Several defuzzification methods are nonlinear (Driankov, Hellendoorn, and Reinfrank, 1996).

Utilizing the nonlinear characteristics of a fuzzy controller is an important issue. The Type ACS201 P1.0 Intelligent Fuzzy Logic Control (IFLC) software product is part of the Advanced Control Solutions (ACS) from Fisher-Rosemount Systems, Inc. The IFLC product uses fuzzy logic algorithms to improve control loop performance. With autotuning functionality, the IFLC provides superior performance for a variety of applications. The nonlinearity built into the IFLC reduces overshoot and settling time, achieving tighter control of the process loop. Specifically, the fuzzy logic controller treats small control errors differently from large control errors and penalizes large overshoots more severely. It also severely penalizes large changes in the error, helping to reduce oscillation (www.emersonprocess.com).

Ultimately, the goal of tuning is to shape the nonlinearity that is implemented by the fuzzy controller. This nonlinearity, sometimes called the

“control surface,” is affected by all the main fuzzy controller parameters (Passino and Yurkovich 1998).

The fuzzy PD and PI controllers to be introduced in this paper are natural extensions of their conventional versions, which preserve the linear structures of the PID controllers, with simple and conventional analytical formulas as the final results of the design. Thus, they can directly replace the conventional PID controllers in any operating control systems (plants, processes). The main difference is that these fuzzy controllers are designed by employing fuzzy logic control principles and techniques to obtain new controllers that possess analytical formulas very similar to the conventional digital PID controllers. After the design is completed, all the fuzzy logic IF-THEN rules, membership functions, defuzzification formulas, etc. will not be needed any more in applications: what one can see is a conventional controller with a few simple formulas similar to the familiar PID controllers. Thus, in operations the controllers do not use any “look-up” table at any step, and so can be operated in real time. A control engineer who doesn’t have any knowledge about fuzzy logic and/or fuzzy control systems can use them just like the conventional ones, particularly for higher-order, time-delayed, and nonlinear systems, and for those systems that have only vague mathematical models or contain significant uncertainties. The key reason, which is the price to pay, for such success is that these fuzzy controllers are slightly more complicated than the conventional ones, in the sense that they have variable control gains in their linear structures. These variable gains are nonlinear functions of the errors and changing rates of the error signals. The main contribution of these variable gains in improving the control performance is that they are self-tuned gains and can adapt to the rapid changes of the errors and the (changing) rates of the error signals caused by the time-delayed effects, nonlinearities, and uncertainties of the underlying system (plant, process) (Chen and Pham 2001).

Several researches had been made that utilizes the variable gain aspect of fuzzy controllers such as (Ying 2000 -1), which has proved that the analytical structure of a (two-input two-output) fuzzy PI/PD controllers is the sum of two nonlinear PI/PD controllers whose gains continuously change with system outputs. In (Brdys and Littler 2002), a



variable gain PI fuzzy controller was proposed to control a nonlinear servo system where traditional methods for controlling this system using linear control techniques are inadequate because of hard nonlinearities in the dynamics. The variable gain characteristics would compensate these nonlinearities. (Bonfe and Mainardi 2004) presents a variable gain fuzzy PID controller to control a robot arm and the experiments show the ability of this controller to greatly reduce the overshoot. (Miloudi, Draou, and AlRadadi 2002) presents an original variable gain PI controller for speed control of an induction machine drive. (Dash, Morris, and Mishra 2004) presents the design of a nonlinear variable-gain fuzzy controller for a flexible ac transmission systems device to enhance the transient stability performance of power systems.

NONLINEAR VARIABLE GAIN CONTROLLER

A variable gain PI controller (VGPI) is a generalization of a classical PI controller where the proportional and integrator gains vary along a tuning curve (Miloudi, Draou, and AlRadadi 2002). A variable gain PD controller has the same relation with the classical PD controller. In a linear PD controller, the control variable is given by

$$u = k_e e + k_{\dot{e}} \frac{de}{dt}$$

where k_e and $k_{\dot{e}}$ are constants representing the proportional and derivative gains, respectively. For convenience, let $\frac{de}{dt}$ and $k_{\dot{e}}$ be denoted by r and k_r ,

respectively. These gains can be considered as the sensitivity of the control variable u to e and r , respectively (i.e., $k_e = \frac{\partial u}{\partial e}$ and $k_r = \frac{\partial u}{\partial r}$) (Haines and Hittle 2006). The purpose is to design a nonlinear

controller so that $\frac{\partial u}{\partial e}$ is not constant but an increasing function of e in the region $\{e \geq 0\}$ and a decreasing function of e in the region $\{e \leq 0\}$. This means that $\frac{\partial^2 u}{\partial e^2}$ must be nonnegative in the region

$\{e \geq 0\}$ and nonpositive in the region $\{e \leq 0\}$. The same thing must hold for $\frac{\partial u}{\partial r}$ and r .

$$\frac{\partial u}{\partial e} = k_e + \frac{\partial k_e}{\partial e} e + \frac{\partial k_r}{\partial e} r \quad (1)$$

$$\frac{\partial u}{\partial r} = \frac{\partial k_e}{\partial r} e + k_r + \frac{\partial k_r}{\partial r} r \quad (2)$$

$$\frac{\partial^2 u}{\partial e^2} = 2 \frac{\partial k_e}{\partial e} + \frac{\partial^2 k_e}{\partial e^2} e + \frac{\partial^2 k_r}{\partial e^2} r \quad (3)$$

$$\frac{\partial^2 u}{\partial r^2} = 2 \frac{\partial k_r}{\partial r} + \frac{\partial^2 k_r}{\partial r^2} r + \frac{\partial^2 k_e}{\partial r^2} e \quad (4)$$

DESIGN OF A NONLINEAR VARIABLE GAIN FUZZY LOGIC CONTROLLER

A block diagram of a PD fuzzy controller is shown in Fig. 1 (Passino and Yurkovich 1998). The proposed fuzzy controller uses two identical input fuzzy sets, namely Positive (\tilde{P}) and Negative (\tilde{N}). The membership functions of these fuzzy sets are

$$\mu_{\tilde{P}}(x) = \begin{cases} 0 & \text{when } x < -1 \\ \frac{1}{2}(x+1) & \text{when } -1 \leq x \leq 1 \\ 1 & \text{when } x > 1 \end{cases},$$

$$\mu_{\tilde{N}}(x) = \begin{cases} 1 & \text{when } x < -1 \\ \frac{1}{2}(-x+1) & \text{when } -1 \leq x \leq 1 \\ 0 & \text{when } x > 1 \end{cases}$$

where x is the input variable $k_1 e$ or $k_2 \frac{de}{dt}$, where k_1 and k_2 are scaling factors.

Three output fuzzy sets, namely Positive (\tilde{P}), Zero (\tilde{Z}), and Negative (\tilde{N}) are used. They are of singleton type and their nonzero values are at 1, 0, and -1, respectively. The input and output fuzzy sets are shown in Fig.2

The fuzzy controller uses the following four fuzzy rules:

IF e is Positive AND r is Positive THEN u is Positive

IF e is Positive AND r is Negative THEN u is Zero

IF e is Negative AND r is Positive THEN u is Zero

IF e is Negative AND r is Negative THEN u is Negative

Using the Zadeh fuzzy AND operator, the Lukasiewicz fuzzy OR operator, and the center-average defuzzification technique, the analytical structure of the fuzzy controller can be derived. To focus the analysis of the fuzzy controller to the region near the equilibrium point $(k_1 e, k_2 r) = (0, 0)$, only the square region $[-1, 1] \times [-1, 1]$ of the $k_1 e - k_2 r$ phase plane will be considered. The controller output is

$$u = \begin{cases} \frac{1}{4 - 2k_1|e|} (k_1 e + k_2 r) & \text{When } k_2|r| \leq k_1|e| \\ \frac{1}{4 - 2k_2|r|} (k_1 e + k_2 r) & \text{When } k_1|e| \leq k_2|r| \end{cases}$$

The following analysis shows that for this fuzzy controller the partial derivatives in eq (3) and eq(4) are nonnegative in the region $k_2|r| \leq k_1|e|$. A similar analysis can be carried out for the region $k_1|e| \leq k_2|r|$.

$$k_e = \frac{k_1}{4 - 2k_1|e|} \quad \text{and} \quad k_r = \frac{k_2}{4 - 2k_1|e|} \quad \text{where } k_e \text{ and } k_r \text{ are positive in } [-1, 1] \times [-1, 1]$$

$$\frac{\partial k_e}{\partial e} = \frac{2k_1^2 \operatorname{sgn}(e)}{(4 - 2k_1|e|)^2}, \quad \frac{\partial k_r}{\partial e} = \frac{2k_1 k_2 \operatorname{sgn}(e)}{(4 - 2k_1|e|)^2},$$

$$\frac{\partial^2 k_e}{\partial e^2} = \frac{8k_1^3 \operatorname{sgn}^2(e)(4 - 2k_1|e|)}{(4 - 2k_1|e|)^4}$$

$$\frac{\partial^2 k_r}{\partial e^2} = \frac{8k_1^2 k_2 \operatorname{sgn}^2(e)(4 - 2k_1|e|)}{(4 - 2k_1|e|)^4}$$

DESIGN OF A VARIABLE GAIN NONLINEAR FUZZY CONTROLLER AND PERFORMANCE ENHANCEMENT DUE TO GAIN VARIATION

$$\frac{\partial k_e}{\partial r} = \frac{\partial k_r}{\partial r} = \frac{\partial^2 k_e}{\partial r^2} = \frac{\partial^2 k_r}{\partial r^2} = 0$$

Substituting the above expressions of the partial derivatives in eq(1) through eq(4) yields

$$\frac{\partial u}{\partial e} = \frac{k_1}{4 - 2k_1|e|} + \frac{2k_1 \operatorname{sgn}(e)}{(4 - 2k_1|e|)^2} (k_1 e + k_2 r)$$

$$\frac{\partial u}{\partial r} = \frac{k_2}{4 - 2k_1|e|}$$

$$\frac{\partial^2 u}{\partial e^2} = 4 \frac{k_1^2 \operatorname{sgn}(e)}{(4 - 2k_1|e|)^2} + \frac{8k_1^2 \operatorname{sgn}^2(e)(4 - 2k_1|e|)}{(4 - 2k_1|e|)^4} \times (k_1 e + k_2 r) \quad (5)$$

$$\frac{\partial^2 u}{\partial r^2} = 0 \quad (6)$$

For $e > 0$, $\operatorname{sgn}(e) = 1 > 0$, $|e| = e$, and

$$k_2|r| \leq k_1|e| \Rightarrow k_2|r| \leq k_1 e \Rightarrow -k_1 e \leq k_2 r \leq k_1 e \\ \Rightarrow 0 \leq k_1 e + k_2 r \leq 2k_1 e$$

Since each term of the left hand side of eq.(5) is

nonnegative, this implies that $\frac{\partial^2 u}{\partial e^2}$ is nonnegative. It

is clear from eq.(6) that $\frac{\partial^2 u}{\partial r^2} = 0$ implies that

$$\frac{\partial^2 u}{\partial r^2} \geq 0, \text{ i.e., } \frac{\partial^2 u}{\partial r^2} \text{ is nonnegative.}$$

For $e < 0$, $\operatorname{sgn}(e) = -1 < 0$, $|e| = -e$, and

$$k_2|r| \leq k_1|e| \Rightarrow k_2|r| \leq -k_1 e \Rightarrow k_1 e \leq k_2 r \leq -k_1 e \\ \Rightarrow 2k_1 e \leq k_1 e + k_2 r \leq 0$$

Since each term of the left hand side of eq.(5) is

nonpositive, this implies that $\frac{\partial^2 u}{\partial e^2}$ is nonpositive. It

is clear from eq.(6) that $\frac{\partial^2 u}{\partial r^2} = 0$ implies that

$$\frac{\partial^2 u}{\partial r^2} \leq 0, \text{ i.e., } \frac{\partial^2 u}{\partial r^2} \text{ is nonpositive.}$$



Fig. 3 and **Fig. 4** show the graphs of $\frac{\partial u}{\partial e}$ and $\frac{\partial u}{\partial r}$ as functions of $k_1 e$ and $k_2 r$, respectively (without loss of generality, k_1 and k_2 were assumed to be 1). These surfaces are valid only above the region $k_2 |r| \leq k_1 |e|$. It is obvious from **Fig. 3** that the surface of $\frac{\partial u}{\partial e}$ is discontinuous at $(k_1 e, k_2 r) = (0, 0)$ because of the discontinuity of $\text{sgn}(e)$ at $e = 0$.

A block diagram of a PI fuzzy controller is shown in **Fig. 5** (Passino and Yurkovich 1998) (Reznik 1997).

The structure of the PI fuzzy controller is the same as that of the PD fuzzy controller except that the

derivative input $\frac{de}{dt}$ in the PD fuzzy controller is

replaced by the integral input $\int_0^t e dt$ in the PI fuzzy

controller. Therefore, if $\frac{de}{dt}$ is replaced by $\int_0^t e dt$ in

the above design and analysis, the result is a PI fuzzy controller.

SIMULATION RESULTS

Since fuzzy control has the potential to outperform linear control when nonlinear systems or systems that have time delay are involved (Ying 2000 –1), the above PD and PI fuzzy controllers are used to control such systems.

Controlling a Nonlinear Plant

Most real plants have nonlinear dynamics. A common nonlinear functions that appear in process dynamic models are enthalpy as a function of temperature, fluid flow as a function of pressure drop, radiation heat transfer rate as a function of temperature,...etc (Smith and Corripio 2005). The nonlinear plant that is used in this simulation is a nonlinear mass-spring-damper system shown in **Fig. 6** (Lam, Leung, and Tam 2001). The dynamic of this plant is given by

$$\ddot{x}(t) = -\dot{x}(t) - 0.01x(t) - 0.1x(t)^3 + (1.4387 - 0.13\dot{x}(t)^2)u(t)$$

Fig. 7 (**Fig. 8**) shows a step response comparison of this plant when a nonlinear PD (PI) fuzzy controller and a conventional PID controller are used. **Table 1**

shows the time domain performance characteristics for these responses. The PI fuzzy controller has a large overshoot since it lacks the derivative term in its structure. However, the PD fuzzy controller still outperforms the PID controller.

Controlling a Plant with Time Delay

Many industrial processes can be approximated by first-order dynamics and a time delay (Astrom 1997) (Landau, and Zito 2006) (Chen and Pham 2001) (Ogata 1010) (Fadali 2009). The steering control of a moon vehicle is an example of a plant that has a time delay (Dorf and Bishop 2008). The dynamics of the plant is given by

$$0.2\dot{\theta}(t) + \theta(t) = 2u(t - 0.1)$$

Fig. 9 (**Fig. 10**) shows a step response comparison of this plant when a nonlinear PD (PI) fuzzy controller and a conventional PID controller are used. **Table 2** shows the time domain performance characteristics for these responses. It is obvious that the two fuzzy controllers outperform the PID controller.

CONCLUSIONS

Fuzzy control and conventional PID control produce the same control performance for linear systems. Therefore, using fuzzy control should be avoided in such cases since a fuzzy controller has many more design parameters than a PID controller which has only three design parameters and its design and implementation is effective and efficient. However, PID control may not generate satisfactory control performance if the plant is nonlinear, time varying, or has time delay. In such cases, fuzzy control can outperform PID control, especially due to its variable gain characteristics. Simulation results show two cases where fuzzy control gives better performance characteristics than PID control.

REFERENCES

- Astrom, K. J. and Wittenmark, B., "Computer-controlled systems", Prentice Hall, 1997.
- Bonfè, M. and Mainardi, E., "A non linear fuzzy pid controller for robotic visual-servoing", Proceedings of Sixth Portuguese Conference on Automatic Control CONTROLO, 2004.

- Brdys, M. A. and Littler, J. J., "Fuzzy logic gain scheduling for non-linear servo tracking", *Int. J. Appl. Math. Comput. Sci.*, 2002, Vol.12, No.2, 209–219
- Chen, G., and Pham, T. T., "Introduction to fuzzy sets, fuzzy logic, and fuzzy control systems", CRC Press LLC, 2001.
- Dash, P. K., Morris, S., and Mishra, S., "Design of a nonlinear variable-gain fuzzy controller for FACTS devices", *IEEE Transactions on control systems technology*, vol 12, issue 3, 2004.
- Dorf, R. C. and Bishop, R. H., "Modern control systems", Pearson Prentice Hall, 2008.
- Driankov, D., Hellendoorn, H., and Reinfrank, M., "An introduction to fuzzy control", Springer, 1996.
- Fadali, M.S., "Digital control engineering", Elsevier, 2009.
- Haines, R. W. and Hittle, D. C., "Control systems for heating, ventilating, and air conditioning", Springer, 2006.
- Jantzen, J., "Foundations of fuzzy control", John Wiley and sons, 2007.
- Lam, H. K., Leung, F. H. F., and Tam, P. K. S., "Nonlinear state feedback controller for nonlinear systems: stability analysis and design based on fuzzy plant model", *IEEE Transactions on fuzzy systems*, vol. 9, no. 4, August 2001.
- Landau, I. D. and Zito, G., "Digital control systems", Springer, 2006.
- Chen, C. "Analog and digital control system design", Oxford University Press, 2006.
- Miloudi, A., Draou, A., and AlRadadi, E. A., "Variable Gain PI Controller Design For Speed Control and Rotor Resistance Estimation of an Indirect Vector Controlled Induction Machine Drive", in *Proc. IECON.02*, Sevilla, Spain, Nov. 5.8, 2002, pp. 323-328.
- Ogata, K., "Modern control engineering", Prentice Hall, 2010.
- Passino, K. M. and Yurkovich, S., "Fuzzy control", Addison-Wesley, 1998.
- Reznik, L., "Fuzzy controllers", Newnes, 1997.
- Smith, C. A. and Corripio, A. B., "Principles and practice of automatic process control", John Wiley and sons, 2005.
- Ying, H., "TITO Mamdani Fuzzy PI/PD Controllers as Nonlinear, Variable Gain PI/PD controllers", *International Journal of Fuzzy Systems*, Vol. 2, No. 3, September. 2000.
- Ying, H., "Fuzzy control and modeling", IEEE Press, 2000.
- <http://www.emersonprocess.com/systems/support/documentation/provox/docvue/index.asp?path=../docvue/Advanced%20Control/>

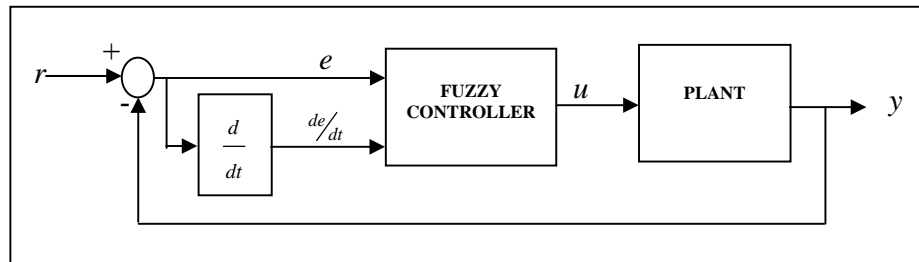


Fig. 1: A block diagram of a PD fuzzy controller.

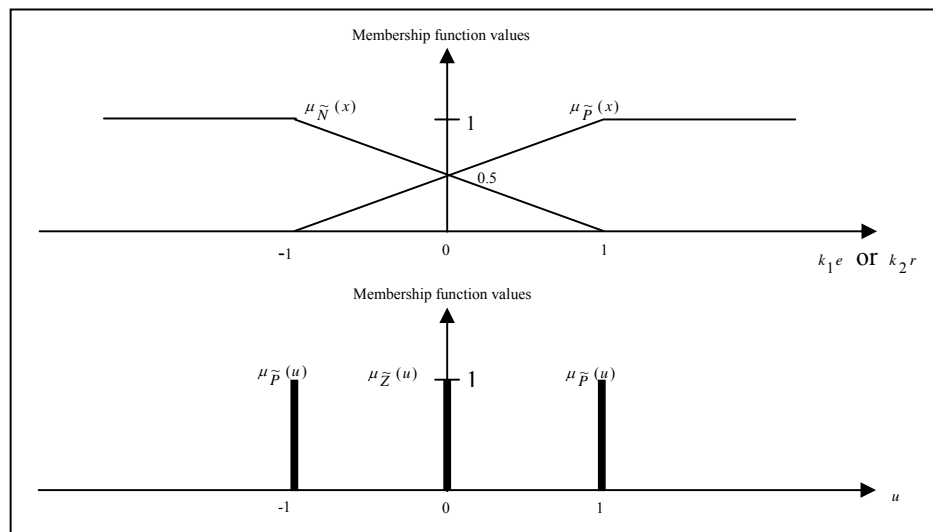


Fig. 2: The input and output fuzzy sets.

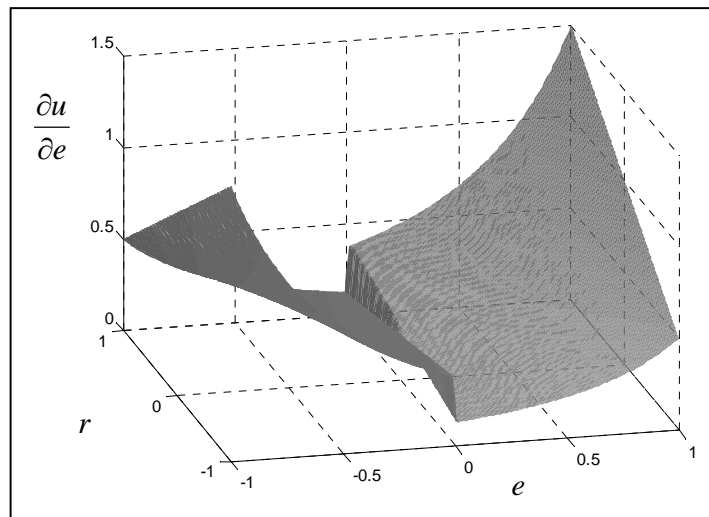


Fig. 3: Graph of $\frac{\partial u}{\partial e}$ as functions of $k_1 e$ and $k_2 r$.

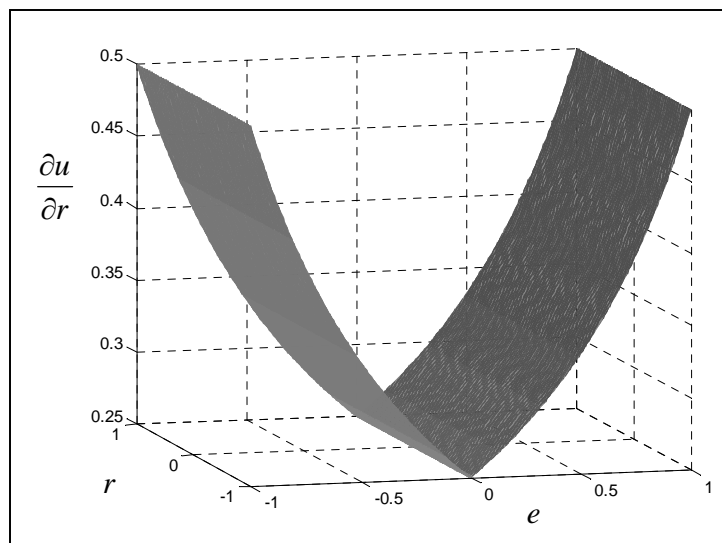


Fig. 4 Graph of $\frac{\partial u}{\partial r}$ as functions of $k_1 e$ and $k_2 r$.

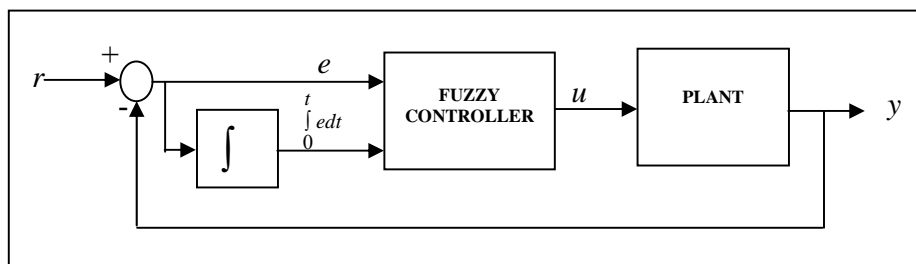


Fig. 5: A block diagram of a PI fuzzy controller (version 1)

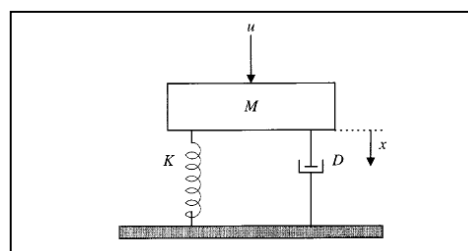


Fig. 6: A nonlinear mass-spring-damper system

Table 1: Time domain performance characteristics for the nonlinear plant

Type of controller	PD fuzzy Fig. 7	PI fuzzy Fig. 8	PID
Performance characteristics			
Rise time (sec)	0.92	0.48	1
Percentage overshoot	0	56.3944	6.7093
Settling time (2%) (sec)	2.4	11.76	3.38

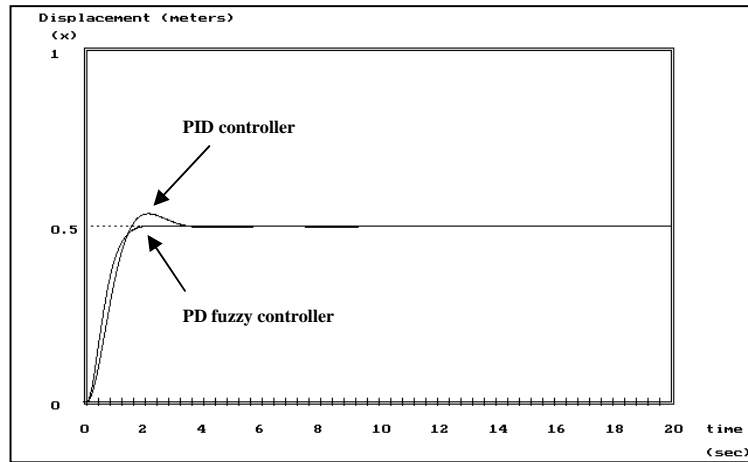


Fig. 7: Step response of the nonlinear plant using a nonlinear PD fuzzy controller and a conventional PID controller.

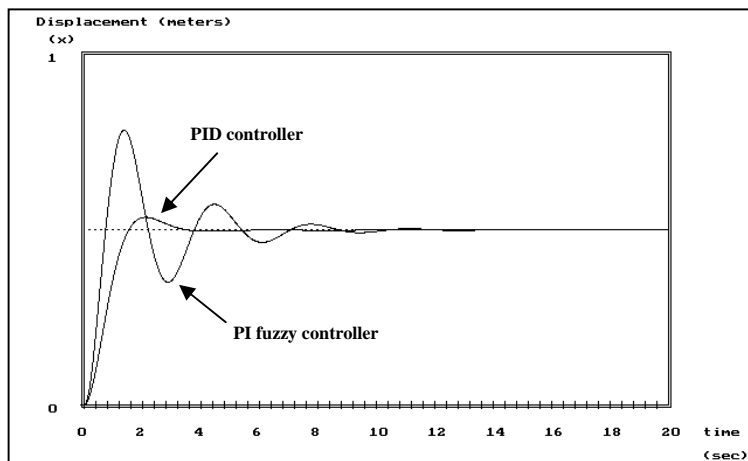


Fig. 8: Step response of the nonlinear plant using a nonlinear PI fuzzy controller and a conventional PID controller.

Table 2: Time domain performance characteristics for the plant with time delay

Type of controller	PD fuzzy Fig. 9	PI fuzzy Fig. 10	PID
Performance characteristics			
Rise time (sec)	0.46	0.38	1.08
Percentage overshoot	0	0	0.2505
Settling time (2%) (sec)	0.74	0.96	1.92

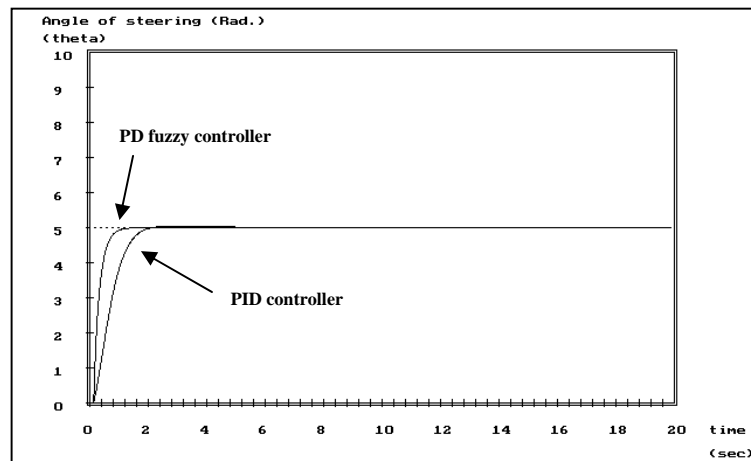


Fig. 9: Step response of the plant with time delay using a nonlinear PD fuzzy controller and a conventional PID controller.

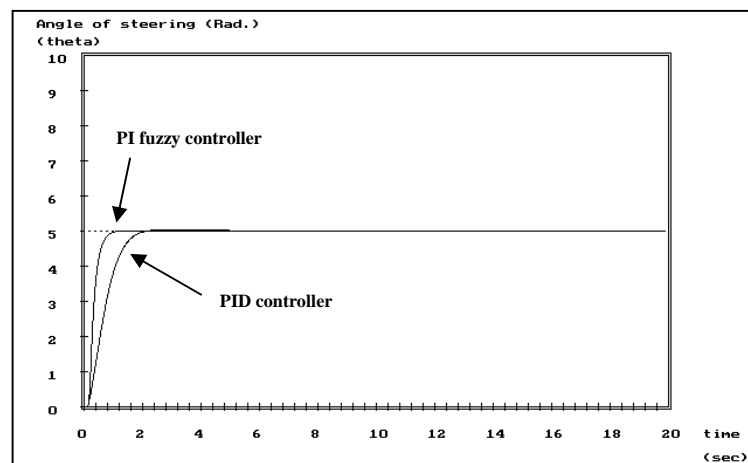


Fig. 10: Step response of the plant with time delay using a nonlinear PD fuzzy controller and a conventional PID controller.



GENERATION AND TOOTH CONTACT ANALYSIS (TCA) OF HYPOID GEAR DRIVE

Assist. Prof. Mohammad Q. Abdullah
Dep. Of Mech.
College of Engineering
University of Baghdad

Nassear R. Hmoad

ABSTRACT

The present work covers the Face-Hobbing method for generation and simulation of meshing of Face hobbed hypoid gear drive. In this work the generation process of hobbed hypoid gear has been achieved by determination of the generation function of blade cutter. The teeth surfaces have been drawn depending on the simulation of the cutting process and the head cutter motion. Tooth contact analysis (TCA) of such gear drive is presented to evaluate analytically the transmission error function for concave and convex tooth side due to misalignment errors. TCA results show that the gear is very sensitive to misalignment errors and the increasing of the gear teeth number decrease the transmission error for both concave and convex tooth sides and ensure smooth motion with low vibration.

KEYWORD

Hypoid, Generation, Tooth Contact Analysis (TCA).

Introduction:

Generation of hypoid bevel gears depends upon the theory of derivation of gear and pinion tooth surface. The accurate geometrical representation of gear tooth surface is the first step to design a successful gear drive. This paper presents a mathematical model able to compute the tooth surface of hypoid gear drive cut by face-hobbing method (FH). At first a brief discussion about kinematic relationships of FH process and about the main characteristics of face-hobbed tooth cutting tools will be proposed. Then the cutting tools will be described analytically, after that according to the theory of gearing the cutting process will be simulated and gear tooth surface will be derived.

1- Face Hobbing Method:

In Fig. (1) FH process are shown schematically. The head cutter is provided with (N_c) groups of blade. Each group contains three blades, one for rough cutting and two finishing blades one for each tooth side [F. L. Litvin , 1991]. To accomplish continuous indexing, the head cutter and the being cut gear are rotated in opposite directions. While the head cutter is rotated by the angle ($2\pi/N_c$) the gear is rotated through the angle ($2\pi/N_f$), where (N_f) is gear or pinion teeth number. Thus the next group of blades will start to cut the next gear tooth

after finishing the current tooth, according to that the rotation of the cutter (θ_c) is related to that of work piece(θ_f) by the ratio (R_b).

$$R_b = N_c/N_f = \theta_f/\theta_c \quad (1)$$

2- Analytical Description of Cutting Blade Geometry:

The analytical description will be focused on the two finishing blades only, which shaped the gear tooth surfaces. Fig. (2) shows, from two different viewpoints, the location of one blade group in Gleason Tri-ac left-handed (LH) head cutter. A left-handed gear or pinion is cut by a (LH) head cutter [V. Simon and U. L. Hungary, 2000]. Fig. (3) shows the outer and inner cutting blades of straight edge without filet. There are three reference coordinate systems to specify the blade geometry as below.

1. S_c - Fixed at the pitch point (P) and its axes parallel to the edge of the tool blank.
2. S_b - Its origin at (P), (x_b) coinciding with (x_c), (y_b) and (z_b) having hook angle (η_b) with(y_c) and (z_c).
3. z_c - Its origin has been setup at the tip of the blade and its

components parallel to (s_b) components.

(α_e) presents blade angle (pressure angle) between the projection of the cutting edge on $(x_e z_e)$ plane and (z_e) . The cutting edge lies entirely on a plane, called rake plane, which forms rake angle (k_e) , usually equal to 12° , with tool blank plane having as normal the (y_e) axis. Hook angle (η_b) , usually equal to 4.42° , represent the direction of cutting blade with respect to the head cutter rotation axis (z_h) . The eccentric angle (ε_b) is the angle between (s_b) and (s_h) coordinate systems.

At first a vector (c_e) oriented along the cutting edge and pointing from point (P) to the blade tip will be defined in (s_h) system. The upper sign refers to the outer blade and the lower one refers to inner blade, [V. Simon and U. L. Hungary, 2000]

$$c_e = \begin{bmatrix} \pm \sin(\alpha_e) \\ \sin(\alpha_e) \tan(k_e) \\ \cos(\alpha_e) \end{bmatrix} \quad (2)$$

The normal unit vector to rake plane is.

$$n_e = \begin{bmatrix} \pm \sin(k_e) \\ -\cos(k_e) \\ 0 \end{bmatrix} \quad (3)$$

The representations of c_e, n_e, α_e , and k_e in (s_b) system are [V. Simon and U. L. Hungary, 2000].

$$c_b = \begin{bmatrix} c_{bx} \\ c_{by} \\ c_{bz} \end{bmatrix} = \begin{bmatrix} 1 & 0 & 0 \\ 0 & \cos(\eta_b) & -\sin(\eta_b) \\ 0 & \sin(\eta_b) & \cos(\eta_b) \end{bmatrix} c_e \quad (4)$$

$$n_b = \begin{bmatrix} n_{bx} \\ n_{by} \\ n_{bz} \end{bmatrix} = \begin{bmatrix} 1 & 0 & 0 \\ 0 & \cos(\eta_b) & -\sin(\eta_b) \\ 0 & \sin(\eta_b) & \cos(\eta_b) \end{bmatrix} n_e \quad (5)$$

$$\alpha_b = \tan^{-1}(\pm c_{bx}/c_{bz}) = f(\alpha_e, k_e, \eta_b) \quad (6)$$

$$k_b = \tan^{-1}(\pm c_{by}/c_{bx}) = f(\alpha_e, k_e, \eta_b) \quad (7)$$

Eccentric angle found to be calculated as in Eq. (8), [F. L. Litvin, 1989]

$$\varepsilon_b = \sin^{-1}(N_e r_i \cos(\beta_i)/(N_i * r_b)) \quad (8)$$

Where (r_i) presents gear radius if $(i=1)$ and

pinion radius if $(i=2)$, and (β) is spiral

angle, r_b is the cutter radius. The measured

c_b, n_b and α_b in s_h systems are.

$$c_h = \begin{bmatrix} c_{hx} \\ c_{hy} \\ c_{hz} \end{bmatrix} = \begin{bmatrix} \cos(\varepsilon_b) & \sin(\varepsilon_b) & 0 \\ -\sin(\varepsilon_b) & \cos(\varepsilon_b) & 0 \\ 0 & 0 & 1 \end{bmatrix} c_b \quad (9)$$

$$n_h = \begin{bmatrix} n_{hx} \\ n_{hy} \\ n_{hz} \end{bmatrix} = \begin{bmatrix} \cos(\varepsilon_b) & \sin(\varepsilon_b) & 0 \\ -\sin(\varepsilon_b) & \cos(\varepsilon_b) & 0 \\ 0 & 0 & 1 \end{bmatrix} n_b \quad (10)$$

$$\alpha_h = \tan^{-1}(\pm c_{hx}/c_{hz}) = f(\alpha_s, k_s, \eta_b, \varepsilon_b) \quad (11)$$

The above eq.s are the analytical description of cutting blade geometry. Fig. (4) shows more complex blade shape consists of four sections and these sections are.

- (I)- Bottom: straight horizontal segment.
- (II)- Fillet: circular arc of radius (r_s , fillet radius) and center at (R).
- (III)- Toprem: straight inclined segment with length (L_T) and angle (τ).
- (IV)- Curved blade: a circular arc with radius (ρ) and center at point (O).

The coordinates of (P) are [V. Simon and U. L. Hungary, 2000].

Where the upper sign refers to right side of the plade and the lower sign refers to the left side of the plade

$$\left. \begin{aligned} x_p &= \pm h_f \tan(\alpha_b) \\ y_p &= -h_f \tan(\alpha_b) \tan(k_b) \end{aligned} \right\} \quad (12)$$

$$z_p = -h_f$$

Point (A) the intersection of (x_t) with the toprem section there for the distance of (OA) is

$$OA = \sqrt{\rho_t^2 + L_T^2 - 2\rho_t L_T \cos(\frac{\pi}{2} - \tau)} \quad (13)$$

Where (ρ_t) is the projection of (ρ) on

(x_t, z_t) plane and (τ) is toprem angle.

$$A\bar{O}B = \sin^{-1}(L_T \sin(\pi/2 - \tau)/OA) \quad (14)$$

The intersection of the circular arc with the Toprem occurs at point (B). The angle between (OA) and (x_t) is, [V. Simon and U. L. Hungary, 2000]

$$\lambda = \sin^{-1}(z_o/OA) \quad (15)$$

Then the coordinates of (A) are

$$\left. \begin{aligned} x_A &= x_o \pm OA \cos(\lambda) \\ z_A &= 0 \\ y_A &= 0 \end{aligned} \right\} \quad (16)$$

$$\delta = \lambda + A\tilde{O}B \quad (17)$$

$$\gamma = \pi/2 - (\delta - \tau) \quad (18)$$

$$L_1 = r_e \gamma \quad (19)$$

$$\left. \begin{aligned} x_R &= x_A \pm r_e \tan(\gamma/2) \\ z_R &= -r_e \end{aligned} \right\} \quad (20)$$

Toprem length can be calculated as

$$L_2 = L_T - r_e \tan(\gamma/2) \quad (21)$$

The calculation of cutting edge in (s_c) system depends on the blade section to be calculated, Table (1) propose the calculation of blade sections in (s_c) .

All points of cutting edge lie in the rake plane and (y_c^p) can be obtained as

$$y_c^p(s) = y_p z + \left[\left(x_p - x_c^p(s) \right) n_{bx} + \left(z_p - z_c^p(s) \right) n_{bz} \right] / n_{by} \quad (22)$$

And the cutting blade representation in head cutter center is

$$r_c^p(s) = \begin{bmatrix} r_b + (x_c^p(s) - x_p) \cos(\varepsilon_b) + (y_c^p(s) - y_p) \sin(\varepsilon_b) \\ -(x_c^p(s) - x_p) \sin(\varepsilon_b) + (y_c^p(s) - y_p) \cos(\varepsilon_b) \\ z_c^p(s) - x_p \end{bmatrix} \quad (23)$$

3- Simulation of FH Cutting Process:

Eq. (23) represents the principle point to start the simulation process.

According to gearing theory the proper coordinate transformation able to simulate the cutting process and compute the gear drive teeth surfaces. Simulation process has two forms depending upon generating or non-generating cutting process.

3.1- FH Cutting Process Without Generation:

Fig. (5) show FH cutting machine which is setup to cut format gear member. A proper set of reference frames has to be introduced in order to describe the machine setting. There are three machine reference coordinate systems (s_h) which has been specified previously, (s_m) its origin at (O_m) and (z_m) parallel to (z_h) , (s_w) which has been setup with its origin at (O_w) , gear apex) where (z_w) coincides with the gear rotation axis. When the cutter rotates by angle (θ) gear rotation will be $(R_p \theta)$ condition of continuous indexing.

Gleason saved files (SAF) provides the details to properly locate, with respect to reference frame (s_m) machine root angle (γ_m) and machine center to back (Δx_p) . The setting (H) and (I) found to be a function of gear drive shape parameters as in eq.s (24) and (25), [F. L. Litvin et al, 1991].

$$V = r_b \cos(\beta - \varepsilon_b) \quad (24)$$

$$H = (r_i / \sin(\gamma_m)) - r_b \sin(\beta - \varepsilon_b) \quad (25)$$

Finally the representation of gear tooth surfaces is

$$r_2^p(\theta, s) = M_{w2} M_{2m} M_{m1} M_{1h} r_h^p(s) \quad (26)$$

where

$$M_{m1} = \begin{bmatrix} \cos\theta & \sin\theta & 0 \\ -\sin\theta & \cos\theta & 0 \\ 0 & 0 & 1 \end{bmatrix},$$

$$M_{m1} = \begin{bmatrix} 1 & 0 & 0 \\ 0 & 1 & 0 \\ 0 & 0 & 1 \end{bmatrix} + \begin{bmatrix} H \\ \pm V \\ 0 \end{bmatrix}$$

$$M_{2m} = \begin{bmatrix} \cos(\frac{\pi}{2} - \gamma_m) & 0 & \sin(\frac{\pi}{2} - \gamma_m) \\ 0 & 1 & 0 \\ -\sin(\frac{\pi}{2} - \gamma_m) & 0 & \cos(\frac{\pi}{2} - \gamma_m) \end{bmatrix} + \begin{bmatrix} 0 \\ 0 \\ -\Delta x_p \end{bmatrix}$$

,

$$M_{w2} = \begin{bmatrix} \cos(R_b\theta) & \sin(R_b\theta) & 0 \\ -\sin(R_b\theta) & \cos(R_b\theta) & 0 \\ 0 & 0 & 1 \end{bmatrix}$$

In Fig. (6) a non-generated gear blank is drawn depending upon eq. (26) by using the Gleason SAF details ($\gamma_m, \Delta x_p$).

The normal vector to these surfaces which is used to analyze tooth contact analysis is

$$n_2^p(\theta, s) = \frac{\partial}{\partial s} r_w^p(\theta, s) \times \frac{\partial}{\partial \theta} r_w^p(\theta, s) \quad (27)$$

3.2- FH Cutting Process with Generation Motion:

Theoretically FH with generation motion is based on a generalized concept of bevel gear generation in which the pinion is generated by a complementary generation crown gear. The tooth surfaces of the generating crown gear are kinematically formed by the traces of the head cutter edge and the cradle rotation, [Dr.Qi Fan, 2007], cradle is a mechanical element centered at (O_m) and carrying the head cutter. In generated FH method there are two sets of related motion are defined. The first set was specified in eq. (1), the second set presents the rotation of the cradle and the pinion as below

$$R_a = N_g / N_1 = \theta_1 / \phi \quad (28)$$

(R_a) represents the roll ratio, (N_g) is the

generating crown gear teeth number, (ϕ) is

the crown gear rotation. Fig. (7) show FH cutting machine which is ready to cut the generated pinion. It is seen that the reference coordinate systems (s_h), (s_m) and (s_c) have been rigidly connected respectively to the head cutter, machine center and work piece. The (s_c) system rigidly connect to the cradle. The rotation of

pinion is a function of (θ) and cradle

rotation (ϕ) .

$$\theta_1 = R_b \theta + R_a \phi \quad (29)$$

Radial setting (s_r) and cradle angle (q) can be computed as in eq.s (30) and (31).

$$s_r = \sqrt{H^2 + V^2} \quad (30)$$

$$q = \tan^{-1}(V/H) \quad (31)$$

The Gleason SAF kept the values of (R_a) and of all the setting to properly locate, with respect to the reference frame (s_m) , the pinion setting

E_m : pinion offset, γ_m : machine root angle, Δx_b : sliding base, i : tilt angle j : swivel angle

The cutting edges representation in (s_w) is derived in eq. (32)

$$r_1^p(\theta, \phi, s) = M_{w3} M_{34} M_{4m} M_{mc} M_{c3} M_{32} M_{21} M_{1h} r_h^p(s) \quad (32)$$

Where

$$M_{1h} = \begin{bmatrix} \cos \theta & \sin \theta & 0 \\ -\sin \theta & \cos \theta & 0 \\ 0 & 0 & 1 \end{bmatrix},$$

$$M_{21} = \begin{bmatrix} \cos i & 0 & \sin i \\ 0 & 1 & 0 \\ -\sin i & 0 & \cos i \end{bmatrix},$$

$$M_{32} = \begin{bmatrix} \cos j & \mp \sin j & 0 \\ \pm \sin j & \cos j & 0 \\ 0 & 0 & 1 \end{bmatrix}$$

$$M_{c3} = \begin{bmatrix} \cos(\frac{\pi}{2} - q) & \mp \sin(\frac{\pi}{2} - q) & 0 \\ \pm \sin(\frac{\pi}{2} - q) & \cos(\frac{\pi}{2} - q) & 0 \\ 0 & 0 & 1 \end{bmatrix} + \begin{bmatrix} 0 \\ \mp s_r \\ 0 \end{bmatrix}$$

,

$$M_{mc} = \begin{bmatrix} \cos \phi & \sin \phi & 0 \\ \sin \phi & \cos \phi & 0 \\ 0 & 0 & 1 \end{bmatrix}$$

$$M_{4m} = \begin{bmatrix} 1 & 0 & 0 \\ 0 & 1 & 0 \\ 0 & 0 & 0 \end{bmatrix} + \begin{bmatrix} 0 \\ \pm E_m \\ -\Delta x_b \end{bmatrix},$$

$$M_{34} = \begin{bmatrix} \cos(\frac{\pi}{2} - q) & 0 & \sin(\frac{\pi}{2} - q) \\ 0 & 1 & 0 \\ -\sin(\frac{\pi}{2} - q) & 0 & \cos(\frac{\pi}{2} - q) \end{bmatrix} + \begin{bmatrix} 0 \\ 0 \\ -\Delta x_p \end{bmatrix}$$

$$M_{w3} = \begin{bmatrix} \cos(R_b \theta + R_b \phi) & \sin \cos(R_b \theta + R_b \phi) & 0 \\ -\sin \cos(R_b \theta + R_b \phi) & \cos \cos(R_b \theta + R_b \phi) & 0 \\ 0 & 0 & 1 \end{bmatrix}$$

Eq. (32), unlike eq. (26), is not surface but represents family of surfaces. In order to drive the tooth surfaces it is necessary to calculate the set of points for whom, the eq. (33), which represents the tooth surface points, satisfied [F. L. Litvin et al, 1991].

$$\frac{\partial}{\partial s} r_1^p(\theta, \phi, s) \times \frac{\partial}{\partial \theta} r_1^p(\theta, \phi, s) \cdot \left(\frac{\partial}{\partial \phi} r_1^p(\theta, \phi, s) \right) = 0 \quad (33)$$

By using a proper values that satisfy eq. (32) and (33) each part of the tooth surface is generated. The normal vector to these surfaces is obtain by eq. (34)

$$\dot{r}_1^p(\theta, \phi, s) = \frac{\partial}{\partial s} r_1^p(\theta, \phi, s) \times \frac{\partial}{\partial \theta} r_1^p(\theta, \phi, s) \quad (34)$$

Fig. (8) shows hypoid pinion blank, the two meshed gears are shown in Fig. (9).

4 - Determination of Transmission Error:

The transmission function of an ideal gear drive is a linear one which is depends on ratio of gear teeth number

$$\theta_2 = \frac{N_1}{N_2} \theta_1 \quad (35)$$

Due to misalignment between the meshing gears the real transmission function $\theta_2(\theta_1)$ becomes piecewise periodic function with the period equal to the cycle of meshing of a pair of teeth. Due to The jump of angular velocity at the junction of cycles the acceleration approaches to large value of acceleration that cause large vibration and noise, for this reason it is necessary to predesign a parabolic function of transmission error that can absorb a linear function of transmission error and reduce the jump of angular velocity and acceleration [F. L. Litvin and Yi Zhang, 1991] and [F. L. Litvin, 2006]. The linear transmission function and the predesigned function are in tangency at the mean contact point and have the same derivative (m_{21}) at this point.

$$m_{12} = \partial\theta_2 / \partial\theta_1 = N_1 / N_2 \quad (36)$$

The predesigned transmission function is represented as

$$\theta_2 - \theta_2^{(0)} = F(\theta_1 - \theta_1^{(0)}) \quad (37)$$

Here $(\theta_1^{(0)})$ and $(\theta_2^{(0)})$ are the initial angles of rotation of pinion and gear that provide the tangency of gear tooth surfaces a mean contact point (M). By using the Taylor expansion up to the members of second order, [F. L. Litvin, 2006].

$$\begin{aligned} F(\theta_1 - \theta_1^{(0)}) &= \frac{\partial}{\partial \theta_1} F(\theta_1 - \theta_1^{(0)}) + .5 \frac{\partial^2}{\partial \theta_1^2} F(\theta_1 - \theta_1^{(0)}) \\ &= m_{21} (\theta_1 - \theta_1^{(0)}) + .5 \dot{m}_{21} \end{aligned} \quad (38)$$

(\dot{m}_{21}) is the to be chosen constant value: positive for the gear concave side, and negative for the gear convex side. The synthesized gears rotates with a parabolic function of transmission errors represented by

$$\Delta\theta_2(\theta_1) = .5 \dot{m}_{21} (\theta_1 - \theta_1^{(0)})^2 \quad (39)$$

Where

$$-\pi/N_1 \leq (\theta_1 - \theta_1^{(0)}) \leq \pi/N_2$$

Eq. (39) enables the determination of (\dot{m}_{21}) , considering as known the expected values of transmission errors [F. L. Litvin, 1989]. Eq. (39) has another form of second order

function [Dr. Q. Fan and Dr. L. Wilcox, 2006].

$$\Delta\theta_2(\theta_1) = a_t + b_t (\theta_1 - \theta_1^{(0)}) - c_t (\theta_1 - \theta_1^{(0)})^2 \quad (40)$$

5- Results and Discussions of Tooth Contact Analysis (TCA):

All the results of tooth contact that has been shown in Figs (11)–(19) specify the shape and magnitude of transmission errors for both tooth concave and convex side for different teeth number. These results are based on eq. (40) and by using the maximum transmission errors presented in [T. J. Maiuri, 2006], [V. Simon and U. L. Hungary, 2000]. The pinion has been shifted along its axis by $\pm\Delta P$ and also the misalignment can be achieved by changing the center distance ($\pm\Delta E$) which means the error of pinion shaft offset as shown in Fig. (9). The results show that the hypoid bevel gear is so sensitive to assembly errors, both misalignment procedures show that the transmission error functions have a linear or almost linear shape far away the mean contact point, the increasing of teeth number minimize the transmission error significantly and vibration will appear in every cycle of meshing. The misalignment for convex side is $\Delta E=0.508$ mm, $\Delta P=-0.254$ mm, and for concave side is $\Delta E=.254$ mm, $\Delta P=-0.102$ mm.

The gear and pinion machine- tool settings are shown in Table (3) and (4) respectively.

6- Conclusions:

The main conclusions obtained from the present work can be summarized as follow:

1. The modified mathematical model for tooth surface representation of face hobbled hypoid gear and its application for computerized design of these gears have been presented.
2. From tooth contact result its clear that:
 - i. The hypoid gear drive is very sensitive to misalignment of their meshing.
 - ii. The parabolic shape of transmission function have a linear shape far away the mean contact point.
 - iii. The increasing of gear teeth number minimizes the transmission errors and ensure smooth transmission performance and low noise.

REFERENCES

F. L. Litvin, (Theory of gearing), NASA publication, 1212, AVSCOM technical report, 88-c-035, 1989.

F. L. Litvin, W.S. Chaing, C. Kuan, M. Lundy and W. J. Tsung, (generation and geometry of hypoid gear member with face-hobbed tooth of uniform depth), IVSL / ELSEVIER, Int. J. Mach. Tools Manufact. Vol. 31, No. 2, pp. 167-181, 1991.

F. L. Litvin and Yi Zhang, (Local synthesis and tooth contact analysis of Face-Milled spiral bevel gears), NASA, Technical report 4342, 1991.

V. Simon, u. l. Hungary, (FEM stress analysis in hypoid gears), IVSL / PERGAMON, Mechanism and Machine theory, pp. 1197-1220, 2000.

Dr. Q. Fan and Dr. L. Wilcox, (New developments in tooth contact analysis (TCA) and loaded TCA for spiral bevel and

hypoid gear drives), Journal, Available on line at WWW.geartechnology.com , 2006.

T. J. Maiuri. (Spiral bevel and hypoid Gear cutting technology update), WWW.geartechnology.com 2006.

F. L. Litvin, (Development of gear technology and theory of gearing), University of Illinois at Chicago, Chicago, Illinois. NASA RP-1406, taken at 2006.

Dr. Q. Fan, (Kinematical simulation of face hobbing and tooth surface generation of spiral bevel and hypoid gears), Journal, Available on line at WWW.geartechnology.com, 2007.

NOMENCLATURES

Symbol	Description	Unit
c_b	Cutting edge description in S_b system	---
c_e	Cutting edge description in S_e system	---
c_h	Cutting edge description in S_h system	---
E_m	Pinion offset	mm
h_f	Blade height	mm
H	Machine horizontal setting	mm
i	Tilt angle	degree
j	Swivel angle	degree
n_b	Cutting edge unit normal in S_b	---
n_e	Cutting edge unit normal in S_e	---
n_h	Cutting edge unit normal in S_h	---
$n_1^p(\theta, \phi, s)$	Normal of pinion tooth surfaces	---
$n_2^p(\theta, s)$	Normal vector of gear tooth surfaces	---
N_1	Pinion tooth number	---
N_2	Gear tooth number	---
N_c	Cutting blade number	---
N_g	Crown gear teeth number	---
r_b	Cutter radius	mm
r_e	Filet radius	mm
$r_h^p(s)$	Description of deferent cutting sections	mm
$r_1^p(\theta, \phi, s)$	Pinion toot surfaces	mm



$r_2^p(\theta, s)$	Gear tooth surfaces	mm
R_b	Ratio of gear drive rotation	---
V	Machine vertical setting	mm
α_b	Pressure angle in S_b	degree
α_e	Pressure angle	degree
α_h	Pressure angle in S_h	degree
β_1	Pinion spiral angle	degree
β_2	Gear spiral angle	degree
γ	Cutting blade fillet angle	degree
γ_m	Pitch angle	degree
ε_b	Eccentric angle	degree
η_b	Hook angle	degree
$\theta_2^{(0)}, \theta_1^{(0)}$	Initial angle of rotation for gear and pinion	degree
$\Delta\theta_2(\theta_1)$	Error transmission function	degree
τ	Toprem angle	degree

Table (1), calculation of different blade sections in (s_e) coordinate system.

Blade part	p	s^p	$\begin{Bmatrix} x_e^p(s) \\ z_e^p(s) \end{Bmatrix}$
Bottom	I	$s^I \leq 0$	$\begin{Bmatrix} \pm s^I + x_R \\ 0 \end{Bmatrix}$
Fillet	II	$0 \leq s^{II} \leq L_1$	$\begin{Bmatrix} x_R \pm r_e \sin(s^{II}/r_e) \\ -r_e(1 - \cos(s^{II}/r_e)) \end{Bmatrix}$
Toprem	III	$L_1 \leq s^{III} \leq L_1 + L_2$	$\begin{Bmatrix} x_R \pm r_e \sin(s^{III}/r_e) \pm (s^{III} - L_1) \sin(\delta - \tau) \\ -r_e(1 - \cos(s^{III}/r_e)) - (s^{III} - L_1) \cos(\delta - \tau) \end{Bmatrix}$
Curved blade	IV	$L_1 + L_2 \leq s^{IV}$	$\begin{Bmatrix} x_O \pm \rho_t \cos(\delta + (s^{IV} - L_1 - L_2)/\rho_t) \\ z_O - \rho_t \sin(\delta + (s^{IV} - L_1 - L_2)/\rho_t) \end{Bmatrix}$

Table (2), Hypoid gear design data.

	Pinion	Gear
Number of teeth	12	30
Module (mm)	6	6
Running offset (mm)	15	
Outside diameter (mm)	72	180
Face width (mm)	31	27
Mean spiral angle (deg.)	30	20
Pitch angle (deg.)	18.5	71.5



Table (3), Gear machine- tool settings.

Cutter radius (mm).	75.184
Cutter blade angle (deg.)	17
Point width (mm)	2.032
Basic machine root angle γ_m (deg.)	64.5986
Machine center to back (ΔX_p) (mm)	2.358

Table (4), Pinion machine- tool setting,(for concave and convex side)

Setting	Value
Cutter radius (mm)	75.5
Cutter blade angle (deg.)	17
Machine root angle (deg.)	-3.44
Basic tilt angle (deg.)	21.22
Basic swivel angle (deg.)	-34.18
Basic cradle angle (deg.)	79.81
Sliding base setting (deg.)	16.498
Machine center to back (mm)	-1.117
Blank offset setting (mm)	23.411
Ratio of roll	3.5510

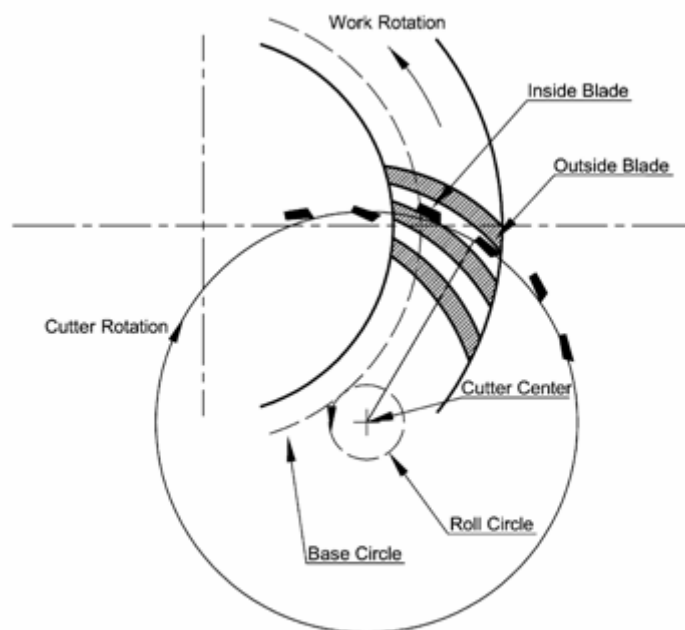


Fig. (1). Face Hobbing process

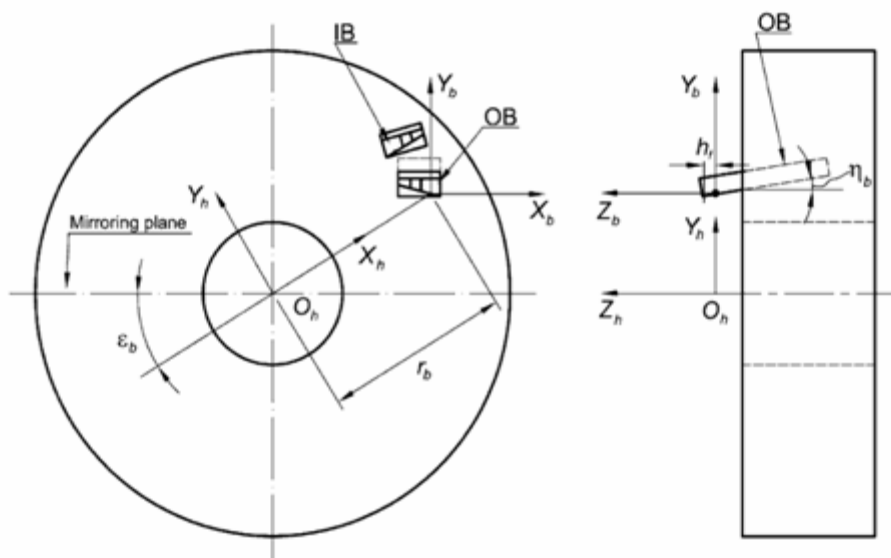


Fig. (2), LH blade group mounted in the head cutter .

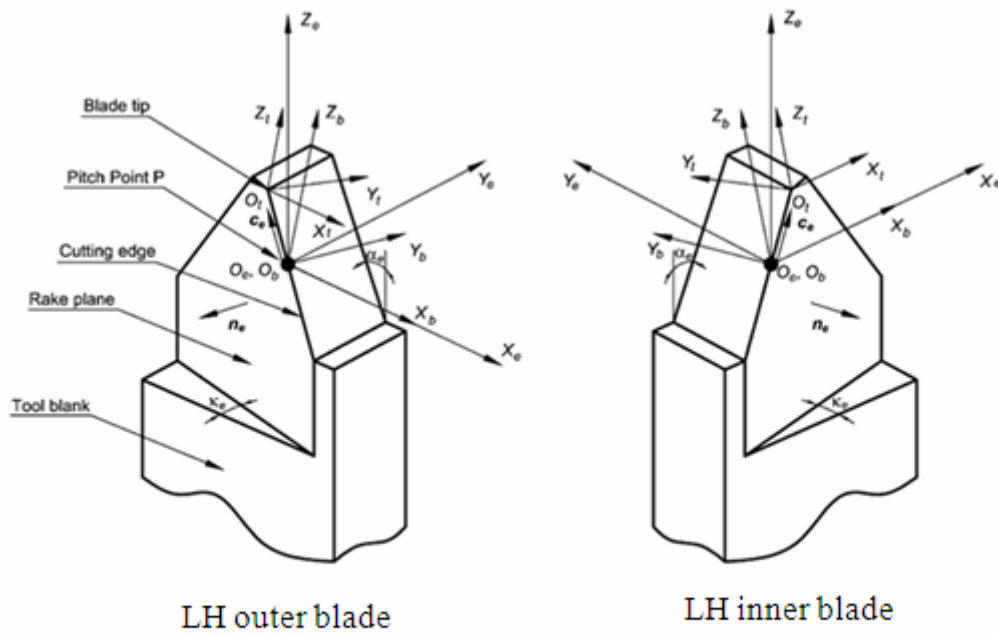


Fig. (3), LH group blades .

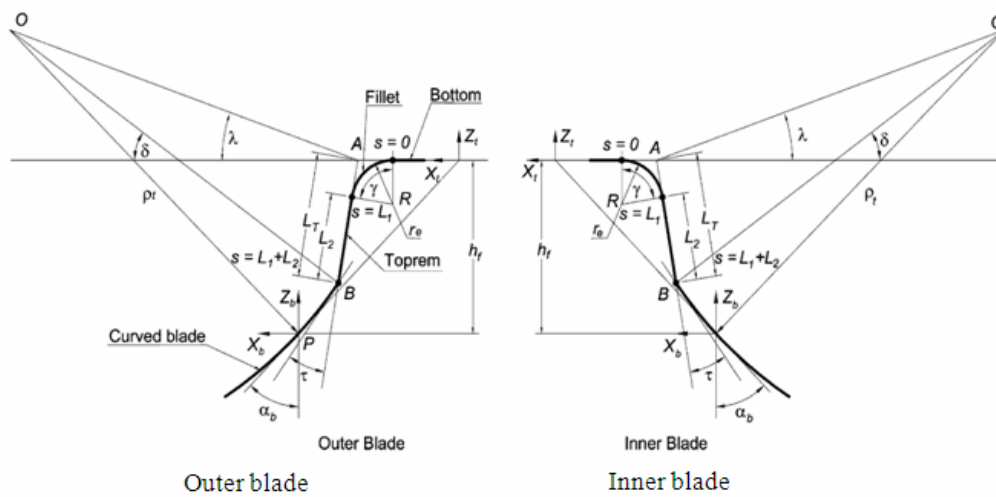


Fig. (4) projection of the curved LH on x_t, z_t plane .

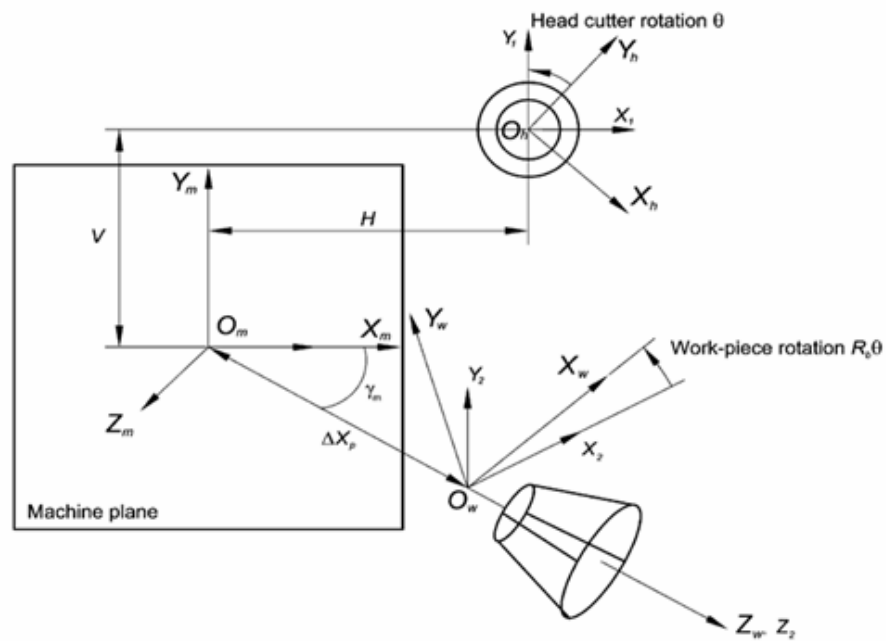
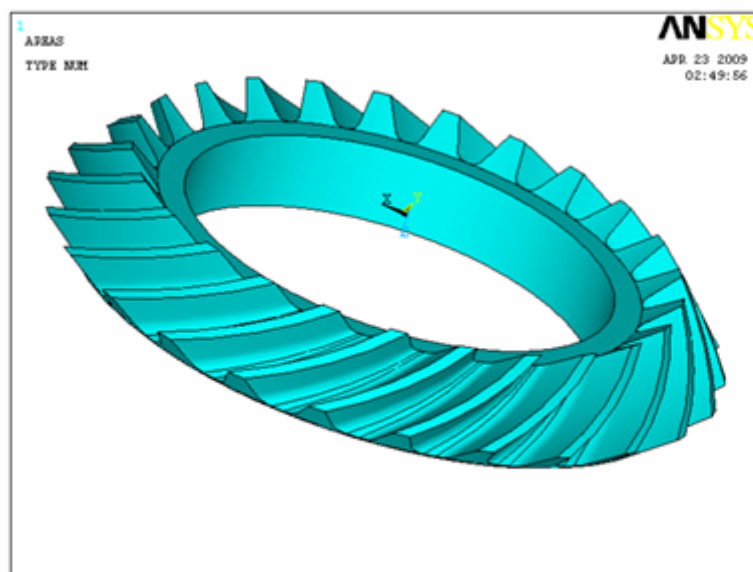


Fig. (5) cutting machine setup for cutting non-generated gear.



$$\alpha = 22 \text{ degree}$$

$$\beta = 30 \text{ degree}$$

$$\gamma = 60 \text{ degree}$$

$$r = 90 \text{ mm}$$

$$h_f = 4 \text{ mm}$$

$$N_2 = 25$$

Fig. (6) (a), A non-generated gear blank

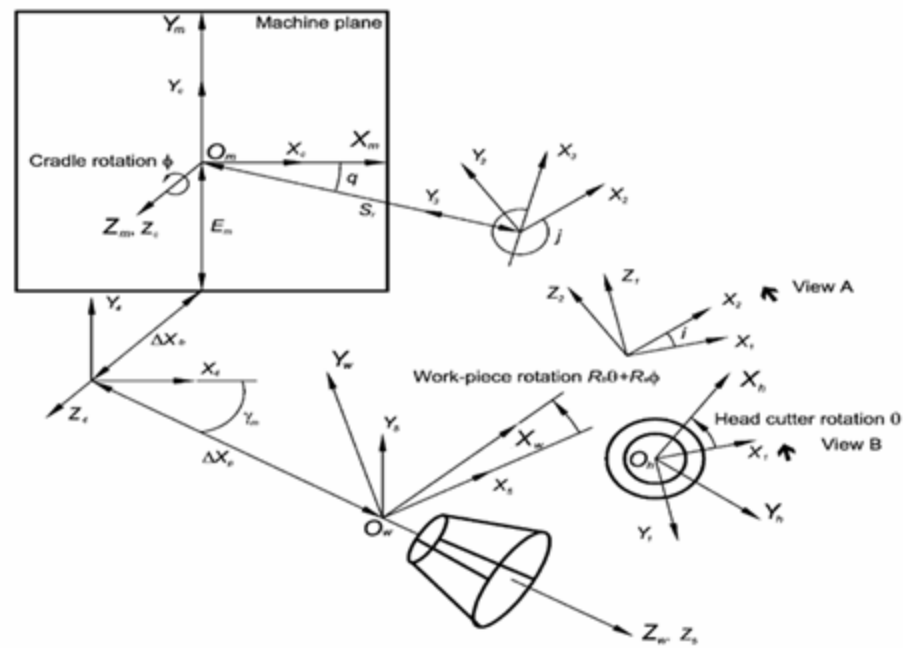
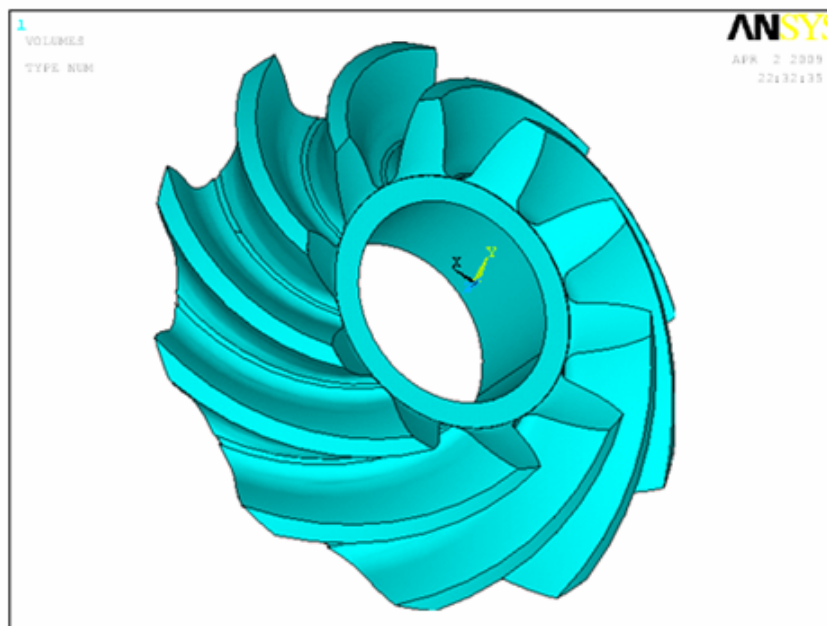


Fig. (7), Cutting machine setup for manufacturing a generated gear .



$$\alpha = 22 \text{ degree}$$

$$\beta = 37 \text{ degree}$$

$$\gamma = 50 \text{ degree}$$

$$r = 50 \text{ mm}$$

$$h_f = 4 \text{ mm}$$

$$N_1 = 10$$

Fig. (8), Hypoid pinion blank

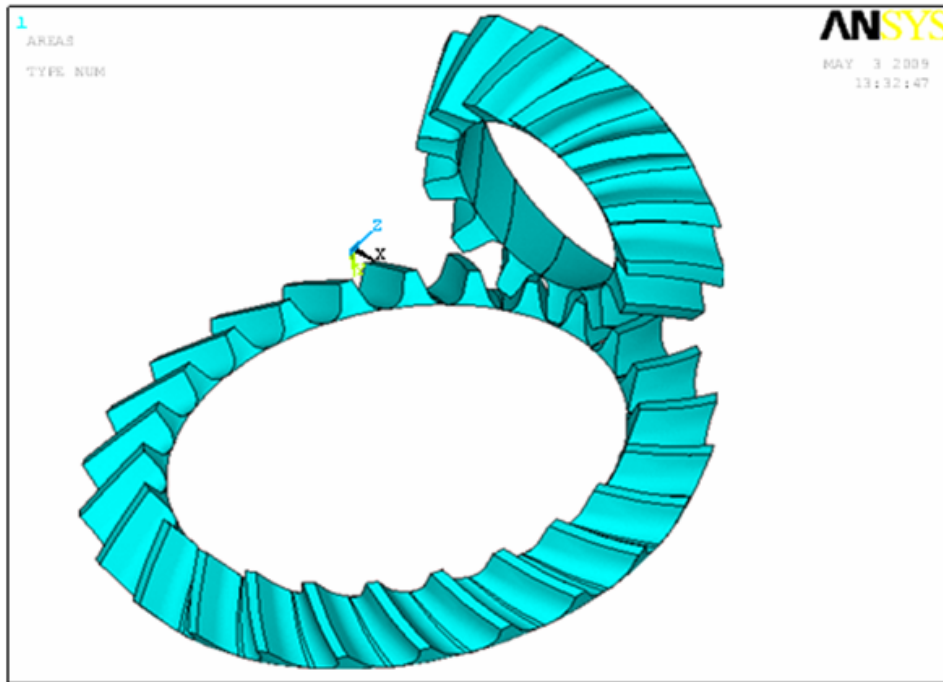


Fig. (9), Hypoid gear drive

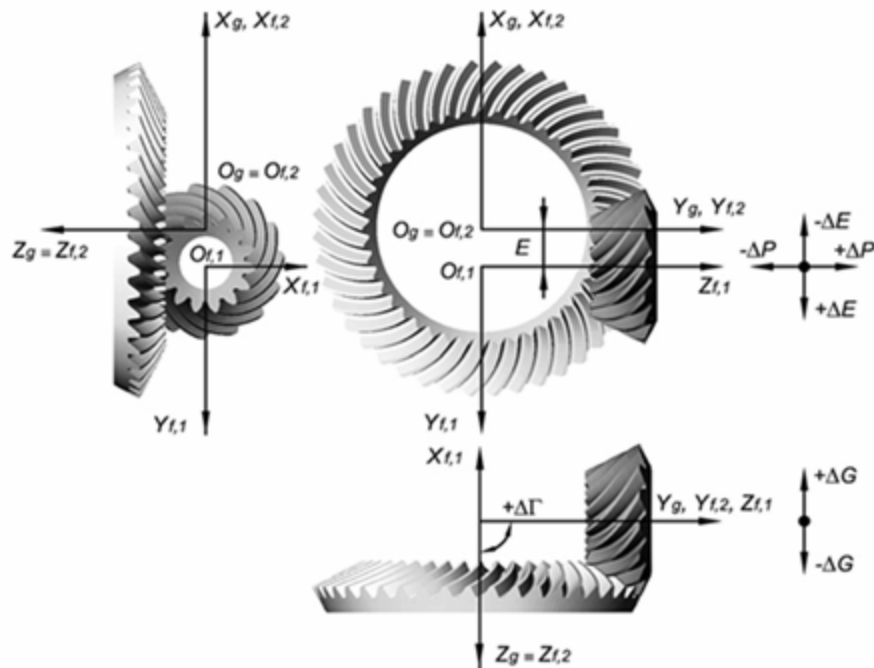
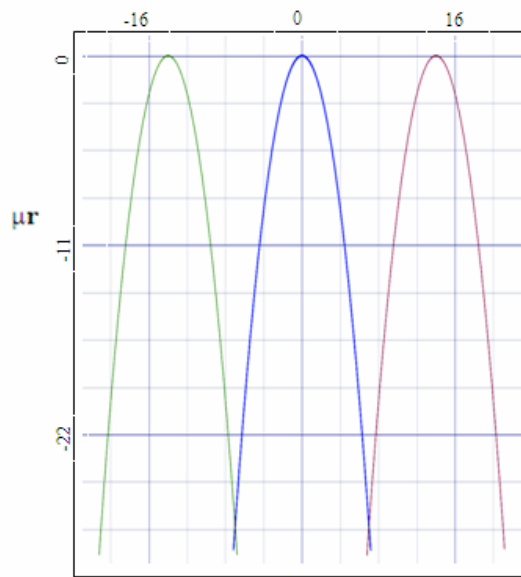
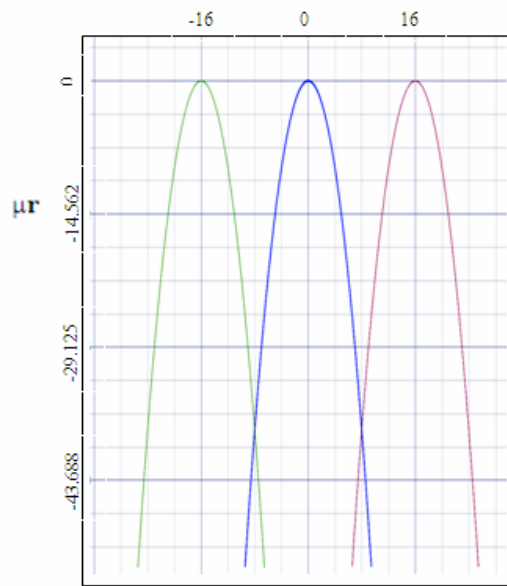


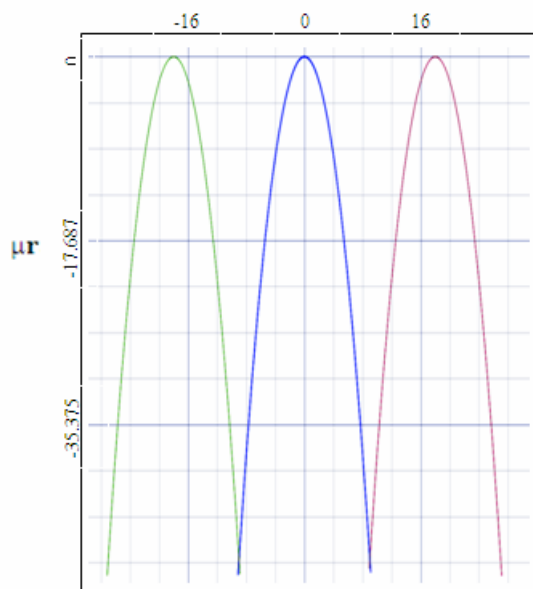
Fig. (10), Hypoid gear misalignment.



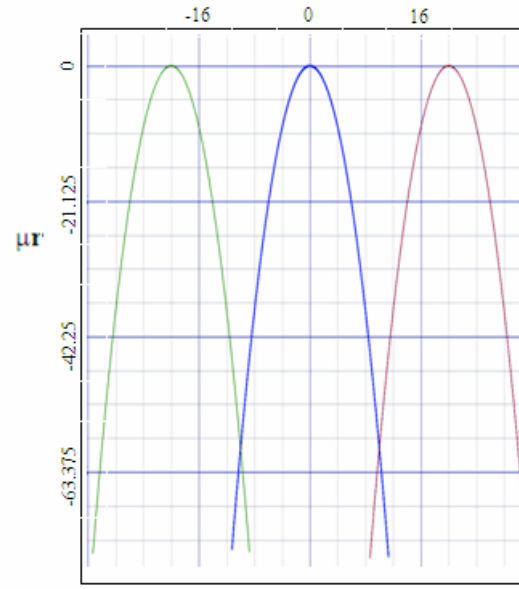
Pinion rotation angle (deg.)

Fig. (11), Concave side transmission function, $N_1=25$ 

Pinion rotation angle (deg.)

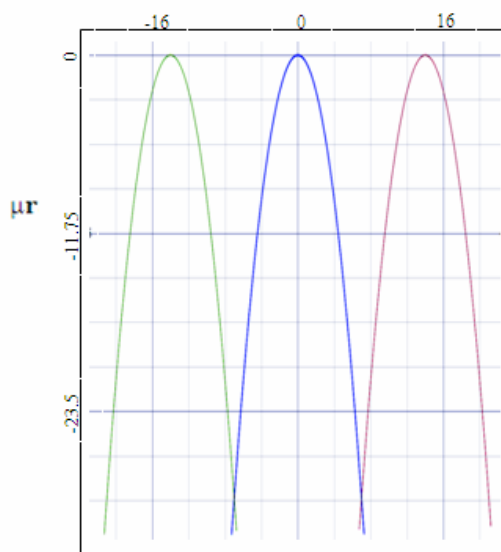
Fig. (12), Concave side transmission function, $N_1=22$ 

Pinion rotation angle (deg.)

Fig. (13), Concave side transmission function, $N_1=20$ 

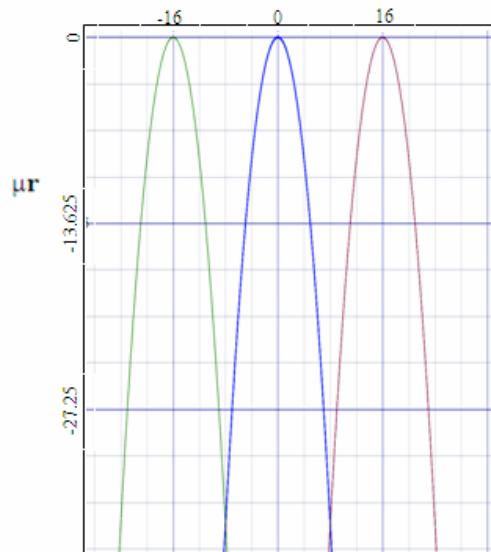
Pinion rotation angle (deg.)

Fig. (14), Concave side transmission function, $N_1=18$



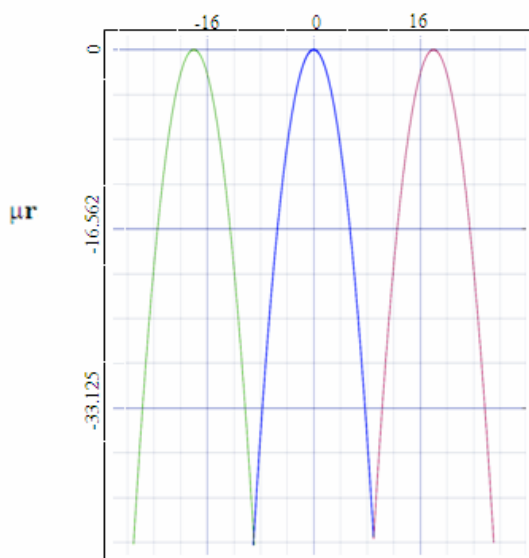
Pinion rotation angle (deg.)

Fig. (15), Convex side transmission function, $N_1=25$



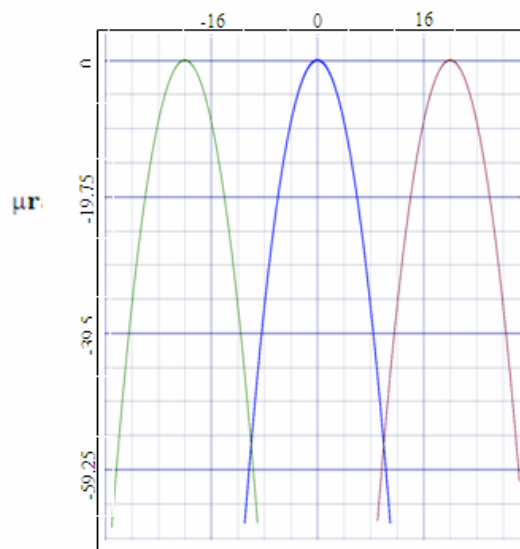
Pinion rotation angle (deg.)

Fig. (16), Convex side transmission function, $N_1=22$



Pinion rotation angle (deg.)

Fig. (17), Convex side transmission function, $N_1=20$



Pinion rotation angle (deg.)

Fig. (18), Convex side transmission function, $N_1=18$

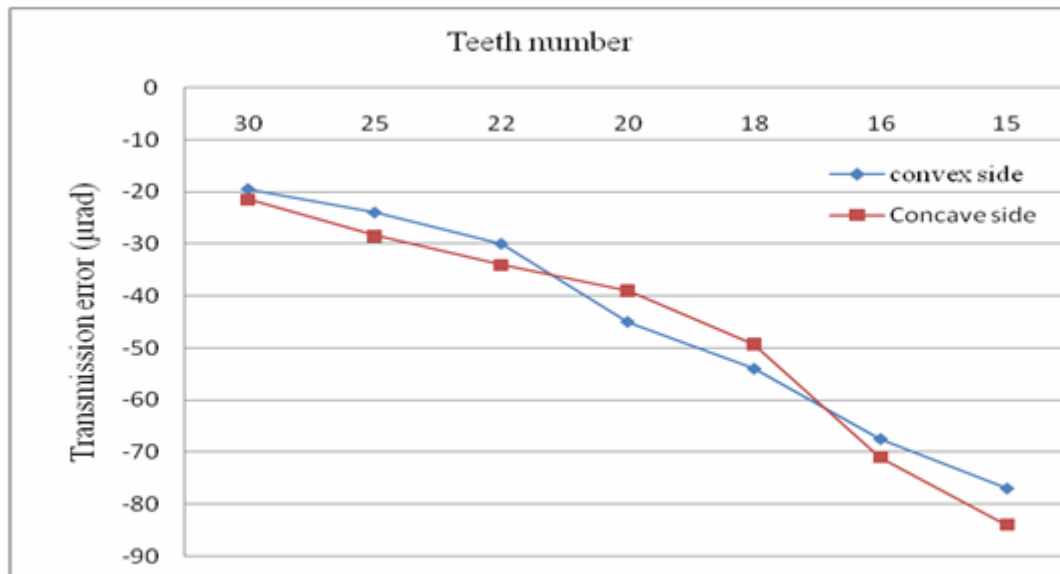


Fig. (19), Variation of transmission error with teeth number.



SIMULATION OF OPTIMAL SPEED CONTROL FOR A DC MOTOR USING LINEAR QUADRATIC REGULATOR (LQR)

Ruba M.K. Al-Mulla Hummadi
Mechanical Engineering Department
Baghdad University

ABSTRACT:

This paper describes DC motor speed control based on optimal Linear Quadratic Regulator (LQR) technique. Controller's objective is to maintain the speed of rotation of the motor shaft with a particular step response.

The controller is modeled in MATLAB environment, the simulation results show that the proposed controller gives better performance and less settling time when compared with the traditional PID controller.

:

LQR

MATLAB

PID

Keywords: DC motor, Optimal Speed control, PID controllers, LQR

INTRODUCTION:

Due to the excellent speed control characteristics of a DC motor, it has been widely used in industry (such as cars, trucks and aircraft) even though its maintenance costs are higher than the induction motor. As a result, authors have paid attention to position control of DC motor and prepared several methods to control speed of such motors. Proportional–Integral–Derivative (PID) controllers have been widely used for speed and position control. [Neenu, 2009]

They designed a position controller of a DC motor by selection of PID parameters using genetic algorithm (GA) once and secondly by using Ziegler and Nichols method of tuning the parameters of PID controller. They found that the first method gives better results than the second one.

[Delavari Hadi, 2006], presented and compared two types of controllers which are PID controller and optimal controller. The PID compensator is designed using (GA), while the other compensator is made optimal and integral state feedback controller with Kalman filter. Computer simulations have been carried out. Finally they found that the second controller gives less settling, less overshoot and better performance encountering with noise and disturbance parameters variations.

Other authors like [Boumediene, 2009], used a particle swarm optimization (PSO) instead of (GA). They presented a PID controller based on (PSO) method of tuning controller parameters. They modeled their PID-PSO controller in MATLAB environment and compare the results with fuzzy logic controller (FLC) using PSO. They found that PID-PSO controller gives better performance and minimal rise time than FLC-PSO controller.

[Sharaf, 2007], presented a novel PID dual loop controller for a solar photovoltaic (PV) powered industrial permanent magnet DC (PMDC) motor drive. MATLAB/SIMULINK was used in the analysis for the GUI environment.

[Molavi and khaburi, 2008], introduced the optimal strategies for speed control of permanent magnet synchronous motor (PMSM) through the linear quadratic regulator (LQR) and linear quadratic Gaussian (LQG) methodologies.

The simulation results showed that the proposed controllers have better performance for the sake of

design criteria like overshoot and settling time of the step response.

[Gwo, 2004], presented a novel optimal PID controller using (LQR) methodology in tuning the parameters of PID controller. The new PID controller is applied to control the speed of brushless DC motor (BLDC). Finally, the computer simulation and experimental results showed that the proposed controller gives better performance than the traditional controller.

This paper presents LQR controller which applied to control the speed of a DC motor. The rest of the paper is presented as follows: at first the plant model is described. The next section describes the PID technique and the design of LQR. Then simulation results are presented. Finally, the last section contains paper conclusion.

PLANT MODEL:

The speed of a DC motor is proportional to the voltage applied to it. While, its torque is proportional to the motor current. Speed control can be achieved by variable battery tapplings, variable supply voltage, resistors or electronic controls.

A simple motor model is shown in Fig.1. The armature circuit consist of a resistance (R_a) connected in series with an inductance (L_a), and a voltage source (e_b) representing the back emf (back electromotive force) induced in the armature when during rotation. [Ogata, 1998 and 2002].

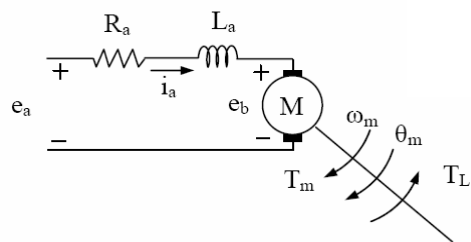


Fig.1 DC-Motor Model

The motor torque T_m is related to the armature current, i_a , by a torque constant K_i ;

$$T_m = K_i i_a \quad (1)$$

The back emf, e_b , is relative to angular velocity by;



$$e_b = k_b \omega_m = k_b \frac{d\theta}{dt} \quad (2)$$

From Fig. 1 we can write the following equations based on the Newton's law combined with the Kirchoff's law:

$$L_a \frac{di_a}{dt} + R_a i_a = e_a - K_b \frac{d\theta}{dt} \quad (3)$$

$$J_m \frac{d^2\theta}{dt^2} + B_m \frac{d\theta}{dt} = K_i i_a \quad (4)$$

There are several different ways to describe a system of linear differential equations. The plant model will be introduced in the form of **state-space representation** and given by the equations:

$$\begin{aligned} \dot{x} &= Ax + Bu \\ y &= Cx + Du \end{aligned} \quad (5)$$

According to eq.s from (2) to (4), the state space model will be:

$$\begin{bmatrix} \dot{i}_a \\ \dot{\omega}_m \\ \dot{\theta}_m \end{bmatrix} = \begin{bmatrix} -R_a/L_a & -K_b/L_a & 0 \\ K_i/J_m & -B_m/J_m & 0 \\ 0 & 1 & 0 \end{bmatrix} \begin{bmatrix} i_a \\ \omega_m \\ \theta_m \end{bmatrix} + \begin{bmatrix} 1/L_a \\ 0 \\ 0 \end{bmatrix} e_a \quad (6)$$

$$\omega_m = \begin{bmatrix} 0 & 1 & 0 \end{bmatrix} \begin{bmatrix} i_a \\ \omega_m \\ \theta_m \end{bmatrix} \quad (7)$$

with the block diagram as shown in Fig. 2

The DC motor data taken for this work are [Nguyen, 2006]:

Symbol	Value and unit
E	= 12volt
J _m	= 0.01kgm ²
B _m	= 0.00003kgm ² /s
K _i	= 0.023Nm/A
K _b	= 0.023V/rad/s
R _a	= 1Ω
L _a	= 0.5H

DESIGN OF THE LQR CONTROLLER [Firas, 2006]

LQR control that designed is classified as optimal control systems. This is an important function of control engineering. Fig.3 shows the designed LQR state-feedback configuration.

The purpose of the design is to realize a system with practical components that will provide the desired operating performance. The desired performance can be readily stated in terms of time domain performance indices. For example, the maximum overshoot and rise time for a step input are valuable time domain indices. In the case of steady state and transient performance, the performance indices are normally specified in the time domain.

The performance of a control system can be represented by integral performance measures. Therefore, the design of the system must be based on minimizing a performance index, such as the integral of the squared error (ISE).

The specific form of the performance index can be given as in eq.(8), where x^T indicates the transpose of the x matrix, then, in terms of the state vector, is

$$J = \int_0^{t_f} (x^T x) dt \quad (8)$$

Where x equals the state vector, and t_f equals the final time.

Then the design steps are as follows:

- 1- Determine the matrix P that satisfies eq.(8-a), where H is known.

$$\boxed{H^T P + PH = -I} \quad (8-a)$$

- 2- Minimize J by determining the minimum of eq.(8-b) by adjusting one or more unspecified system parameters (Firas, 2006)

$$\boxed{J = \int_0^{\infty} x^T x dt = x^T(0)Px(0)} \quad (8-b)$$

Upon examining the performance index (eq.8), recognizing that the reason the magnitude of the

control signal is not accounted for in the original calculation is that u (equals the control vector) is not included within the expression for the performance index. However, in many cases, the expenditure of the control signal energy are concerned. For example, in an electric vehicle control system, $(u)^2$ represents the expenditure of battery energy and must be restricted to conserve the energy for long periods of travel. To account for the expenditure of the energy of the control signal, it will be utilize the performance index

$$J = \int_0^{\infty} (x^T I x + \lambda u^T u) dt \quad (9)$$

Where λ is the scalar weighting factor and I = identity matrix. The weighting factor λ will be chosen so that the relative importance of the state variable performance is contrasted with the importance of the expenditure of the system energy resource that is represented by $u^T u$ as in the previous paragraphs, the state variable feedback will be represented by the matrix equation

$$u = -Kx \quad (10)$$

And the system with this state variable feedback as

$$\dot{x} = Ax + Bu = Hx \quad (11)$$

Now, substituting eq.(10) into eq.(9), then

$$\begin{aligned} J &= \int_0^{\infty} (x^T I x + \lambda (Kx)^T (Kx) dt \\ &= \int_0^{\infty} [x^T (I + \lambda K^T K) x] dt = \int_0^{\infty} x^T Q x dt \quad (12) \end{aligned}$$

Where $Q = (I + \lambda K^T K)$ is an $n \times n$ matrix. postulating the existence of an exact differential so that

$$\frac{d}{dt} (x^T P x) = -x^T Q x \quad (13)$$

Then, in this case, it is required that

$$H^T P + PH = -Q \quad (14)$$

As before in eq.(8-a)

$$J = x^T(0)Px(0) \quad (15)$$

Now, the design steps are exactly as for eq.(8-a) and eq.(8-b) with exception that the left side of eq.(14) equals $-Q$ instead of $-I$. Of course, if $\lambda = 0$, eq.(14) reduces to eq.(8-b).

Consider the single-input, single-output (SISO) system with

$$\dot{x} = Ax + Bu \quad (11)$$

and feedback

$$u = -Kx = -[k_1 \ k_2 \dots k_n]x$$

The performance index is

$$J = \int_0^{\infty} (x^T Q x + R u^2) dt$$

or the performance index is

$$J = \int_0^{\infty} [(tracking \ errors)^2 + (weighted \ inputs)^2] dt$$

where R is the scalar weighting factor. This index is minimized when

$$K = R^{-1} B^T P$$

The $n \times n$ matrix p is determined from the solution of equation

$$A^T P + PA - PBR^{-1}B^T P + Q = 0 \quad (16)$$

The two matrices Q and R are selected by design engineer by *trial and error*. Generally speaking, selecting Q large means that, to keep J small. On the other hand selecting R large means that the control input u must be smaller to keep J small. One should select Q to be *positive semi-definite* and R to be *positive definite*. This means that the scalar quantity $x^T Q x$ is always positive or zero at each time t . And the scalar quantity $R u^2$ is always positive at each time t .

eq.(16) can be easily programmed for a computer, or solved using MATLAB. eq.(16) is often called



the **Riccati Equation**. This optimal control called the **Linear Quadratic Regulator (LQR)** which is shown in state-space configuration in Fig. 3. Combine Fig.2 with Fig.3 yields Fig.4, which shows the use of LQR controller with the DC motor.

SIMULATION MATLAB SCRIPT FILE AND RESULTS:

The simulation procedure may be summarized as follows:

- First input the DC motor data,
- Write the differential equations for the model then get the state space representation as in eq. (6)
- Get the open loop transfer function and the closed loop step response
- Finally performing the performance of PID controller and LQR controller and compare the results.
- The output will be taken as $\omega_m(s)$ from Fig.4.

MATLAB script file is:

```
% file name: DCM2.m
clear
clc
t = 0:0.001:10;
% DATA1=====
J = 0.01;
b = 0.00003;
K = 0.023;
R = 1;
L = 0.5;
A = [-b/J    K/J
     -K/L    -R/L];

B = [0
     1/L];
C = [1    0];
D = 0;
% sys = ss(A,B,C,D);
num=K;
den=[(J*L) ((J*R)+(L*b)) ((b*R)+K^2)];
open=tf(num,den);
closed= feedback(open,1)
%=====PID=====
Kp = 150; %
Ki = 150; % took by try
Kd = 0.4; %
PID = tf([Kd Kp Ki],[1 0]);
PIDsys = feedback(PID*open,1);
% ++++++
```

```
% Linear Quadratic Regulator design
LQR
% ++++++
Q=[.2 0;0 0.028];
R=[.2];
[KK,S,e] =lqr(A,B,Q,R)
ZZ=(A-B*KK);
LQR=ss(ZZ,B,C,D);
damp(LQR)
[num1,den1]=ss2tf(ZZ,B,C,D,1);
G=tf(num1,den1) %ALWAYS den=1
BECAUSE ONLY u
% ++++++
% Linear Quadratic Regulator design
LQR Step
% ++++++
figure(1)
step(closed,t),title('Closed Loop step
response')
xlabel('Time','FontSize',11);
ylabel('P.U. speed','FontSize',11);
figure(2)
step(PIDsys,t),title('PID step
response')
xlabel('Time','FontSize',11);
ylabel('P.U. speed','FontSize',11);
figure(3)
step(LQR,t),title('LQR step response')
xlabel('Time','FontSize',11);
ylabel('P.U. speed','FontSize',11);
figure(4)
step(PIDsys,LQR,closed,t),title('step
all')
xlabel('Time','FontSize',11);
ylabel('P.U. speed','FontSize',11);
```

Finding the poles and zeros for a transfer function in MATLAB :

To find the zeros use the command: $z=\text{zero}(g)$

To find the poles use the command: $p=\text{pole}(g)$

where g : is the transfer function.

After executing the previous script file the open loop transfer function of the DC motor according to the selected data is:

$$\omega_m(s) = \frac{0.023}{0.005s^2 + 0.01002s + 0.000559}$$

The two poles for the open loop transfer function are: $(-0.0575+j0)$ and $(-1.95+j0)$.

The closed loop for speed of the DC motor with unity feedback transfer function is:

$$\frac{\omega_m(s)}{e_a(s)} = \frac{0.023}{0.005s^2 + 0.01002s + 0.02356}$$

with two poles: $(-1+j1.92)$ and $(-1-j1.92)$.

The closed loop step response for speed is shown in Fig.5, with settling time of 3.83sec. and peak amplitude of 1.17.

Now by using PID controller for a DC motor we get better settling time (2.76 sec) and the peak amplitude (1.84) than closed loop response as shown in Fig.6

Using LQR controller for a DC motor gives better settling time (1.99 sec) and peak amplitude (1) than PID controller response as shown in Fig.7 The LQR transfer function is:

$$\frac{\omega_m(s)}{e_a(s)} = \frac{4.6}{s^2 + 3.681s + 4.601}$$

The closed loop, PID and LQR step responses are plotted on the same figure as shown in Fig.8.

CONCLUSION

Speed control of a DC motor is an important issue, so this paper presents a design method to determine the optimal speed control using LQR method. The obtained results showed that the presented controller has shorter settling time and smaller overshoot than that of the traditional PID controller as shown in Table 1.

Table (1) Simulation Results

	Settling Time	Peak Amplitude	Over shoot
Closed Loop With Unity Feedback	3.83 sec	1.17	19.5%
PID Controller	2.76 sec	1.84	84.8%
LQR Controller	1.99 sec	1	0.525%

REFERENCES

Boumediene Allaoua, Barhim Gasbaoui and Barhim Mebarki, "Setting Up PID DC Motor Speed Control Alteration Parameters Using Particle Swarm Optimization Strategy", Leonardo Electronic Journal of Practices and Technologies, ISSN 1583-1078, Issue 14, January-June 2009, pp. 19-32

Firas Mohammed To'aima, "Optimal Control of Governor and Exciter for Turbogenerator using LQG", Baghdad University, College of Engineering, PhD Thesis, November 2006

Gwo-Ruey Yu and Rey-Chue Hwang, "Optimal PID speed control of brushless DC motors using LQR approach", Systems, Man and Cybernetics, 2004 IEEE International Conference on Vol 1, Issue , 10-13 Oct. 2004, pp: 473 – 478.

Hadi Delavari, Ghasem Alizadeh and Mohammad Bagher Bannane Sharifian, "Optimal Integral State Feedback Controller for a DC Motor", 2006, paper identification number 440.

Katsuhiko Ogata: System Dynamics; Prentice Hall International, Inc. Third Edition 1998.

Katsuhiko Ogata: Modern Control Engineering; Prentice Hall International, Inc. Fourth Edition 2002.

Neenu Thomas and Dr. P.Poongodi, "Position Control of DC Motor Using Genetic Algorithm Based PID Controller", Proceedings of the World Congress on Engineering 2009 Vol. II, WCE2009, July 1-3, 2009, London, U.K.

Roosbeh Molavi, and Davood A. Khaburi, "Optimal Control Strategies for Speed Control of Permanent-Magnet Synchronous Motor Drives", World Academy of Science, Engineering and Technology 44, 2008, pp.428-432.

Sharaf, A.M., Elbakush, E., Altas, I.H., "Novel Control Strategies for Photovoltaic Powered PMDC Motor Drives", IEEE, 2007

Tutorial 12 about DC motor, instrumentation and process control by Hung Nguyen, 2006

**LIST OF SYMBOLS:**

$A = n \times n$ constant matrix

$B = n \times 1$ constant matrix

$B_m =$ viscous friction coefficient (kgm^2/s)

$C = 1 \times n$ constant matrix

$D =$ constant

$e_a(t) =$ applied voltage (V)

$e_b(t) =$ back emf (V)

$i_a(t) =$ armature current (A)

$J_m =$ moment of inertia of rotor (kg.m^2)

$K_b =$ back emf constant (V/rad/s) ($K_b = K_i$)

$K_i =$ torque constant (Nm/A)

$L_a =$ armature inductance (H)

$R_a =$ armature resistance (Ω)

$t_f =$ final time(sec)

$T_L(t) =$ load torque (Nm)

$T_m(t) =$ motor torque (Nm)

$u =$ control signal

$x =$ state vector

$y =$ output signal

$\theta_m(t) =$ rotor displacement (rad)

$\omega_m(t) =$ rotor angular velocity (rad/s)

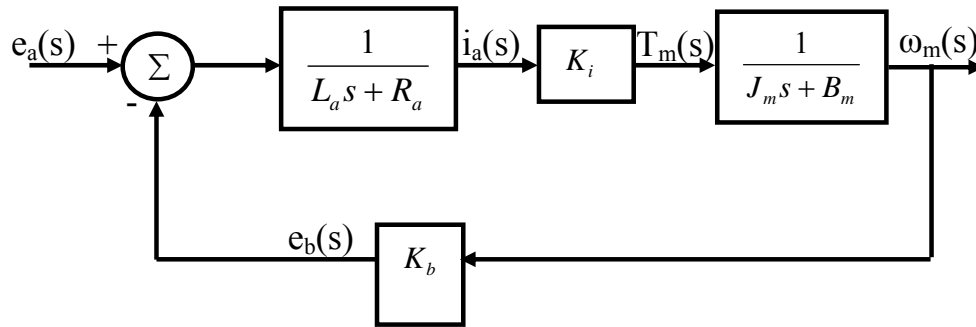


Fig. 2- DC-Motor System Block Diagram for speed (Plant System)

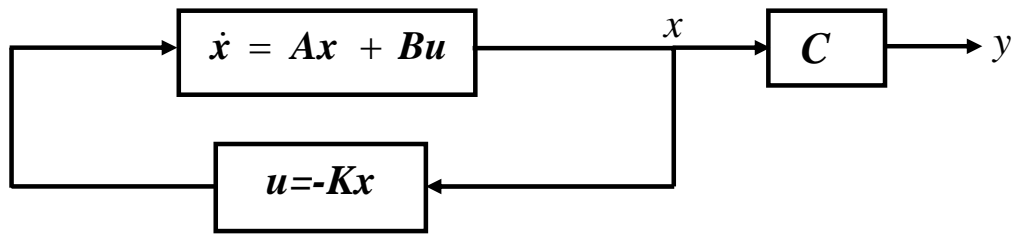


Fig. 3 Linear Quadratic Regulator Structure

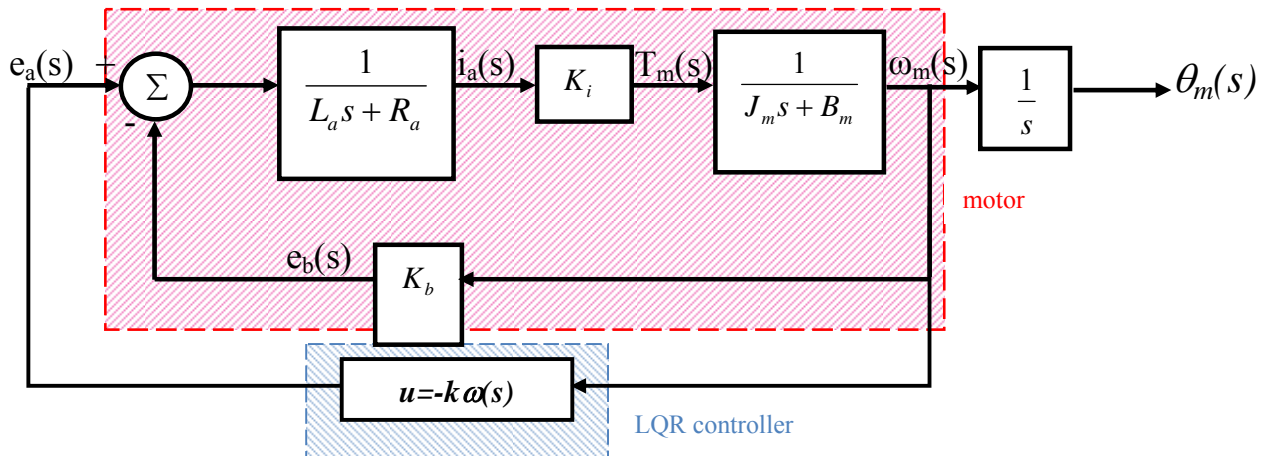
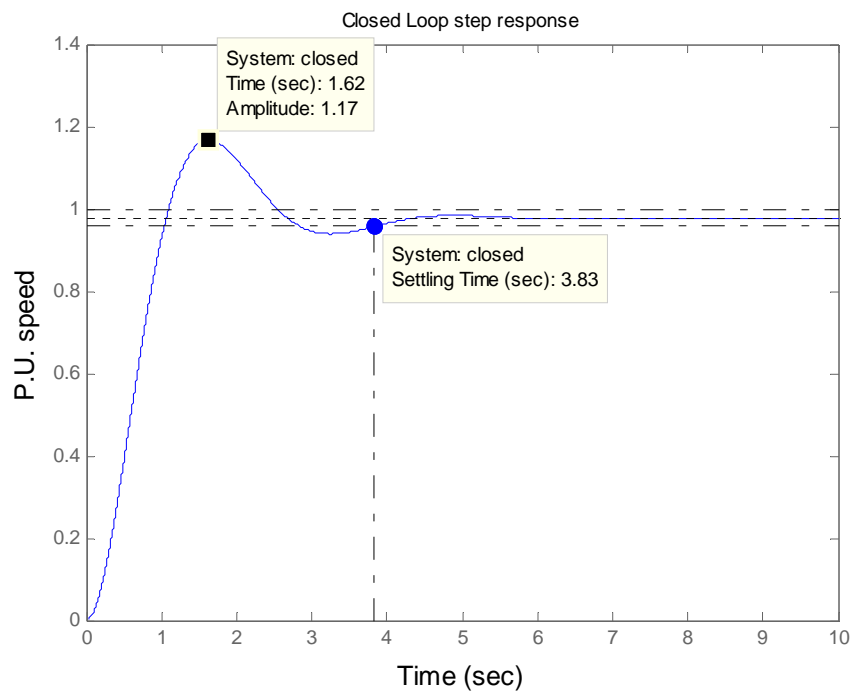
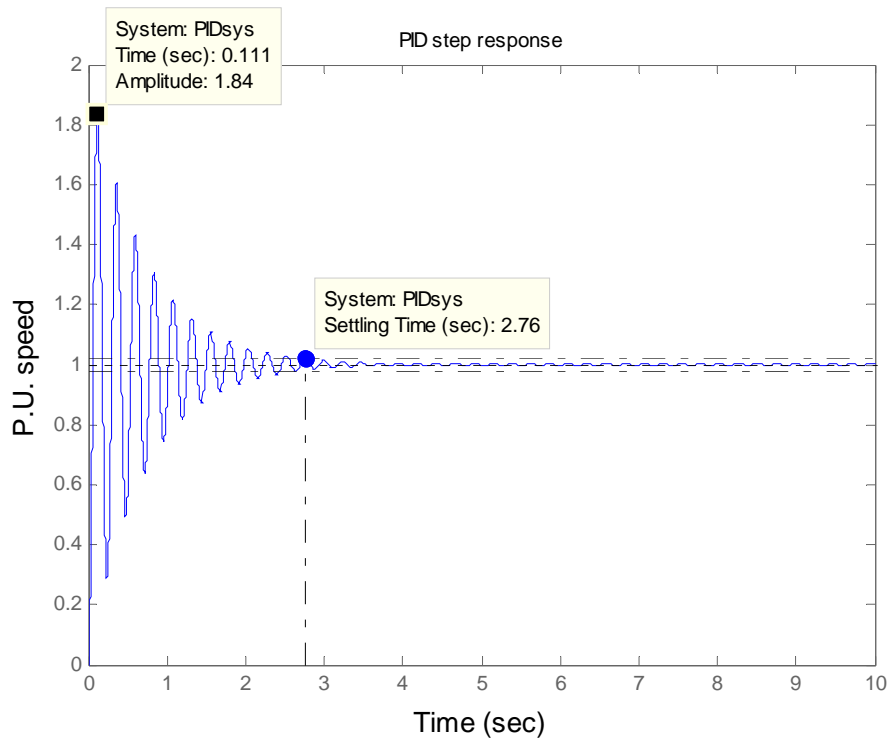
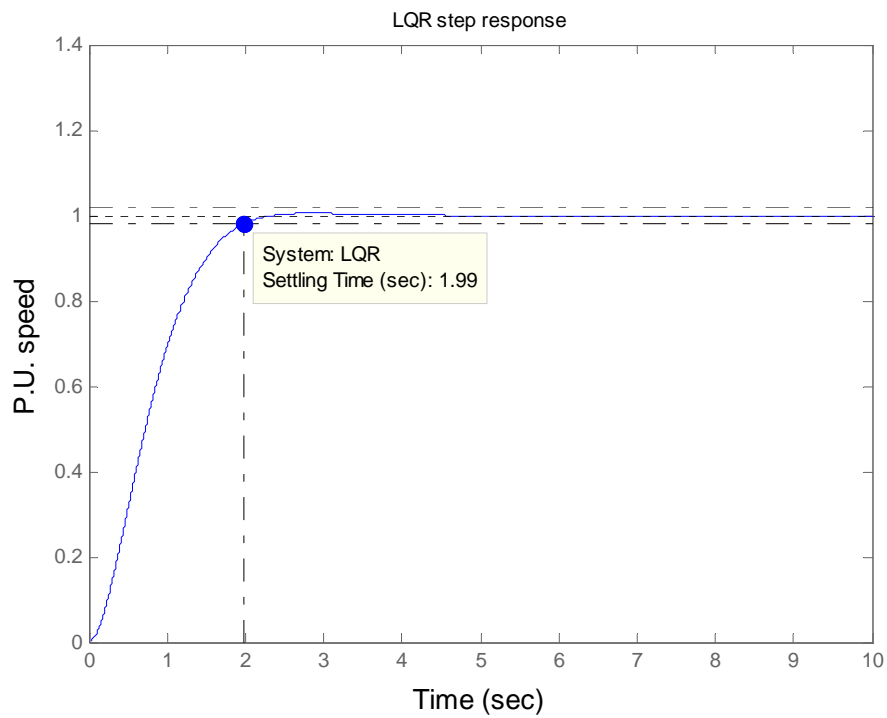
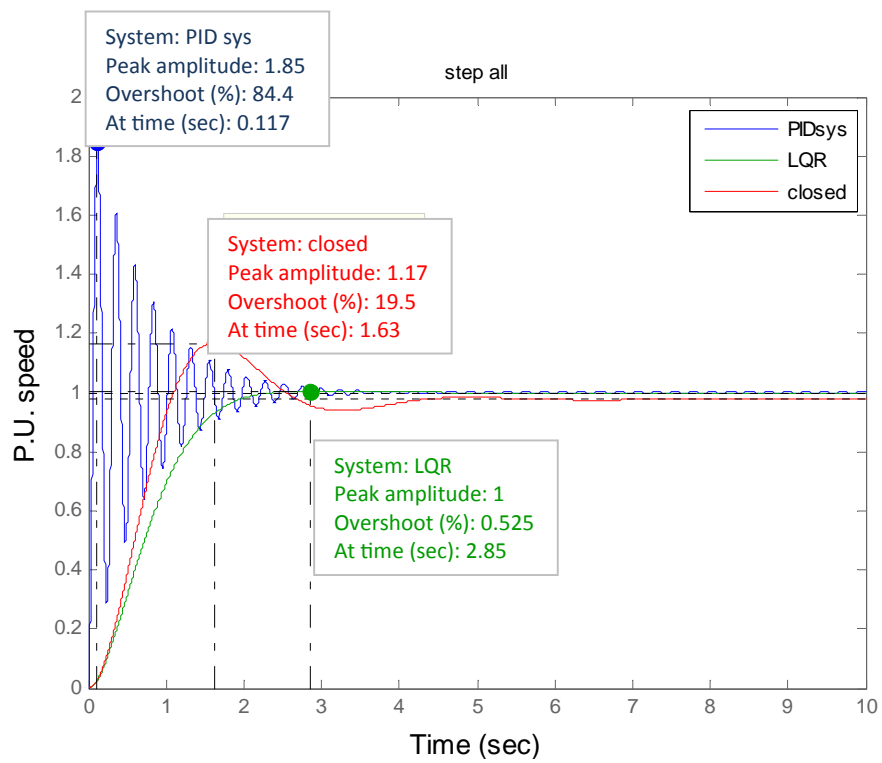


Fig. 4- DC-Motor System with LQR

**Fig. 5 Closed Loop Step Response****Fig.6 PID Step Response**

**Fig.7 LQR Step Response****Fig.8 Closed loop, PID and LQR Step response**



EFFECT OF HOOPS AND COLUMN AXIAL LOAD ON SHEAR STRENGTH OF HIGH-STRENGTH FIBER REINFORCED BEAM-COLUMN JOINTS

Jamal A. Farhan

Lecturer, Civil Engineering Dept. College of
Engineering, University of Anbar

Zaid M. Kani

Lecturer, Dams Engineering Dept. College of
Engineering, University of Anbar

Abstract

A reinforced concrete frame is referred as "RIGID FRAMES". However, researches indicate that the Beam-Column joint (BCJ) is definitely not rigid. In addition, extensive research shows that failure may occur at the joint instead of in the beam or the column. Joint failure is known to be a catastrophic type which is difficult to repair.

This study was carried out to investigate the effect of hoops and column axial load on the shear strength of high-strength fiber reinforced Beam-Column Joints by using a numerical model based on finite element method using computer program ANSYS (Version 11.0). The variables are: diameter of hoops and magnitude of column axial load.

The theoretical results obtained from ANSYS program are in a good agreement with previous experimental results.

(ANSYS)

(ANSYS)

Keywords: Hoops, Column Axial Load, High Strength Concrete (HSC), Fiber Reinforced Concrete, Finite Elements, Beam-Column Joints (BCJ), ANSYS

1. INTRODUCTION

In building analysis and design, in general, the structures that contain slabs, beams and columns are referred as "Rigid Frames". However, researches indicate that, both reinforced concrete and structural steel frames, the beam-column joints are definitely not rigid; they are subjected to deformation under all types and stages of loadings. Moreover, extensive researches show that failure may occur at the joint instead of in the column or the beam. Thus, another way of looking at a joint is to be considered it as a member of the structure, as slabs, beams and columns etc [1].

In general, the adequate performance of beam-column joints depends primarily on providing the principal requirements for shear strength, confinement and anchorage of reinforcement passing through or terminating in the joint.

Some researchers studied the effect of using fiber reinforcement in the beam-column joints [2,3,4,5]. They show that the addition of fibers enhanced the ductility and strength of the beam-column joints.

With the production of High Strength Concrete, enhanced material properties such as higher compressive and tensile strength and elastic modulus.

This study was carried out to investigate the effect of hoops and column axial loads on the strength of high-strength fiber reinforced beam-column joints by using analytical model based on finite element method and using computer program ANSYS (version 11.0)[6]. The variables considered are: Diameter of hoops and magnitude of column axial load.

The comparison between the theoretical results obtained from the suggested model and the experimental results from previous research [1] shows a good agreement.

2. TESTING PROGRAM

The specimens are classified into three groups. Group.1 specimens includes three specimens with out fiber reinforcement, the first is

without hoops while the others are reinforced with one hoop of (4 and 8mm) diameters. Group.2 includes three specimens having the same properties of group.1 except that they contain the optimum volume fraction of hooked fibers which equals 1% [1], all the two groups are tested under a constant column axial load equal to (100 kN). Group.3 includes two specimens contain 1% of fibers and without hoop reinforcement tested under (150 and 200 kN) column axial loads. **Table.1** shows the designation and properties of the specimens.

All the eight beam-column joints have identical beam and column sizes. **Fig.1** shows the details of the specimens, these dimensions were used previously by several investigators [7, 8, and 9]. The beams were 300mm depth by 150 mm width and the columns were 200 mm depth by 150 mm width.

All columns were reinforced with four 16 mm longitudinal bars and 8 mm closed ties at 85 mm centre to centre spacing. All beams were reinforced with three 18 mm bars on tension side and three 12 mm bars on compression side. This resulted in an under-reinforced beam with tension steel percentage slightly under 1.9%. Beam stirrups were 8 mm closed ones spaced at 130 mm centre to centre.

Ordinary Portland cement from Kubaysa factory was used. This cement conforms to Iraqi standards [10]. It has already been found that this cement was the most suitable for high strength concrete [11].

Fine aggregate passing through 4.75mm sieve conforming to ASTM C33 specifications [12] was used, the fineness modulus was 2.5 and the specific gravity was 2.6.

Natural coarse aggregate was used. Many references have shown that the smaller size aggregates produce higher strength values. Therefore maximum size was chosen to be 9.5 mm. Grading of these aggregates conforms to ASTM C33 specifications [12]. The bulk specific gravity of these aggregates was 2.7.

For high strength concrete production, water content of mix is reduced, and the associated reduction in workability is compensated for by using superplasticizer (Melment) which are chemical admixtures. The optimum dosage for this admixture was found to be 5% of weight of cement and the reduction of water for this dosage was 27.7%.

Three samples of reinforcing steel bars for each size of bars (8,12,16, and 18)mm were tested, the results of tests are shown in **Table.2**. Further tests on separate samples were made using the Instron testing machine. Results were automatically recorded by a plotter, which was attached to the testing machine. The purpose of these tests was to determine the stress strain relationship of the bars, which were used in the analytical model.

Cylindrical compressive strength (f'_c), modulus of rupture (f_r), poison's ratio (ν) and modulus of elasticity (E_c) for the concrete of the eight specimens are included in **Table.3**.

3. EXPERIMENTAL PROGRAM

The testing rig dimensions were (3x4)m with a depth of 1.1m. The testing rig consisted of a reinforced concrete mass with a special reinforcing bars used for fixing the large steel I-sections as reaction points for bracing the specimens and applying the loads. It was insured that the testing rig was stiff enough to resist all possible loadings [1].

The specimens were tested using two hand operating jacks; the first was used to apply the column axial load (N_u), while the second was used to apply the beam load (V). Ball and socket type hinges, designed and constructed especially for allowing rotation in the plane of the frame only, were used to brace the columns in the two sides and the bottom. However for the loading points under the two jacks, roller type hinges designed and constructed especially for allowing movement in the direction perpendicular to the applied load only, were used to eliminate fixity. All these details are illustrated in **Fig.2**.

4. ANALYTICAL MODELLING

Building the analytical model consists of:

4.1 Element Type

The beam-column joint was modelled in ANSYS 11.0 [6] with Solid 65, Solid 45 and Link 8 elements. Solid 65 element was used to model the concrete and Solid 45 was used to model steel plates at supports and under testing loads. These elements have eight nodes with three degrees of freedom at each node which is the translations in x, y and z directions. Link8 element was used to model reinforcement. This three dimensional bar element has two nodes with three degrees of freedom at each node which is translations in x, y and z directions.

4.2 Sectional Properties (Real Constants)

The real constants considered for Solid 65 were; volume ratio and angle of orientation of reinforcement. Since there was no smeared reinforcement, the real constants (volume ratio and orientation angles) were set to zero. No real constant sets exist for Solid 45 element. The real constant that considered for Link8 elements were sectional areas.

4.3 Material Properties

Parameters needed to define the material models are given in **Table.4**. As seen in this table, there are multiple parts of the material model for each element. Material model number 1 refers to Link8 element which is used to model reinforcing bars. Link8 requires linear and bilinear isotropic. **Fig.3** is used to define the bilinear stress-strain relationship which is important for the computer solution convergence[13]. For example the material properties of 12mm bar diameter are illustrated in **Table.2**, which are the modulus of elasticity, yield stress and ultimate strength.

Material model number 2 refers to solid65 element for specimen No.1 which was used to model concrete. Solid65 element requires linear isotropic and multi-linear isotropic material properties to properly model concrete. E_c is the modulus of elasticity of concrete (E_c), and PRXY is the Poisson ratio (ν). For the normal weight concrete based on a dry unit weight (2200-2500 kg/m³); E_c was taken as in (ACI 318) [14]:

$$E_c = 4700\sqrt{f'_c} \quad (1)$$

According to Bangash [15], the value of poisons ratio can be taken equal to (0.2). In this study the values of the modulus of elasticity and poisons ratio are determined from tests and used in **Table.4**. According to Desayi and Krishnan [16], the compressive uniaxial stress-strain relationship for concrete model is obtained using equations (2), (3), and (4).

$$f = \frac{E_c \varepsilon}{1 + \left(\frac{\varepsilon}{\varepsilon_o} \right)^2} \quad (2)$$

$$\varepsilon_o = \frac{2f'_c}{E_c} \quad (3)$$

$$E_c = \frac{f}{\varepsilon} \quad (4)$$

Where:

f = stress at any strain ε , N/mm². ε = strain at stress f . ε_o = strain at the ultimate compressive strength f'_c . E_c = Modulus of elasticity for concrete (equation 1)

The multi-linear isotropic stress-strain implemented requires the first point of the curve to be defined by the user. It must satisfy Hooks law defined by equation (4). The multi-linear curve is used to help with convergence of the nonlinear solution algorithm. In this study, the concrete stress-strain relationship was determined from tests and used in **Table.4**

Concrete material model in ANSYS [6] requires that different constants be defined. These 9 constants are:

1. Shear transfer coefficients for an open crack;
2. Shear transfer coefficients for a closed crack;
3. Uniaxial tensile cracking stress;
4. Uniaxial crushing stress (positive);
5. Biaxial crushing stress (positive)
6. Ambient hydrostatic stress state for use with constants 7 and 8;
7. Biaxial crushing stress (positive) under the ambient hydrostatic stress state (constant 6);
8. Uniaxial crushing stress (positive) under the ambient hydrostatic stress state (constant 6);
9. Stiffness multiplier for cracked tensile condition.

Typical shear transfer coefficients range from 0.0 to 1.0, with 0.0 representing a smooth crack (complete loss of shear transfer) and 1.0 representing a rough crack (no loss of shear transfer). The shear transfer coefficients for open and closed cracks were determined using the work of Kachlakev, et al. [17] as a basis. Convergence problems occur when the shear transfer coefficient for the open crack dropped below 0.2. The presence of steel fibers in concrete mixture affects the value of this factor significantly because it increases the shear strength of concrete, thus in this study different values for this factor were used for each specimen to simulate the effect of type and volume fraction of steel on the beam-column joint model.

The uniaxial cracking stress is based upon the modulus of rupture. This value can be determined using the equation ACI code [14]:

$$f_r = 0.62\sqrt{f'_c} \quad (5)$$

In this study the cracking stress was determined from tests and used in **Table.4**. The uniaxial crushing stress in this model is based on the uniaxial unconfined compressive strength (f'_c). In this study a value of (-1) is given to the crushing coefficient to turn off the crushing capability of the concrete element and prevent local failure. The other five coefficients were given the value 0.0.

Material model number 3 refers to solid45 element which is used to model steel plates at supports and under testing loads. It requires linear isotropic properties only.

4.4 Modeling of Joint

The beam-column joint was modeled by two solid models. The block model was used to model concrete and steel plates while lines were used to model reinforcement. After the solid model was constructed, it will be meshed to form the finite element model. **Fig. 4, 5 and 6** shows the solid model of the beam-column joint, reinforcement and the finite element model after meshing respectively.

The loads were applied on the columns and beams through the steel plates, the axial load applied on the center of the column, while the transverse (shear) force was applied at (0.2m) from the beam end. For nonlinear solution, the shear force was divided in to small parts (time stepping).

5. RESULTS AND DISCUSSION

5.1 Failure Load

All specimens failed in the joint as a shear failure, **Fig.7**. **Table.5** shows the analytical and experimental failure load and the ratio of analytical to experimental result.

5.2 Effect of Hoops on the Joint Strength

Fig.8 illustrates the effect of including hoops of different diameters, (0, 4mm and 8mm), but with a single mid-depth layer in the joint, on ultimate load capacity of the joint for the experimental and analytical results. In this work it was found from experimental results that the addition of a single mid-depth 8mm hoop for the beam-column joint with out fiber reinforcement increase the joint load capacity. The addition of this hoop bar increased the load capacity for SP-3 (reinforced with 8mm deformed hoop bar) upon

SP-1 (unreinforced) by 44.9%. It seems from this work that a preferred solution for joint strengthening might be with a combination of two factors (1% volume fraction of hooked fibers plus single mid-depth 8mm hoop bar, e.g. SP-6). As can be seen from the test results, that latter led to 114% strengthening of the beam column joint upon SP-1.

Previous research [9,21] supports the recommendation in this work and indicates beyond doubt that more layers of hoops in the joint leads to less stress development in them. Therefore it is expected, if adequate bond and confinement conditions are provided, that for higher hoop contribution increasing the size of a central hoop is more advantageous than increasing the number of layers.

Fig. 8 also shows that the analytical model represents accurately the effect of diameter of hoops on joint strength for both plain and fiber reinforced concrete beam-column joints, and it was in good agreement with the experimental results.

5.3 Effect of Column Axial Load

One of the primary conditions in the design of beam-column joints is maintaining the required axial load capacity [22]. Tests [8, 23] showed that the presence of axial compression load results in an increase in the shear strength of a beam-column joint. Therefore in a given joint and beam moment capacity an increase in axial compression in the column resulted in less joint shear reinforcement requirements [24]. **Fig.9** shows the effect of axial load on the joint strength. The increase of the column axial load from 100kN to 200kN will increase the joint strength by 21%.

Fig. 9 also shows that the analytical model succeeded in representing the effect of column axial load on the strength of the joint only with the (150 kN) load while it gave an obvious overestimation and underestimation for the (100 kN) and (200 kN) load, respectively.

6. CONCLUSIONS

Based on the results obtained in this study, the following can be concluded:

- 1- The results predicted by the analytical model were in good agreement with the experimental results. The maximum difference in predicting the failure load is 9%. This indicates that the analytical model to predict the effect of hoops

and column axial load on the beam-column joint strength can be used instead of experimental model which may be expensive and leads to time consumption.

- 2- Transverse reinforcement (hoops) in the joint improves the strength. If one 8mm hoop bar is added for the joint without fiber reinforcement the increase in strength is 44.9% while if it is added to a joint reinforced by fibers (with 1% volume fraction), the increase is 114%.
- 3- Increasing the column axial load leads to an increase in the joint strength, for example the increase of this load from 100kN to 200 kN increases the strength by 21%

7. REFERENCES

- 1- Kani, Z.M., "**Capacity of High Strength Fiber Reinforced Beam-Column Joints**", M.Sc thesis, University of Technology, Baghdad, Iraq, 1997
- 2- Gefken, P.R and Ramey, M.R., "**Increased Joint Hoop Spacing in Type 2 Seismic Joints Using Fiber Reinforced Concrete**", ACI Structural Journal, Vol. 86, No.2, March-April, 1989, pp. 168-172.
- 3- Jindal, R.L. and Hassan, K.A., "**Behaviour of Steel Fibers Reinforced Concrete Beam-Column Connections**", Fibre Reinforced Concrete, ACI Publication, SP-81, 1984, pp. 107-123.
- 4- Craig, R. J., Mahadev, S., Patel, C. C., Viteri, M. and Kertesz, C., "**Behaviour of Joints Using Reinforced Fibrous Concrete**", Fibre Reinforced Concrete, ACI Publication, SP-81, 1984, pp. 125-167
- 5- Henager, C. H., "**Steel Fibrous, Ductile Concrete Joint for Seismic-Resistant Structures**", Reinforced Concrete Structures in Seismic Zones, ACI publication, SP-53, 1997, pp. 371-386.
- 6- ANSYS, "**ANSYS Help**", Release 11.0, Copyright 2007.
- 7- Taylor, H. P. J., "**The Behaviour of Insitu Concrete Beam-Column Joints**", London, Cement and Concrete Association, May, 1974, Technical Report No. 42.492, 32 pp.
- 8- Sarsam, K. F., "**Strength and Deformation of Structural Concrete Joints**", Ph.D. Thesis, University of Manchester Institute of Science and Technology, 1983, 340 pp.
- 9- Hadi Tuamma Al-Jubbori, "**The Effect of Hoops on The Shear Strength of Concrete Beam-Column Joints**", M.Sc Thesis,

- University of Technology, Baghdad, Iraq, 1986.
- 10- المواصفات القياسية العراقية/5 " سمنت بورتلاند الاعتيادي وسمنت بورتلاند سريع التصلب "، هيئة المواصفات والمقاييس العراقية ، مجلس التخطيط ، بغداد ، 1985 ، 8 صفحة .
 - 11- Abdullah, A.M., "**Shear Strength Of High-Strength Concrete Beams**", M.Sc Thesis, University of Technology, Baghdad 1987, 120 pp.
 - 12- ASTM Designation C 33-86., "**Concrete Aggregates**", 1989 Annual Book of ASTM , Standard American Society for Testing & Materials , Philadelphia, Pennsylvania, Section4, Vol. 04-02, pp 10-15.
 - 13- European Committee for Standardization (CEN), Eurocode 3, "**Design of Steel Structures**", Part 1.1: General Rules and Rules for Buildings, DD ENV 1993-1-1, EC3.
 - 14- ACI Committee 318, "**Building Code Requirements for Structural Concrete (ACI 318M-2008) and Commentary (ACI 318RM-2008)**", American Concrete Institute, Farmington Hills, USA, 2008.
 - 15- Bangash, M.Y.H., "**Concrete and Concrete Structures: Numerical Modelling and Applications**", Elsevier Science Publishers Ltd., London, England, 1989.
 - 16- Desayi, P. and Krishnan, S., "**Equation for the Stress-Strain Curve of Concrete**", Journal of the American Concrete Institute, Vol. 61, March 1964, pp. 345-350.
 - 17- Kachlakev, D., Miller, T. and Yim, S., "**Finite Element Modelling of Reinforced Concrete Structures Strengthened with FRP Laminates**", Final Report, SPR 316, May 2001, 99 p.
 - 18- ACI-ASCE committee 352 Report; "**Recommendations for Design of Beam-Column Joints in Monolithic Reinforced Concrete Structures**"; ACI Journal, V.82, No.3, May-June, 1985, pp. 266-283.
 - 19- Ehsani, M.R., and Wight, J.K., "**Exterior Reinforced Concrete Beam –to- Column Connections Subjected to Earthquakes-type Loading**", ACI Journal, V.82, No.4, July-August, 1985, pp. 449-492.
 - 20- Uzumeri, S. M., "**Strength and Ductility of Cast in Place Beam-Column Joints**", Reinforced Concrete Structures in Seismic Zones, ACI Publications, SP-53, 1977, PP. 293-350.
 - 21- Park, R., and Paulay, T., "**Reinforced Concrete Structures**"; John Wiley and Sons, 1975, 769 PP.
 - 22- Lee, D. L. N., Wight, J. K., and Hanson, R.D.; "**RC Beam-Column Joints under Large Load Reversals**", Journal of the Structural Division, V.103, No.ST-12, December, 1977, PP. 2337-2350.
 - 23- Paulay, T., Park, R., and Priestley, M. J. M., "**Reinforced Concrete Beam-Column Joints under Seismic Actions**", ACI journal, Nov., 1978, PP. 585-593.
 - 24- Marques, J. G. L., and Jirsa, J. O., "**A Study of Hooked Bar Anchorage in Beam-Column Joints**", ACI journal, V.72, No.5, May, 1975, PP. 198-209.

Table.1 Designation and Properties of Specimens

SP	Type; V_f %	D_H (mm)	N_u kN
1	0.0	-	100
2	0.0	4	100
3	0.0	8	100
4	H1.0	-	100
5	H1.0	4	100
6	H1.0	8	100
7	H1.0	-	150

Table.2 Properties of Reinforcement

Diameter	Modulus of elasticity (GPa)	f_y MPa	f_u MPa
8	202.42	466	598
12	203.55	440	606
16	201.0	507	661
18	197.4	531	704

H = hooked fibers, V_f %= percentage of fiber volume fraction, D_H = Diameter of hoop and N_u = Column axial Load.

Table.3 Test Results of Material Samples

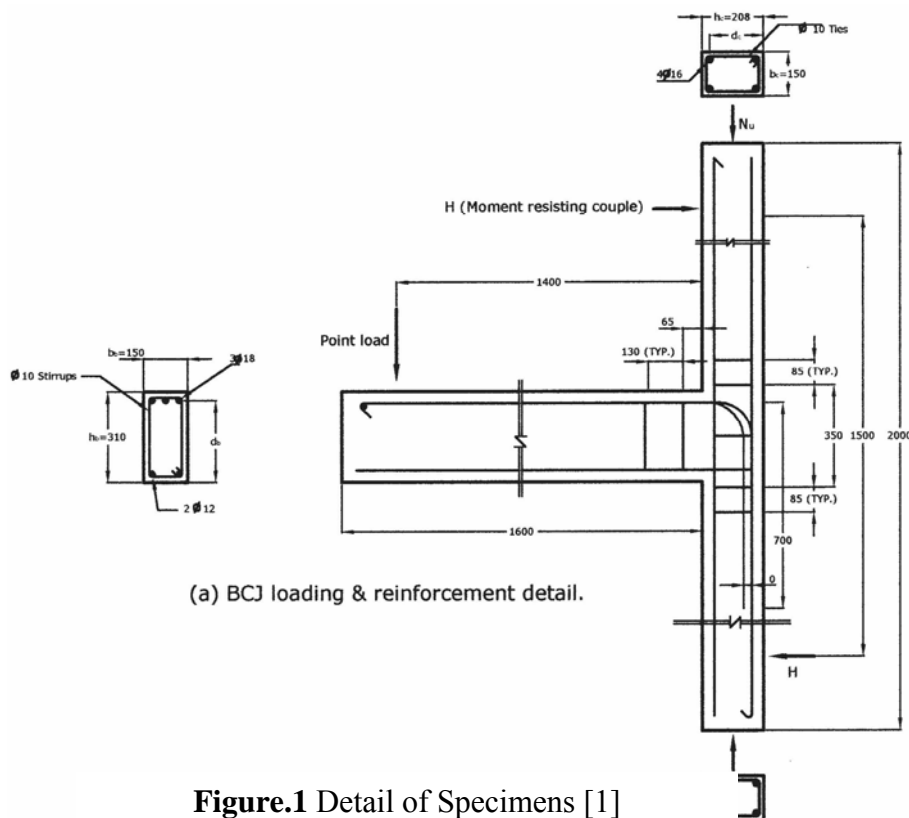
SP	f'_c (MPa)	f_r (MPa)	ν (mm/mm)	E_c (kN/mm ²)
1	60.40	7.500	0.138	34.09
2	61.10	8.950	0.155	33.21
3	59.40	7.200	0.145	33.48
4	67.50	11.37	0.240	33.33
5	67.95	12.50	0.235	34.65
6	66.70	11.00	0.237	32.90
7	66.30	10.86	0.243	32.69
8	68.54	10.66	0.248	35.26

Table.4 Material Models For the Elements

Material Model Number	Element type	Material Properties
1	Link8	Linear Isotropic
		EX 203550MPa
		PRXY 0.3
		Bilinear Isotropic
		Yield stress 440MPa
		Tangent modulus 20.3MPa
2	SOLID65	Linear Isotropic
		EX 34090MPa
		PRXY 0.138
		Multilinear Isotropic
		Strain Stress
		Point1 0.0005 17.5MPa
		Point2 0.001 34.5MPa
		Point3 0.0015 48.5MPa
		Point4 0.002 60.4MPa
		Point5 0.003 60.4MPa
		Concrete
		ShrCF-OP 0.15
		ShrCF-CL 0.6
		UnTensSt 7.5MPa
		UnCompSt -1
		BiCompSt 0
		HydroPrs 0
		BiCompSt 0
		UnTensSt 0
		TenCrFac 0
3	SOLID45	Linear Isotropic
		EX 200000MPa
		PRXY 0.3

Table.5 Test Results of Beam-Column Joint

SP	Type; V_f %	D_H (mm)	N_u kN	Ultimate Load (kN)		Analytical Experimental
				Experimental	Analytical	
1	0.0	-	100	45.2	48.0	1.06
2	0.0	4	100	56.0	54.0	0.96
3	0.0	8	100	65.5	59.5	0.91
4	H1.0	-	100	77.5	82.0	1.06
5	H1.0	4	100	89.0	86.0	0.97
6	H1.0	8	100	96.5	90.0	0.93
7	H1.0	-	150	87.2	88.0	1.01
8	H1.0	-	200	93.5	88.0	0.94


Figure.1 Detail of Specimens [1]

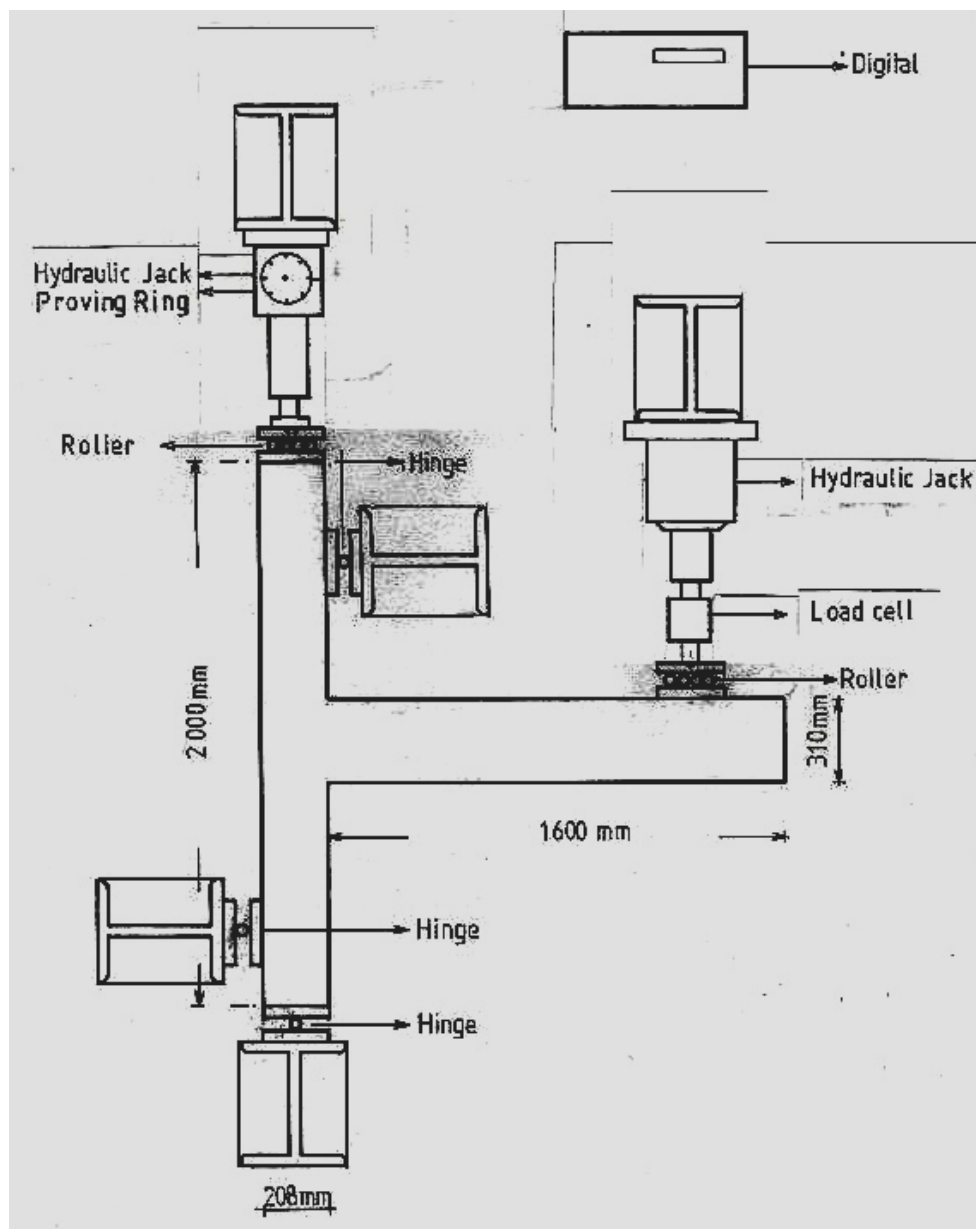


Figure.2 Testing Instrumentation [1]

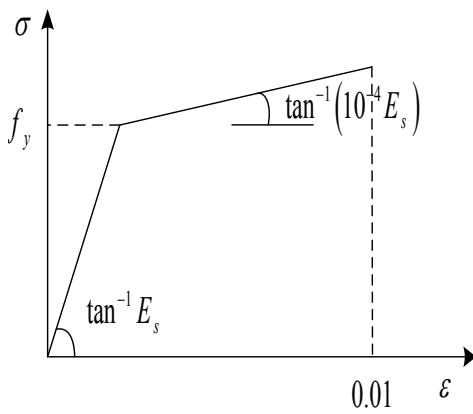


Figure.3 Bilinear stress-strain relationship of steel bars for computer calculations [13]

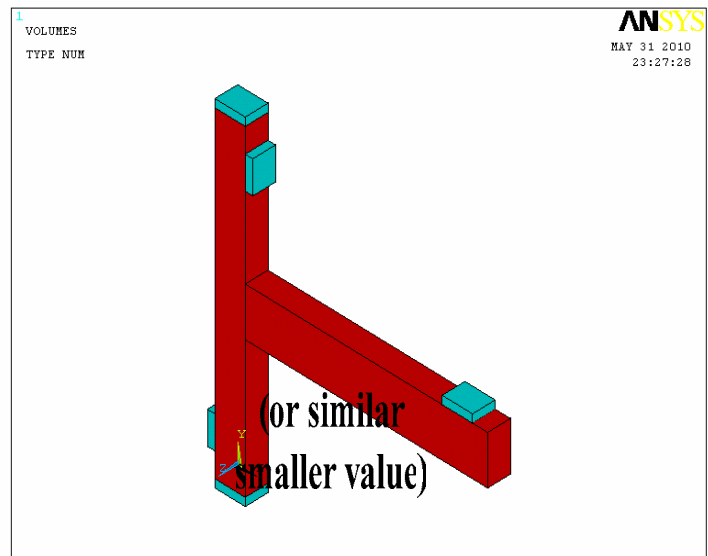


Figure.4 Solid model of beam-column joint

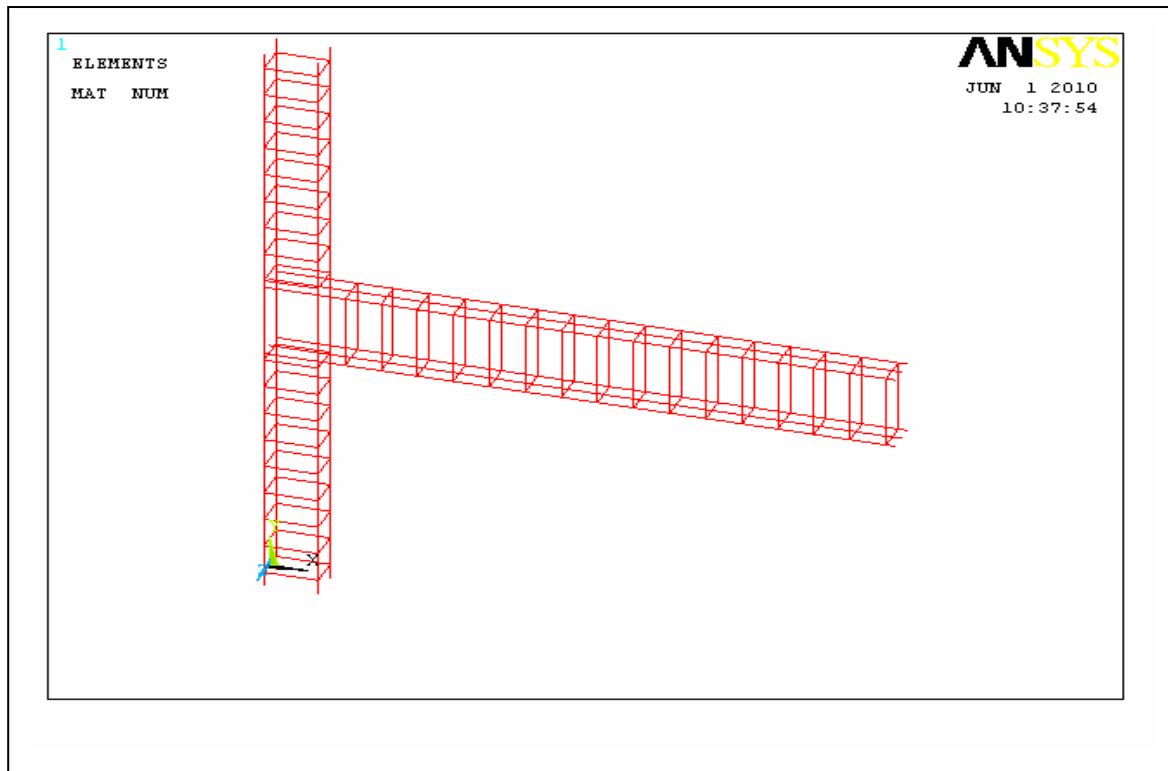


Figure.5 Solid Model of Beam-Column Reinforcement

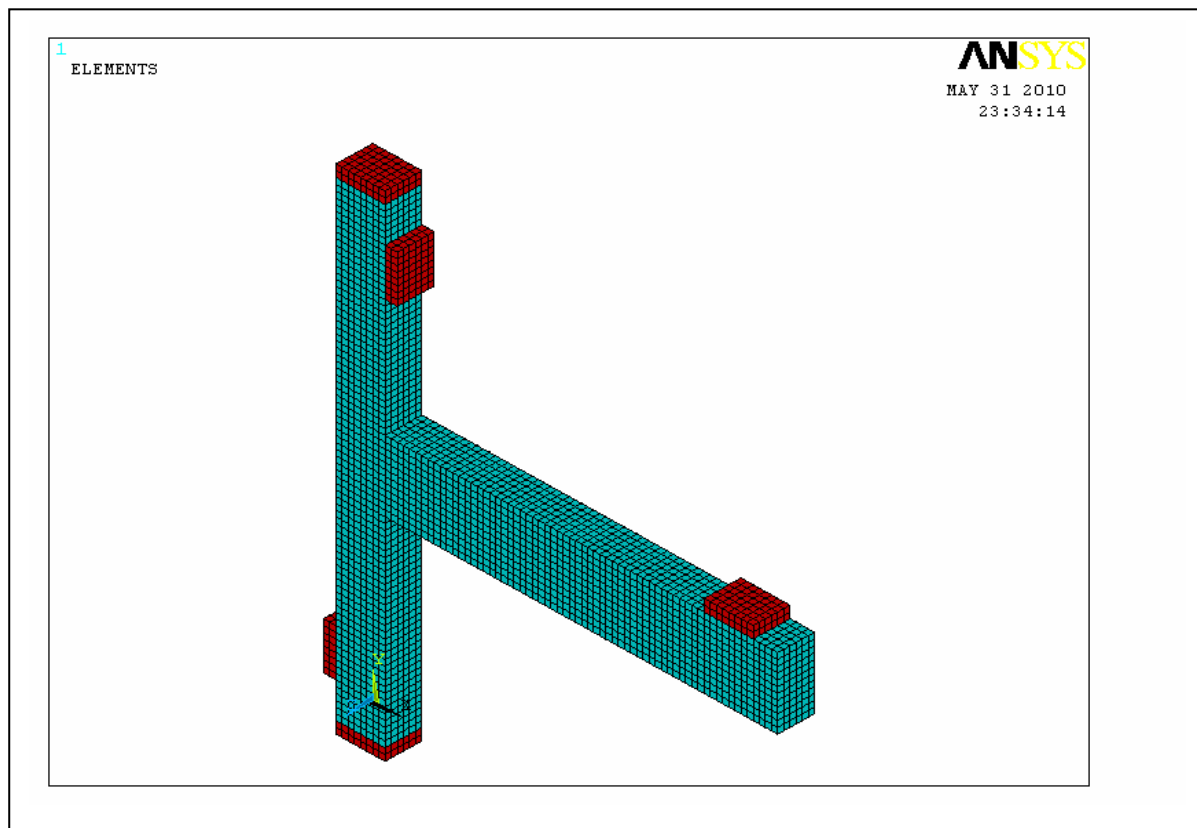


Figure.6 Finite Element Model of Beam-Column Joint

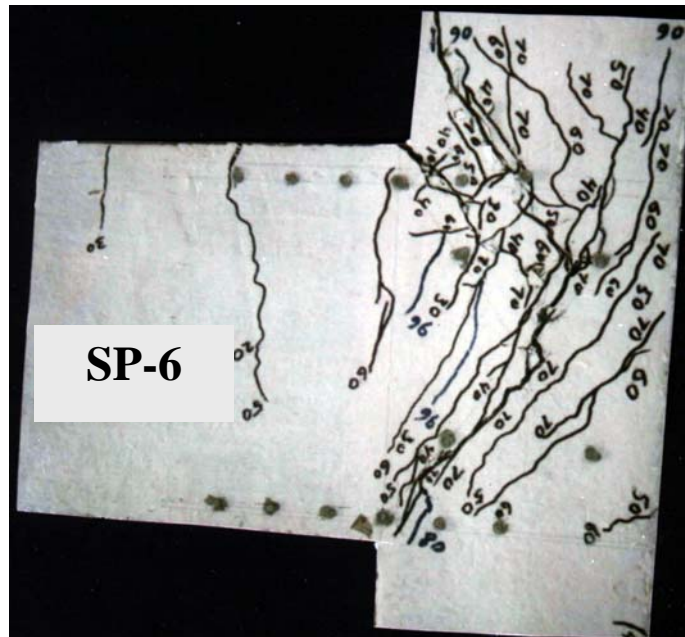


Figure.7 Cracked Specimen after Failure [1]

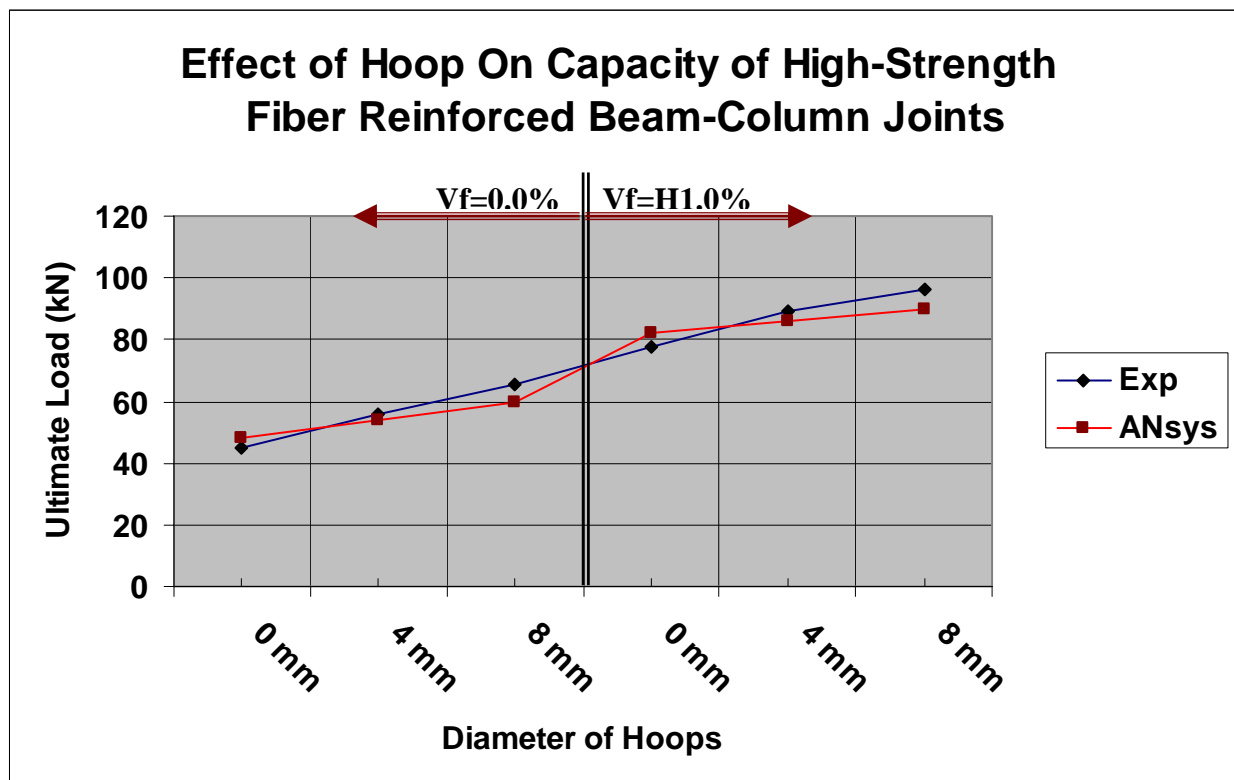


Figure.8 Effect of Hoop Diameter on Joint Strength

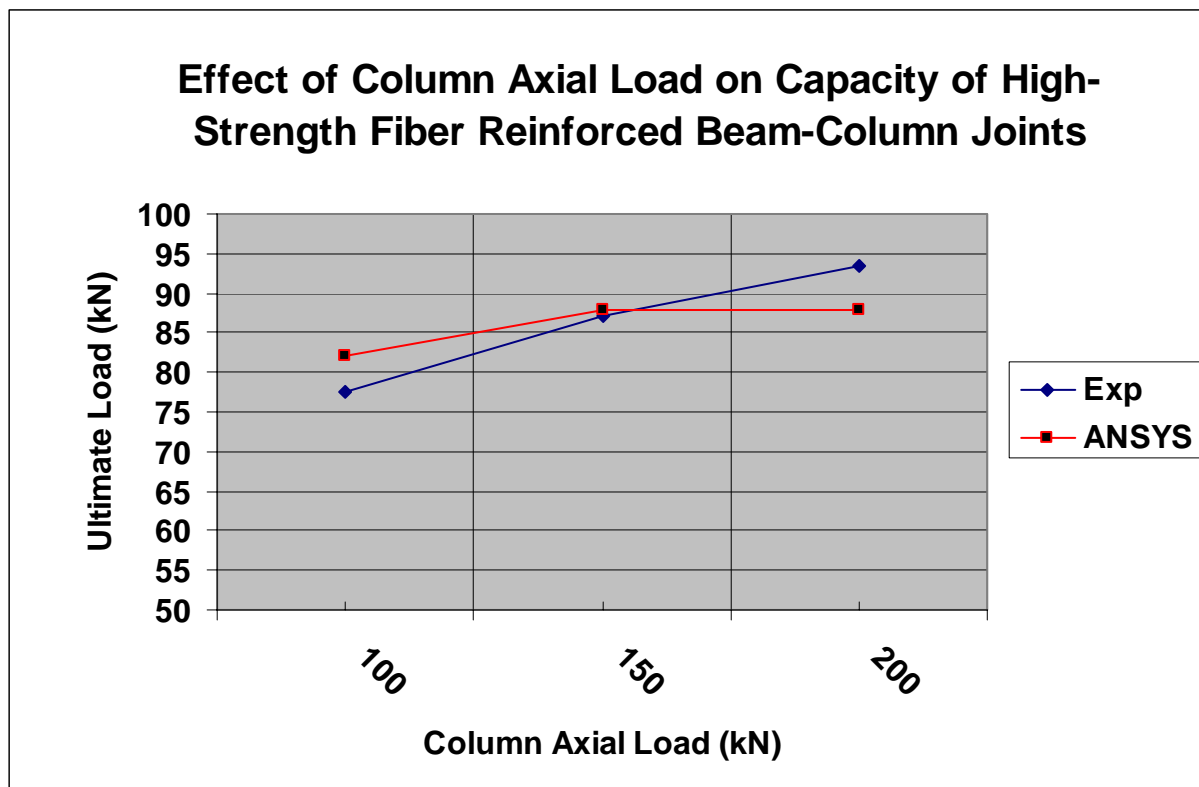


Figure. 9 Effect of Column Axial Load on Joint Strength

EVALUATION OF ELECTRONIC GOVERNMENT SECURITY ISSUES APPLIED TO COMPUTER CENTER OF BAGHDAD UNIVERSITY (CASE STUDY)

Ahmad O. Salman, Prof. Dr. Ghassan H. Abdul-Majeed, Ass. Prof. Dr. Tarik Z. Ismaeel

Abstract

Information security contributes directly to increase the level of trust between the government's departments by providing an assurance of confidentiality, integrity, and availability of sensitive governmental information. Many threats that are caused mainly by malicious acts can shutdown the e-government services. Therefore the governments are urged to implement security in e-government projects. Some modifications were proposed to the security assessment multi-layer model (*Sabri model*) to be more comprehensive model and more convenient for the Iraqi government. The proposed model can be used as a tool to assess the level of security readiness of government departments, a checklist for the required security measures and as a common security reference in the government organizations of Iraq. In order to make this model more practical, applicable and to represent the security readiness with a numerical value, evaluation modeling has been done for this model by using fuzzy logic tool of MATLAB R2010a program.

Since the risk assessment is considered as a major part in the information security management system, an effective and practical method to assess security risk is proposed by combining FEMRA (fuzzy expert model risk assessment) and Wavelet Neural Network (WNN). The fuzzy system is used to generate the training data set in order to make the required training for WNN. The proposed method is applied when a risk assessment case study is made at the computer center of Baghdad University. It is found from the numerical results that the risk levels obtained by WNN are (with maximum of 58.23) too close to these calculated from FEMRA (with maximum of 60), with an average error of 5.51%. According to these results, the proposed method is effective and reasonable and can provide the support toward establishing the e-government.

.R2010a

(58.23)
(60)
%5.51

KEY WORDS: E-Government, Security Model, Risk Assessment, Fuzzy Expert System, Wavelet Neural Network (WNN)

1. INTRODUCTION

E-Government is a kind of governmental administration, which is based on electronic information technology. The essence of e-government is using electronic information technology to break the boundary of administrative organizations, and build up a virtual electronic government [Zhitian and Congyang, 2008]. The concept of an e-government system is to provide access to government services anywhere at anytime over open networks. This leads to issues of security and privacy in the management of the information systems [Salahduddin, Lauren and Kavoos, 2008]. Governments are trying to deliver their services in ways that meet citizens, employees and businesses needs effectively and efficiently. The Internet allows a quick update and access to any information any time the user wants. E-Government is the most important accomplishment of Internet [Walid and Reem, 2008]. The information system security is an essential management responsibility for e-government that has as a target to fulfil the fundamental security properties of; confidentiality, integrity, availability, accountability and information assurance. A high level of confidence and trust among all users (citizens, businesses and government) will be the foundation of a successful e-government initiative [Costas, Stefanos, Fredj and Gunther, 2003]. The objective of information system security is to optimize the performance of an organization with respect to the risks to which it is exposed [Seymour and M.E. Kabay, 2002]. Without adequate protection or network security, many individuals, businesses, and governments are at risk of losing the assets [Salah, 2009]. A *security model* is a statement that outlines the requirements necessary to properly support and implement a certain security policy [Shon, 2009]. Models in the computer security field have generally been constructed as an aid in analyzing "security" properties of interest [D. Elliott, 1988]. Information security presents a lot of challenges and concerns to governmental and commercial organizations. Models are used as the best method for illustrating new concepts or architectures. It was noticed that all existing models were developed to address one aspect or a problem in the information security field. No comprehensive model was found, which addresses all aspects of security for any organization that offers e-services over Internet or a public network. This lead to develop a new model (multi-layer information

security assessment model) which contains multilayer representing the technologies, policies, competencies, operational procedures and decision layer [Sabri, 2008]. This model is named Sabri model in this paper.

Risk assessment provides organizations with an accurate evaluation of the risks to their assets. It can help them prioritize and develop a comprehensive strategy to reduce risks. It is very important to make a study on the theory and practice of the assessment of security risks in the information systems [Ming, SHU and XIAO 2008]. The aim of this paper is:

- To modify the multi layer information security readiness assessment model developed by Sabri (Sabri model) and evaluate it by using fuzzy logic, in order to make it more practical and applicable to the organizations of e-government.
- To propose an effective and practical method of security risk assessment for e-government information system. This method is built by combining two engineering techniques, fuzzy expert system (FEMRA) with wavelet neural network.

2. MULTI-LAYER INFORMATION SECURITY ASSESSMENT MODEL (SABRI MODEL)

The objective of the new security model is to assist in visualizing the combination of different layers of security in order to come up with a mechanism of enhancing the security level of any e-enabled organization but specifically in using the e-governments as the research case. Having more than one dimension or layer of any model gives the model a robust structure and a better success rate in preventing organizations from various categories of threats related to a single or multiple e-services. Each layer will mitigate group of threats related to an e-services. The layers as depicted in **Fig. 1** are, the technology layer, the policy layer, the competency layer, the operational and Management layer and the decision layer. The layers were constructed from the bottom to the top based on the importance of the layers and how they complement each other.

Since each layer has more than one sub layer and to make the structure coherent and more understandable, the model evolved into a matrix oriented structure, where each layer was divided into multiple sub layers as indicated in **Fig. 2**. The division of these layers into sub layers gives the

new model a flexibility to expand into n-number of cells based on the need of the organization [Sabri , 2008].

2.1 Modifications for Sabri Model

Modifications for the Sabri model were done based on the conditions of Iraq, supervisor's experience and analysis of the published works. **Fig. 2** shows the original model of Sabri without the modifications, whereas **Fig. 3** shows the model after making the modifications (modified Sabri model). The modifications include the followingin :

1. Addition of two elements to the technology layer (**VLAN & non-repudiation**). VLANs are used to segment networks for multiple reasons, the primary reason is to group together common hosts for security purposes. VLAN can allow one broadcast domain to be split into two or more domains that restrict an access to certain network resources. This can be a handy addition to user management and security strategy for the company. [Joshura, 2008] [Todd,2003]. Non-Repudiation is an important security service needed for many e-government applications. It will increase the confidence for both citizens and the government departments on e-government applications. [Hasala, Lakshan and Rohana, 2008].
2. Dividing the competency layer into two sub layers called **user sub layer** and **information security department sub layer**. The users of an organization should be classified into two parts (common users and security specialist users). Therefore, this division for this layer will help the users to know their security tasks. Three elements have been added to the user sub Layer called:
 - **Training and awareness:** Security awareness and training is an essential element of a comprehensive and effective security program, to keep staff aware of their responsibilities and role in implementing and maintaining security within the department [Parmar,2009].
 - **Security policies of department:** It is a set of rules and practices dictating how sensitive information is managed, protected, and distributed. Without a strong security policy that every employee must conform to, the organization may suffer from data loss, employee time loss, and productivity loss [Joseph,2005].
 - **Social engineering:** It can be defined as any attempt to gain unauthorized access to systems or resources by means other than software or hardware hacking. A little bit of psychology and some insight into the victim's character or habits is usually enough to mount a successful attack, under the right circumstances [Todd, 2003].
- Two elements have been added to the information security department sub layer called:
 - **cyber crime:** A cyber crime is a crime like any other crime, except that in this case, the illegal act must involve a connected computing system either as an object of a crime, an instrument used to commit a crime or a repository of evidence related to a crime [Joseph, 2009].
 - **Computer Security Incident Response Team (CSIRT):** It is critical for the organization to have a fast and effective means of responding. When an incident occurs, the goal of the CSIRT is to control and minimize any damage, preserve evidence, provide quick and efficient recovery, prevent similar future events, gain insight into threats against the organization and lower the cost of recovery [Georgia, Klaus-Peter, Robin and Mark, 2003].
3. Introduce a new layer called **physical layer**. Physical security is the term used to describe protection needed outside the computer system. Physical security is applied to prevent attackers from have a facility to gain data stored on servers, computers, or other mediums. [Charles and Shari, 2002] [Joshura , 2008]. Three elements have been added to this layer called **site design, access control devices** and **alarms and cameras**.
4. One element has been added to the decision layer called **data sensitivity**. Some databases contain what is called sensitive data. Sensitive data are data that should not be made public. Obviously, some databases, such as a public library catalogue, contain no sensitive data, other databases, such as defence-related ones, are totally sensitive [Charles and Shari, 2002].
5. Replacing the element (technologies availability) in the decision layer by **elements availability**. Specific weight has been assigned to each layer, to take account the effect of all the layers during the decision making process, instead of depending on one layer (technology layer). Technology layer will take weight value 0.6, because it considers the important layer as recommended by Sabri model, and each of other layers will take 0.1 as a weight value. Therefore, the element (technologies

availability) is replaced by elements availability.

2.2 Evaluation of Modified Sabri Model Using Fuzzy Logic

In this section, the modified Sabri model will be evaluated using fuzzy logic. The fuzzification of input variables is based on three major elements (*cost*, *data sensitivity* and *elements availability*) in the decision layer of the model. The design is based on the Mamdani style inference system which is very good for the representation of human reasoning and effective analysis. The implementation is done using the fuzzy logic tool of MATLAB R2010a.

The aim of this work is to assess the level of security readiness of government organizations and make decisions by using fuzzy logic instead of human reasoning. Fuzzy logic-based evaluation modeling architecture is given in **Fig. 4**.

Linguistic values are assigned for the inputs, *cost* and *data_sensitivity* as *Low*, *Medium*, and *High*, whereas the Linguistic value for the input (*elements_availability*) is assigned as *Bad*, *Good*, and *Excellent*. The Linguistic value for the output (*trend_level*) is assigned as *Very low*, *Low*, *Medium*, *Rather high*, *High* and *Very high*. The universe of discourse of the input and output variables in this case ranges from 0 to 100. **Table 1** contains the linguistic variables and their ranges.

Fig. 5 displays information about FIS editor (decision). It shows the names of input and output variables. **Fig. 6** is used to add, change or delete rules.

2.3 Determine the Value of Elements Availability

The decision of launching or not launching an e-service using the fuzzy evaluation of the modified Sabri model depends on some elements. One of these elements is (*elements availability*). In order to determine easily the value of this element with more accurate, a function was written using the built-in editor of MATLAB R2010a. The name of this function is *elements_avail*. It has two arguments (x1 and x2). The first argument (x1) is a row vector that represents the elements selected by security manager or designer from the modified Sabri model. The second argument (x2) is a row vector that represents the type of security service (*confidentiality*, *integrity*, *availability*,

authentication and *non repudiation*) required for establishing an e-service. Each security service takes one value (1, 2, 3, 4 and 5 respectively) to represent it inside the function (*elements_avail*). The output of this function is (*elements_availability*) that represents the value of the element (*elements availability*) will be taken as input in the fuzzy model (decision).

3. SECURITY RISK ASSESSMENT

A Risk can be described as the potential of a threat to exploit a vulnerability found in an asset [Todd, 2003]. A risk exists when there is a possibility of a threat to exploit the vulnerability of a valuable asset. That is, three elements of a risk are *asset*, *vulnerability* and *threat*. The value of an asset makes it a target for an attacker. The vulnerability of an asset presents the opportunity of a possible asset damage or loss. A threat is a potential attack which can exploit a vulnerability to attack an asset [Nong, 2008]. The measure of risk can be determined as a product of threat, vulnerability and asset values as shown in the formula below:

$$\text{Risk} = \text{Asset} \times \text{Threat} \times \text{Vulnerability} \quad (1)$$

With the progress of the construction of the e-government information systems of different levels, the government provides management and services with higher quality and more efficient for the society. So, it is very important to make a study on the theory and practice of the assessment of security risks in information systems [Ming, 2008]. The basic steps for risk assessment are listed as follows [John, 2001] [AS/NZS, 2004]:

1. Identifying and prioritizing assets.
2. Identifying vulnerabilities.
3. Identifying threats and their probabilities.
4. Estimate level of risk
5. Developing a cost benefit analysis.
6. Developing security policies and procedures.

A powerful tool is needed to assess the risk within an organization. The WNN (wavelet neural network) has the intelligent features such as self-learn, obtaining knowledge, which is different to the conventional methods (AHP, fuzzy logical and so on), and can dissolve the uncertain problems [DONG-MEI, 2009]. In this paper, the fuzzy theory and method of Wavelet Neural Network (WNN) are combined to assess the risk level. Since the artificial neural network is suited for the quantity data processing, and poor to the qualitative analyze, therefore the fuzzy expert systems (FEMRA) method was built and applied

firstly to assess the risk factors (training data set). Secondly, the WNN was built to assess the risk level quantitatively.

3.1 Fuzzy Expert Model for Risk Assessment (FEMRA)

The steps of implementation FEMRA will be given below [Alireza, Masoume, Mehdi and Michel, 2010]:

Step 1: Assets classification and identification

Step 2: Threat Identification

Step 3: CIA Triad Evaluation

Evaluating the CIA (confidentiality, integrity and availability) triad is a key to calculate the organization's risks. The base of the CIA triad could be calculated with the following formulas:

$$w_c = \frac{\sum_{e=1}^n C_e}{n}, \quad w_i = \frac{\sum_{e=1}^n I_e}{n}, \quad w_a = \frac{\sum_{e=1}^n A_e}{n} \quad (2a)$$

Since authentication is important service and main part in computer security system [Mark, 2006][William, 2005][Joseph, 2005], therefore it is added to the CIA triad evaluation.

$$w_{AU} = \frac{\sum_{e=1}^n AU_e}{n} \quad (2b)$$

Where n represent the number of experts. C_e, I_e, A_e and AU_e represent the weights of confidentiality, integrity, availability and authentication that assigned by the experts.

Step 4: Vulnerability Identification

Step 5: Risk Identification

Step 6: Asset Value

Each expert assigns a value from 1 to 9 to each part of CIA triad based on the **Table 2**.

Table 2 Risk level range

The asset's value could be calculated with formula below:

$$asset_{value} = \sum_{(CIA+AU)=1}^4 \left(\frac{\sum_{e=1}^n (CIA+AU)_e}{n} \right) * w_{(CIA+AU)} \quad (3)$$

Where n represent the number of experts, w_{CIA+AU} represent the base of the CIA triad and authentication part and $(CIA + AU)_e$ represent

CIA triad and authentication values of an asset based on expert assignment.

Step 7: Vulnerability Effect

Vulnerability effects will be represented with a percentage, and for better accuracy, it is prefer to get help from n experts. The vulnerability effect could be calculated with formula below:

$$vulnerability_{effect} = \frac{\sum_{e=1}^n effect}{n} \quad (4)$$

Step 8: Threat Effect

The calculation method of threats is similar to the one for assets. Each expert assigns a value from 1 to 9 to each part of CIA triad plus authentication based on **Table 2**. The threat effects could be calculated with formula 5.

$$threat_{value} = \sum_{(CIA+AU)=1}^4 \left(\frac{\sum_{e=1}^n (CIA+AU)_e}{n} \right) * w_{(CIA+AU)} \quad (5)$$

Risk Effects (level) modelling

The risk effects modelling are built using the fuzzy model tool of MATLAB R2010a environment. Three parameters are used as input in this modelling: *asset values*, *vulnerability effects* and *threat effects*. **Fig. 7** below shows the architecture of this model.

3.2 Risk Evaluation Based on Wavelet Neural Network Model

The basic structure of proposed WNN is illustrated in **Fig. 8**, which consists of three layers. The first layer is the input layer, which has three nodes ($i=1, \dots, 3$) as following: *asset value*, *vulnerability effect* and *threat effect*. The second layer is a hidden layer, which has H nodes that needs adjusting in the experiment. The third layer is an output layer, which has one node ($m=1$) for putting out a risk effect (risk level).

w_{hi} and w_{mh} are defined respectively as the weight coefficient of the hidden layer and the output layer. The output of a wavelon is defined as:

$$\psi_{a,b}(u) = \psi\left(\frac{u-b}{a}\right) \quad (6)$$

Where $\psi(\cdot)$, a and b are the mother wavelet function, dilation and translation parameters respectively. The activation function of the hidden layer is defined as Marr function:

$$\psi(t) = (1 - t^2) \exp(-t^2 / 2) \quad (7)$$

The active function of output layer is defined as a sigmoid function:

$$f(\text{net}) = 1 / (1 + \exp(-\text{net})) \quad (8)$$

4. CASE STUDY

In order to verify the validity of our proposed method (fuzzy wavelet neural network) and test its ability of risk assessment for e-government network security, experiments were carried out in the computer center at the University of Baghdad. In this study, the FEMRA method was applied firstly to assess the risk factors (training data set), then the WNN is applied to assess the risk level. Three security experts from computer center are used to do this study. The results of this case study are indicated by the following steps:

Step 1: CIA Triad Evaluation

The sum of the weights for all parts must be equal to one. Note that the authentication service is added in this step (eq. 2b), so it will be entering in the calculation of this evaluation. **Table 3** shows this evaluation.

When the eq. (2) is applied on the **Table 3**, the base of the CIA triad and authentication evaluation could be calculated. **Table 4** shows the values of the bases.

Step 2: Asset value

Table 5 shows the asset identification for computer center. Each expert assigned a value from (1 to 9) to each part (confidentiality, integrity, availability and authentication) of an asset. Then eq. (3) is applied to calculate the asset value for each asset. **Table 6** shows the asset value.

Step 3: Vulnerability effect

Table 7 shows the asset's vulnerabilities for the assets of the computer center.

Each expert assigned a value from (0 to 100) for each asset's vulnerability (**Table 8**). Then eq. (4) is applied to calculate the vulnerability effect. **Table 8** shows the vulnerability effects.

Step 4: Threat effect

Table 9 shows the threat identification for computer center.

Each expert assigned a value from (1 to 9) to each part of a threat in **Table 9**. Then eq. (5) is applied to calculate the threat effect for each threat. **Table 10** shows the threat effect.

Step 5: Risk effect (level)

Based on the previous collected data (**Tables 5, 7 and 9**), the relationship among the assets, vulnerabilities and threats will be determined. The relationship between each vulnerability and threat is a risk. **Table 11** illustrates some risks within the computer center. Dependent on the **Table 2**, the risk effect will be divided into three levels ($1 \leq \text{low} < 35$, $35 \leq \text{med} < 65$, $65 \leq \text{high} < 100$).

The risk effect can be calculated by using the fuzzy model of FEMRM. **Table 12** shows the results to assess the risks in the computer center.

4.4 Results of Risk Evaluation Based on WNN

Table 13 shows the result of comprehensive evaluating of risk level for the computer center by WNN.

Table 14 shows the contrast between the FEMRA result (desired output) and the output of WNN.

5. CONCLUSIONS

- E-Government network security is complicated process, and it requires periodically evaluation. Building secure e-government system requires a comprehensive security model.
- Modified Sabri model is an enhanced security readiness assessment model that is designed especially for e-government system. This enhanced model considers an essential tool that can be used by decision makers and designers of e-government security systems. The modified Sabri model is more effective than Sabri model, because it deals with numerical values instead of conceptual elements and all the layers of the model are contributing in making the decision instead of dependence on the technology layer only. This contribution is achieved by assigning a weight value for each layer. The modified Sabri model can help the security managers to assess the security readiness of their department with high accuracy.
- Combine two engineering techniques (fuzzy system with wavelet neural network) enables the governmental organizations to overcome the difficulty of finding the required training data set to build the wavelet neural network, and reduce the level of dependence on the experts and the time required to assess the risks in their departments.

- The numerical results from the real case study of risk assessment indicate that WNN can improve effectively the assessment accuracy and speed. The contrast result between WNN and FEMRA shows that the risk evaluation method based on the WNN can provide a credible algorithm for the risk assessment of information security.

REFERENCES

- Alireza S. Sendi, M. Jabbarifar, M. Shajari and M. Dagenais, "FEMRA: Fuzzy Expert Model for Risk Assessment", Proceedings of the IEEE International Conference on Internet Monitoring and Protection, pp.48-53, 2010.
- AS/NZS, "Risk Management", SAI Global, Third Edition, 2004.
- Charles P. Pfleeger and Shari L. Pfleeger, "Security in Computing", Prentice Hall, third edition, 2002.
- Costas Lambrinoudakis, S. Gritzalis, F. Dridi and G. Pernul, "Security Requirements for E-Government Services: A Methodological Approach for Developing A Common PKI-based Security Policy", Elsevier, Computer Communications 26, 1873–1883, 2003.
- D. Elliott Bell, "Concerning Modeling of Computer Security", Proceedings of the IEEE International Symposium on Security and Privacy, pp.8-13, 1988.
- Georgia Killcrece, Klaus-Peter Kossakowski, Robin Ruefle and Mark Zajicek, "Organizational Models for Computer Security Incident Response Teams (CSIRTs)", Carnegie Mellon University, 2003.
- Hasala Peiris, Lakshan Soysa and Rohana Palliyaguru, "Non-Repudiation Framework for E-Government Applications", Proceedings of the IEEE International Conference on Information and Automation for Sustainability, pp.307-313, 2008.
- John E. Canavan, "Fundamentals of Network Security", British Library, London, 2001.
- Joseph M. Rizza, "Computer Network Security", Springer, 2005.
- Joseph M. Rizza, "A Guide to Computer Network Security", Springer, 2009.
- Joshua Backfield, "Network Security Model", SANS Institute, 2008.
- Mark Stamp, "Information Security Principles and Practice", John Wiley & Sons, 2006.
- Ming Liu, S. Sun and X. Yin, "Research on The Evaluation of Security Risk for E-Government Information System" Proceedings of the IEEE International Conference on Machine Learning and Cybernetics, Vol.3, pp.1404-1409, 2008.
- Nong Ye, "Secure Computer and Network Systems Modeling, Analysis and Design", John Wiley & Sons Inc., 2008.
- S. K. Parmar, "Information Resource Guide Computer, Internet and Network Systems Security", security manual, sunny, Canada, June 2009.
- Sabri Al-Azazi, "A Multi-layer Model for E-Government Information Security Assessment", PhD thesis, Cranfield University, 2008.
- Salah Alabady, "Design and Implementation of A Network Security Model for Cooperative Network", International Arab Journal of e-Technology, Vol. 1, No. 2, June 2009.
- Salahuddin Alfawaz, L. May and K. Mohanak, "E-Government Security in Developing Countries: A Managerial Conceptual Framework", International Research Society for Public Management Conference, 2008.
- Seymour Bosworth and M.E. Kabay, "Computer Security Handbook", John Wiley & Sons, Fourth Edition, 2002.
- Shon Harris, "CISSP All-in-One Exam Guide", McGraw Hill, Fifth Edition, 2009.
- Todd King, "Security + Training Guide", Paul Boger, 2003.
- Walid Al-Ahmad and R. Al-Kaabi, "An Extended Security Framework for E-Government", Proceedings of the IEEE International Conference on Intelligence and Security Informatics, pp. 294-295, 2008.
- William Stallings, "Cryptography and Network Security Principles and Practices", Prentice Hall, Fourth Edition, 2005.

Zhitian Zhou and Congyang Hu, "Study on the E-Government Security Risk Management", IJCSNS International Journal of Computer Science and Network Security, Vol.8 No.5, May 2008.

NOTATION

W_C Confidentiality Base

W_I Integrity Base

W_A Availability Base

C_e Confidentiality Expert Weight

I_e Integrity Expert Weight

A_e Availability Expert Weight

w_{CIA} Base of the CIA Triad

w_{CIA+AU} Base of the CIA Triad and

Authentication Part

$(CIA + AU)_e$ CIA Triad and Authentication

Values of an Asset Based on Expert Assign.

net Scalar Product of the Weight and Input

Vector

$\psi(u)$ Mother Wavelet

W_{hi} Weight Coefficient of the Hidden Layer

W_{mh} Weight Coefficient of the Output Layer

Table 1 Linguistic variable and their ranges

Linguistic variable	Linguistics value	Numerical range	Membership function type
<i>Cost</i>	Low	[0 0 20 40]	Trapezoidal
	Med	[20 60 95]	Triangular
	High	[60 90 100 100]	Trapezoidal
<i>Data_Sensitivity</i>	Low	[0 0 20 40]	Trapezoidal
	Med	[20 55 90]	Triangular
	High	[55 90 100 100]	Trapezoidal
<i>Elements_availability</i>	Bad	[0 0 25 40]	Trapezoidal
	Good	[20 60 100]	Triangular
	Excellent	[60 100 100]	Triangular
<i>Trend_level</i>	Very low	[0 0 30]	Triangular
	Low	[10 30 50]	Triangular
	Medium	[30 50 65]	Triangular
	Rather high	[55 65 75]	Triangular
	High	[65 75 85]	Triangular
	Very high	[75 100 100]	Triangular

Table 2 Risk level range

Level	Level	Effect
High	High	9
	Medium	8
	Low	7
Medium	High	6
	Medium	5
	Low	4
Low	High	3
	Medium	2
	Low	1

Table 3 CIA triad and authentication evaluation

Expert	Confidentiality (W_C)	Integrity (W_I)	Availability (W_A)	Authentication (W_{AU})
E1	0.3	0.3	0.1	0.3
E2	0.35	0.3	0.1	0.25
E3	0.35	0.25	0.1	0.3

Table 4 CIA base value

Base	Value
Confidentiality (W_C)	0.333
Integrity (W_I)	0.283
Availability (W_A)	0.1
Authentication (W_{AU})	0.283

Table 5 Asset identification

Id	Asset
A1	User (Instructor)
A2	Web data (questions and results of IC3 examination)
A3	License application
A4	Router
A5	Server
A6	Storage resources

Table 6 Asset value

Id	Asset	Confidentiality			Integrity			Availability			Authentication			Asset Value
		E1	E2	E3	E1	E2	E3	E1	E2	E3	E1	E2	E3	
A1	User (Instructor)	5	6	6	2	2	2	2	1	1	6	5	5	4.1
A2	Web data	7	8	8	7	7	6	5	5	4	7	6	6	6.7
A3	License Application	3	2	3	3	2	2	6	7	7	4	5	5	3.54
A4	Router	5	5	6	7	6	7	2	3	2	7	8	7	5.97
A5	Server	5	5	4	4	5	6	7	6	8	5	5	6	5.18
A6	Storage Resources	5	4	4	7	7	6	2	3	3	6	5	5	5.11

Table 7 asset's vulnerabilities

Id	Asset	Vulnerability
V1	A1 (Instructor)	User personality
V2	A2(Web data)	Administrative mistake, Poor protection
V3	A3 (License application)	Not using a mixed authentication mode
V4	A4 (Router)	Hardware defect, Configuration error
V5	A5 (Server)	Unsuitable location
V6	A6 (Storage resources)	Hardware defect, poor security

Table 8 Vulnerability effect

Asset Id	Vulnerability Id	Effect (%)			Vulnerability Effect (%)
		E1	E2	E3	
A1	V1	70	70	80	73.33
A2	V2	70	60	60	63.33
A3	V3	60	50	40	50
A4	V4	50	50	60	53.33
A5	V5	60	50	50	53.33
A6	V6	70	70	60	66.66

Table 9 Threat identification

Id	Threat
T1	Malicious Code (viruses, worms...etc.)
T2	Social engineering
T3	Hacker
T4	Equipment failure
T5	Intruder
T6	Human Errors
T7	DoS
T8	Physical theft

Table 10 Threat effect

Id	Threat	Confidentiality			Integrity			Availability			Authentication			Threat Effect
		E1	E2	E3	E1	E2	E3	E1	E2	E3	E1	E2	E3	
T1	Malicious Code	5	6	6	5	5	6	7	7	8	3	4	4	5.17
T2	Social engineering	7	7	8	3	2	2	2	2	1	7	6	6	5.07
T3	Hacker	6	6	7	6	5	5	1	2	2	7	7	6	5.67
T4	Equipment failure	2	1	2	2	2	1	7	8	6	1	1	2	2.1
T5	intruder	7	6	7	5	5	6	2	1	2	7	7	6	5.78
T6	Human Errors	5	5	4	6	5	6	2	2	1	4	5	5	4.65
T7	DoS	2	2	2	1	1	2	7	8	8	2	2	1	2.82
T8	Physical theft	5	5	4	2	2	1	6	7	7	2	1	1	3.07

Table 11 Some Risks in the computer center

Asset Id	Vulnerability Id	Threat Id	Risk Id
A1 User (Instructor)	V1 User personality	T2 Social engineering	R1 (loss of secrecy)
A2 Web data	V2 Administrative mistake	T6 Human Errors	R2 (data corruption)
A2 Web data	V2 Poor protection	T3 Hacker	R3 (company image)
A3 License application	V3 Not using mixed authentication mode	T6 Human Errors	R4 (loss of business or financial)
A4 Router	V4 Hardware defect	T4 Equipment failure	R5 (loss availability)
A4 Router	V4 Configuration error	T5 Intruder	R6 (security Compromise)
A5 Server	V5 Unsuitable location	T8 Physical theft	R7 (loss availability)
A5 (Server)	V5	T7 DoS	R8 (loss e-service)
A6 (Storage resources)	V6 Hardware defect	T4 Equipment failure	R9 (loss data)
A6 (Storage resources)	V6 poor security	T1 Malicious Code	R10 (data corruption)

Table 12 Risk effect

Risk Id	Asset Value (1-9)	Vulnerability Effect (1-100)	Threat Effect (1-9)	Risk Effect (level) (1-100)		
				low	med	high
R1	4.1	73.33	5.07		60	
R2	6.7	63.33	4.65		53.2	
R3	6.7	63.33	5.67		53.2	
R4	3.54	50	4.65		39.5	
R5	5.97	53.33	2.1	26.6		
R6	5.97	53.33	5.78		45.6	
R7	5.18	53.33	3.07		37.4	
R8	5.18	53.33	2.82	32.1		
R9	5.11	66.66	2.1		41.4	
R10	5.11	66.66	5.17		54.8	

Table 13 Risk effect using WNN

Risk Id	Input			output (Risk Level)		
	Asset Value	Vulnerability Effect	Threat Effect	Low	Med	High
R1	4.1	73.33	5.07		58.23	
R2	6.7	63.33	4.65		51.18	
R3	6.7	63.33	5.67		55.81	
R4	3.54	50	4.65		36.33	
R5	5.97	53.33	2.1	23.46		
R6	5.97	53.33	5.78		47.73	
R7	5.18	53.33	3.07		35.41	
R8	5.18	53.33	2.82	30.85		
R9	5.11	66.66	2.1		39.85	
R10	5.11	66.66	5.17		56.72	

Table 14 Contrast between desired output and output of WNN

Desired Output (FEMRA) Risk Level			WNN Risk Level			Absolute Error	Max Error	Min Error	Average Error
Low	Med	High	Low	Med	High				
	60			58.23		1.77	3.17	1.25	2.155
	53.2			51.18		2.02			
	53.2			55.81		2.61			
	39.5			36.33		3.17			
26.6			23.46			3.14			
	45.6			47.73		2.13			
	37.4			35.41		1.99			
32.1			30.85			1.25			
	41.4			39.85		1.55			
	54.8			56.72		1.92			



Fig. 1 multi layers model

Security Layers	Sub Layers / Cells					
Technology Layer	A1: Access Control	A2: Intrusion Detection Prevention	A3: Anti-Virus & Malicious Codes Signature	A4: Authentication and Passwords	A5: Files Integrity Checks	A6: Cryptography
	A7: VPN	A8: Vulnerability Scanning Tools	A9: Digital Signature and Certificate	A10: Biometrics	A11: Logical Access Control (Firewall)	A12: Security Protocols
Policy Layer	B1: Password Management	B2: Log-In Process	B3: Logs Handling	B4: Computer Viruses	B5: Intellectual Property Rights	B6: Data Privacy
	B7: Privilege Control	B8: Data Confidentiality	B9: Data Integrity	B10: Internet Connectivity	B11: Administrative Policies	B12: Encryption Policies
	B13: HR Security Policies	B14: Third Party Policies	B15: Physical Security Policies	B16: Operation Security Policies		
Competency Layer	C1: Security Operation and Management	C2: Security Architecture and Development	C3: Ethical Hacking	C4: Security Policies Development	C5: Computer Forensics	C6: Cryptography
	C7: Security Programming	C8: Laws and Regulations	C9: Security Implementation and Configuration	C10: Security Analysis		
Operation and Management Layer	D1: Operational Policies and Procedures	D2: Management Tool	D3: Correlation and Data Mining	D4: Reporting and Response	D5: Analysis and Human Intervention	
Decision Layer	F1: Cost	F2: Awareness	F3: Need	F4: Technologies Availability	F5: FUD	

Fig.2 Sabri model

Security Layers	Sub Layers / Cells						
Technology Layer	A1: VLAN	A2: Access Control	A3: Intrusion Detection prevention	A4: Anti-Virus & Malicious Codes Signature	A5: Authentication and passwords	A6: Files Integrity Checks	A7: cryptography
	A8: VPN	A9: Vulnerability Scanning Tools	A10: Digital Signature and Certificate	A11: Biometrics	A12: Logical Access Control (Firewall)	A13: Security Protocols	A14: non-repudiation
Policy Layer	B1: Password Management	B2: Log-In Process	B3: Logs Handling	B4: Computer Viruses	B5: Intellectual property Rights	B6: Data Privacy	B7: Privilege Control
	B8: Data Confidentiality	B9: Data Integrity	B10: Internet Connectivity	B11: Administrative policies	B12: Encryption policies	B13: HR Security Policies	B14: Third Party Policies
	B15: Physical Security Policies	B16: Operation Security Policies					
Competency Layer	User Sub Layers	C1: Training and Awareness	C2: Security Policies of Department	C3: Ethical Hacking	C4: Social Engineering		
	Information security Department	C5: Security Operation and Management	C6: Security Architecture and Development	C7: Security Policies Development	C8: Computer Forensics	C9: Cryptography	C10: Security Programming
	Sub Layers	C11: Laws and Regulations	C12: Security Implementation and Configuration	C13: Security Analysis	C14: Cyber Crime	C15: CSIRT	
Operation and Management Layer	D1: Operational Policies and Procedures	D2: Management Tool	D3: Correlation and Data Mining	D4: Reporting and Response	D5: Analysis and Human Intervention		
Physical Layer	E1: Site Design	E2: Access Control Devices	E3: Alarms and Cameras				
Decision Layer	F1: Cost	F2: Awareness	F3: Need	F4: Elements Availability	F6: FUD	F5: Data Sensitivity	

Fig.3 Modified Sabri model

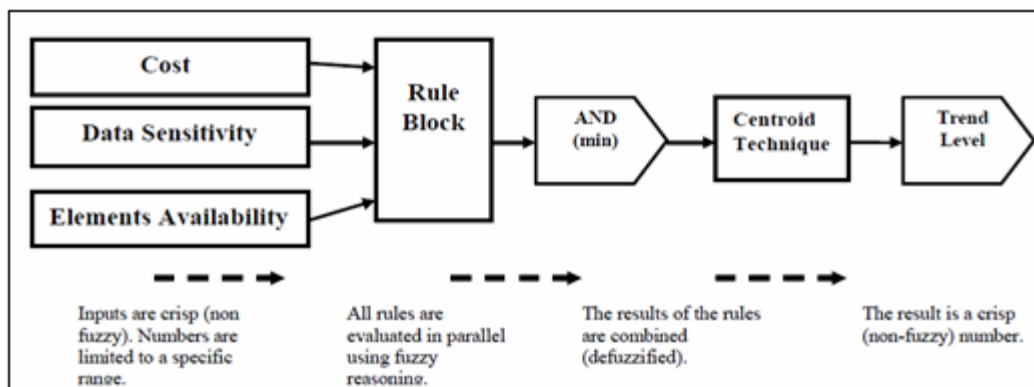


Fig. 4 Architecture for fuzzy logic-based evaluation modeling

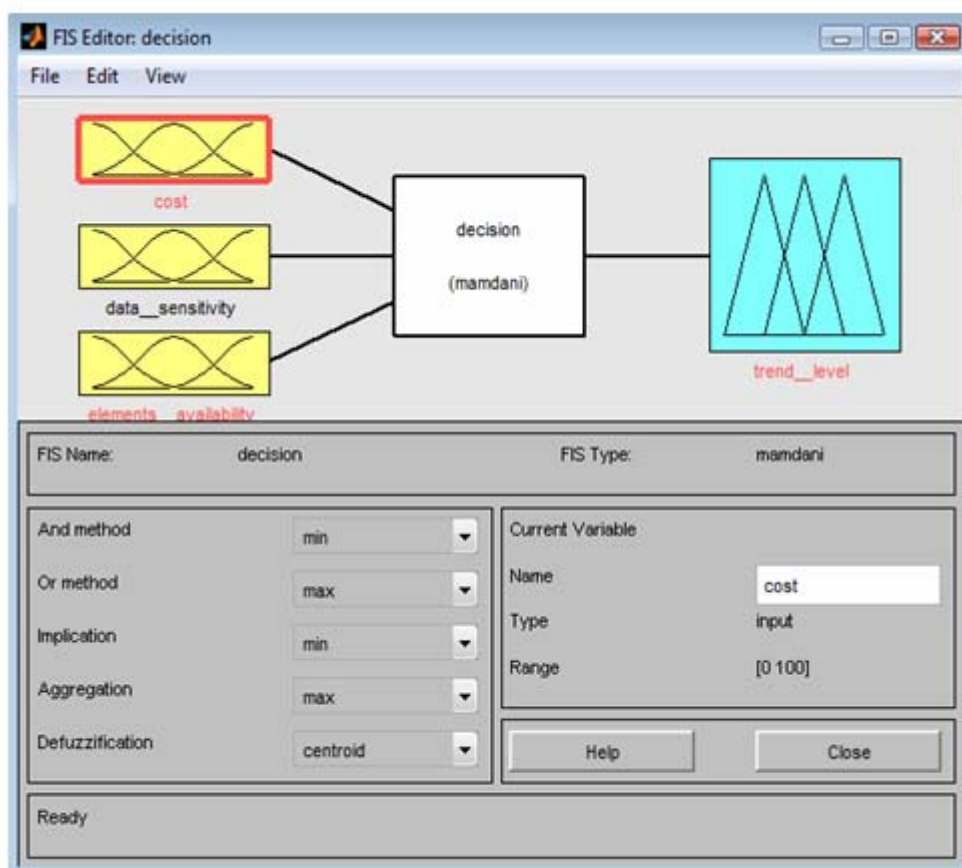


Fig. 5 FIS editor (decision)

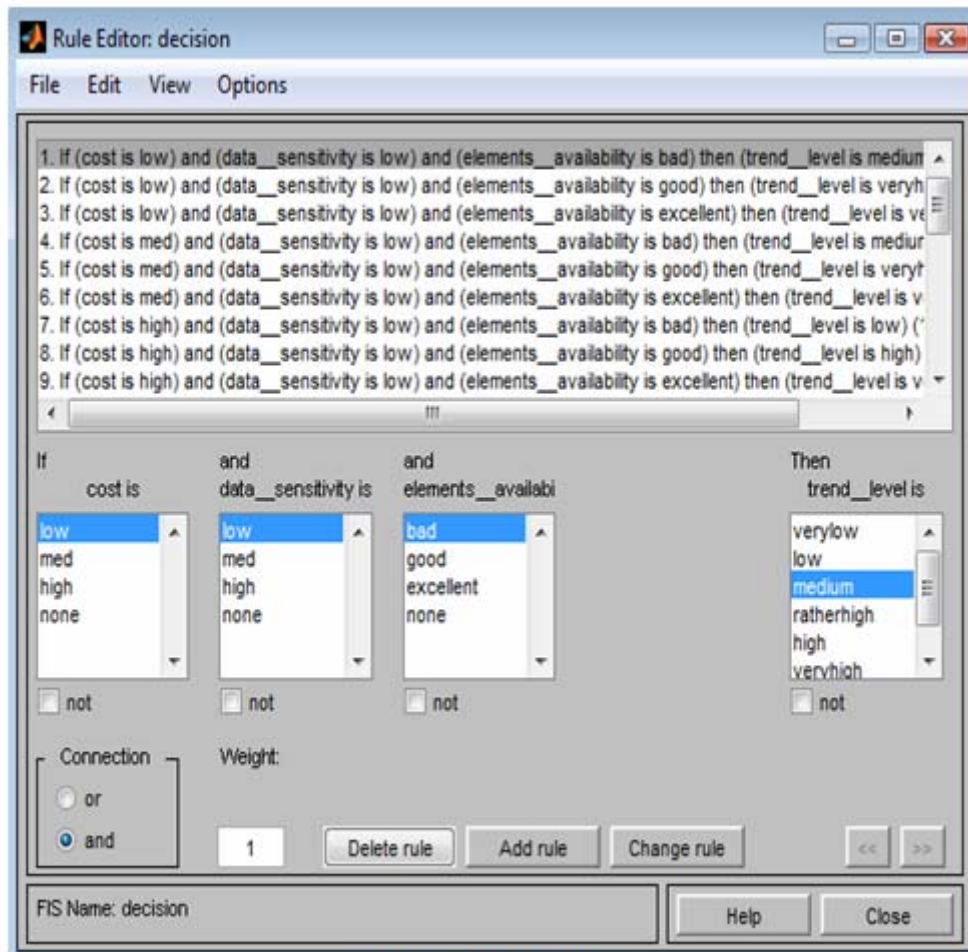


Fig. 6 Rules Editor

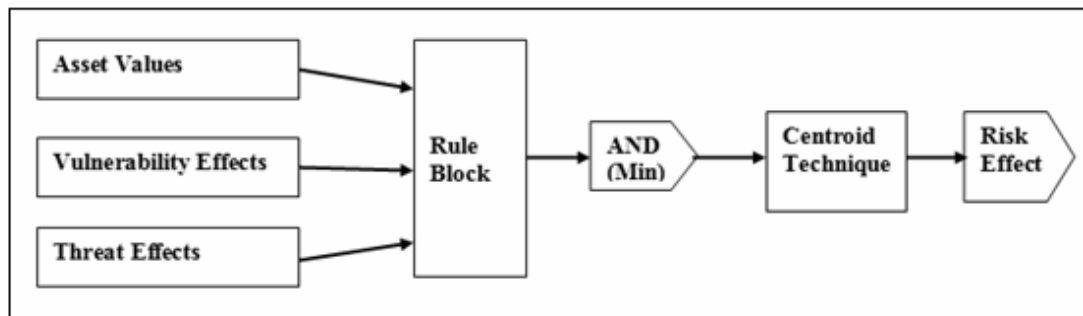


Fig. 7 Architecture of FEMRA



GENERATION OF MPSK SIGNAL USING LOGIC CIRCUITS

Mohammed Kasim Al-Haddad
College of Engineering
Baghdad University

ABSTRACT:

The traditional technique of generating MPSK signals is basically to use IQ modulator that involves analog processing like multiplication and addition where inaccuracies may exist and would lead to imbalance problems that affects the output modulated signal and hence the overall performance of the system. In this paper, a simple method is presented for generating the MPSK using logic circuits that basically generated M-carrier signals each carrier of different equally spaced phase shift. Then these carriers are time multiplexed, according to the data symbols, into the output modulated signal.

الخلاصة:

التقنيات التقليدية لتوليد إشارة MPSK هي أساساً تستخدم مضمن IQ الذي يحوي على عمليات تناظرية مثل الضرب والجمع حيث توجد عدم الدقة مما يؤدي الى مشاكل عدم التوازن التي تؤثر على إشارة الاخراج المضمنة وبالتالي على الاداء الكلي للمنظومة. في هذا البحث تم تقديم طريقة مبسطة لتوليد إشارة MPSK باستعمال دوائر منطقية حيث أساساً تولد عدد M من الاشارات الحاملة كل واحدة بنزحيف طور مختلف وموزعة بالتساوي. ثم يتم انتقاء احدى هذه الاشارات الحاملة حسب رموز البيانات لتتولد الاشارة المحملة.

INTRODUCTION

Phase-Shift Keying is one of the basic digital modulation schemes in which the digital data are modulated into discrete equally spaced phase shift values of the carrier signal. The number of these discrete phase shift values represents the number of levels of the PSK modulation that is generally referred to as MPSK or M-ary PSK. For the two special cases where $M=2$ and $M=4$, the modulation is referred to as Binary PSK (BPSK) and Quadrature PSK (QPSK) respectively. For higher values of M it is referred to as 8PSK, 16PSK, and so on.

In practice BPSK and QPSK are much widely used than 8PSK and 16PSK because the complexity of the system is much higher and since basically, the M-ary PSK and the M-ary QAM have similar spectral bandwidth and system complexity, and the fact that the performance of the QAM modulation is better in terms of probability of error for the same average transmitted signal power, the QAM modulation is preferred and more widely used than MPSK. On the other hand, one advantage in favor of the MPSK over the QAM is that the MPSK has constant envelope while the QAM does not have constant envelope. Therefore the superior performance of the M-ary QAM can be realized only if the channel is free from nonlinearities.

MPSK and QAM modulations are basically implemented using IQ modulator. Imbalance in the I and Q branches is a common problem in the IQ modulator and various techniques were introduced to overcome this problem. In-phase and quadrature amplitudes and phase imbalances are caused by the analog components of the modulator [1].

Cho et al. [1] provided an expression for the probability of symbol error of MPSK-OFDM signal with IQ imbalance over AWGN channel in terms of 2-D Gaussian Q-function, the formula obtained was verified by simulation results. Park et al. [2] worked on the symbol-error probability (SEP) of MPSK signals in the situation of phase error, quadrature error and in-phase-quadrature (I-Q) gain mismatch, in the presence of AWGN and fading channel using Moment Generating Function (MGF) approach. No counter measures were provided both [1] and [2]. Schuchert et al. [3] presented a simulation of an adaptive equalizer applied to OFDM based Digital Video Broadcast-Terrestrial (DVB-T) system. The

GENERATION OF MPSK SIGNAL USING LOGIC CIRCUITS

equalization process is applied to each subcarrier of the OFDM and the coefficients are adapted using data aided training sequence. The equalizer corrects both the channel distortion and IQ imbalance. Nemer et al. [4] presented an algorithm for IQ balancing based on a blind estimation of the magnitude and phase imbalances from the correlation functions of the received I and Q channels without the need of training sequence. The algorithm is further simplified by approximation to eliminate the division operations and reduce the number of multiplication operations and to put it in the form of two cascaded iterative feedback schemes, the first for the magnitude correction and the second for the phase correction. Simulation was applied to DVB signal with QPSK, 8PSK and 16-QAM constellations. Liu [5] presented a study on the IQ imbalance at both the transmitter and the receiver of OFDM systems. A time domain self-calibrating of IQ imbalance estimator for the transmitter is suggested that estimated the amplitude and phase using a training sequence. At the receiver, the estimator of the amplitude and phase imbalance is based on correlation equation of the FFT output of the receiver. The receiver estimator does not rely on training sequence. The performance is evaluated using simulation against AWGN and multipath Rayleigh fading channel.

IQ IMBALANCE

Although there are different formulas of expressing the amplitude and phase imbalance in quadrature modulation but actually these formulas are basically the same and the difference is only as a matter of convenience in choosing the proper mathematical expression. One of these formulas for expressing the amplitude and phase imbalance in a general quadrature modulation (MPSK or QAM) is [4]

$$\begin{bmatrix} I' \\ Q' \end{bmatrix} = \begin{bmatrix} 1+\varepsilon & 0 \\ 0 & 1-\varepsilon \end{bmatrix} \begin{bmatrix} \cos(\Delta\phi/2) & -\sin(\Delta\phi/2) \\ -\sin(\Delta\phi/2) & \cos(\Delta\phi/2) \end{bmatrix} \begin{bmatrix} I \\ Q \end{bmatrix} \quad (1)$$

Where I' and Q' are imbalanced in-phase and quadrature-phase components of the modulated signal, and I and Q are the balanced in-phase and quadrature-phase components, and ε and $\Delta\phi$ are the amplitude and phase imbalance factors respectively. Equation (1) can be expressed without the matrix form as

$$I' = (1+\varepsilon)[\cos(\Delta\phi/2)I - \sin(\Delta\phi/2)Q] \quad (2a)$$



$$Q' = (1 - \varepsilon) [\cos(\Delta\phi/2)Q - \sin(\Delta\phi/2)I] \quad (2b)$$

It should be noted that ε and $\Delta\phi$ are not time dependent factors although they are in general frequency dependent factors [6].

An expression for a multilevel PSK signal can be represented in any of these forms

$$s(t) = \text{Re}[Ae^{j2\pi m/M} e^{j2\pi f_c t}] \quad (3a)$$

$$s(t) = A \cos(2\pi f_c t + 2\pi m/M) \quad (3b)$$

$$s(t) = A [\cos(2\pi m/M) \cos(2\pi f_c t) - \sin(2\pi m/M) \sin(2\pi f_c t)] \quad (3c)$$

$m=0, 2, \dots, M-1$

Where A is the amplitude, f_c is the carrier frequency, $\theta_m = 2\pi m/M$ are the M possible phase shifts of the carrier that convey the transmitted information, and M is a power of 2. $s(t)$ can be further reduced in terms of in-phase and quadrature-phase components to become

$$s(t) = A[I(m)\cos(2\pi f_c t) + Q(m)\sin(2\pi f_c t)] \quad (4)$$

where

$$I(m) = \cos(2\pi m/M) \quad (5a)$$

$$Q(m) = -\sin(2\pi m/M) \quad (5b)$$

In case of imbalance the values of I and Q of eq (5) can be used in eq (1) to get I' and Q' for the imbalanced MPSK signal as

$$I' = (1 + \varepsilon) \cos(2\pi m/M + \Delta\phi/2) \quad (6a)$$

$$Q' = (\varepsilon - 1) \sin(2\pi m/M + \Delta\phi/2) \quad (6b)$$

It is clear that if ε and $\Delta\phi$ are equal to zero, eq (6) reduces to (5)

It is common to represent the digital quadrature modulated signals by their signal space diagram. For the MPSK signals the signal space diagram is as shown in Fig. 1

It is clear from these diagrams that the possible symbol values are located on a circle whose radius represents the amplitude of the modulated signal A . This is expected since the transmitted information is represented by phase shifts only. Therefore, it is possible to assume that the MPSK signal has a unity amplitude for simplicity without any loss of generality i.e. $A=1$. In case of imbalance the effect is reflected on the constellation as shown in Fig. 2

Figure 3 shows a typical IQ modulator where the carrier signal and its quadrature each are multiplied by an appropriate weight according to the modulating symbols and summing the results. The imbalance effect is usually produced due to inaccuracies in the analog blocks of this modulator which are:

- 1- The digital to analog converter (DAC)
- 2- The two multipliers
- 3- The summator
- 4- The -90° phase shifter

The resulting imbalance will affect the position of the transmitted symbols on the signal space diagram and this would lead to increase of probability of detection error.

In this paper a different technique is used to generate the MPSK signal using simple logic circuits to eliminate the need of analog circuits in the MPSK modulator. This way it is possible to avoid inaccuracies that causing a distorted signal space diagram.

THEORETICAL BACKGROUND

It is known from elementary mathematics that the n -order equation

$$z^n = 1 \quad (7)$$

has n complex roots, and these roots are given by

$$z_i = e^{j2\pi(i-1)/n}, \quad i=1, 2, \dots, n \quad (8)$$

and if $n=M=2^k$ i.e. M is a power of 2, the roots of the equation

$$z^M = 1 \quad (9)$$

can be found by repeated square rooting of 1. This can be expressed mathematically in this way

$$z^M = z^{2^k} = z^{(2)^{2^{(k-1)}}} = (z^{2^{(k-1)}})^2 = 1 \quad (10)$$

If we make the change of variables

$$z_1 = z^{2^{(k-1)}} \quad (11)$$

Equation (10) will be reduced to

$$z_1^2 = 1 \quad (12)$$

which is a second degree equation that has two roots. Before proceeding, it is useful to refer to the solution of the complex equation given by

$$z^2 = z_0 \quad (13)$$

where z_0 is a complex number. The solution of eq (13) is given by

$$z = \pm \sqrt{|z_0|} e^{j\theta/2} \quad (14a)$$

Where $|z_0|$ and θ are the magnitude and angle of z_0 . Since the minus sign means a shift of angle of π radians, it is possible to write the roots in the form

$$z = \sqrt{|z_0|} e^{j\theta/2}, z = \sqrt{|z_0|} e^{j(\theta/2+\pi)} \quad (14b)$$

Now, using the result of eq (14b) and the fact that $z_0=1$ in eq (10), it is possible to write the roots of eq (12) as

$$z_{11} = 1 = e^{j0}, z_{12} = -1 = e^{j\pi} \quad (15)$$

Here, the first index represents the step of order reduction and the second index is the root index of that step. Following the same procedure, we will find that

$$z_2^2 = z_1 \quad (16)$$

Equation (16) is actually two equations of the second degree because z_1 has two values (z_{11} and z_{12}), therefore, it will give us 4 roots (2 for each equation). Using the results of eq (15) and eq (14b), the roots of eq (16) will be

$$z_{21} = e^{j0}, z_{22} = e^{j\pi/2}, z_{23} = e^{j\pi}, z_{24} = e^{j3\pi/2}$$

Since each step gives twice as many roots as the previous step, repeating this procedure for k steps will result in 2^k roots which are the desired roots of (9). These roots can be generally expressed as

$$z_{km} = e^{j2\pi(m-1)/M} \quad (17)$$

GENERATION OF MPSK SIGNAL USING LOGIC CIRCUITS

$m=1, 2, \dots, M$

Now, the similarity can be seen between the result of eq (17) and the general expression of the MPSK signal in (1c). Locating the roots given by eq (17) on the complex plane will make the same signal space diagram shown in Fig. 1.

In words, eq (17) is telling us that repeated square rooting of unity yields M complex phasors of M -level MPSK signal. The intention of this paper is to realize the root generation algorithm of unity described above by hardware circuits as will be explained in the next section.

GENERATION OF M-PHASE SHIFTS CARRIERS

Assuming that the amplitude is unity, the square rooting operation is basically a phase division by 2. This can be accomplished using the flip-flop (FF) because the FF does not only divide the frequency by 2, also the phase is divided by 2 as will be explained shortly.

For the purpose of explanation, the generation of 8-level PSK is demonstrated now. The circuit is shown in Fig. 4 where a high frequency clock with frequency f_0 is applied to a JK-FF, with the J and K inputs are connected to logic 1 so that the FF works as a T-FF. The outputs Q and Q' (where Q' is the complement of Q) are denoted as Q_{11} and Q_{12} and used as clocks to a second stage two FF's with outputs Q_{21} , Q_{22} , Q_{23} and Q_{24} , notice the similarity between subscripts notation of the outputs and the subscripts notation of the roots in the previous section, where the first subscripts denotes the stage and the second denotes the position of the output in that stage. The waveforms of the circuit are illustrated in Fig. 5.

Now, assuming that all FF's are initially set to low and that the FF's are negative edge triggered, then the outputs Q_{11} and Q_{12} will change at every high-to-low transition of the high frequency clock, with Q_{12} as the complement of Q_{11} . Now the FF₁₁ with Q_{11} as input will have its outputs Q_{21} and Q_{23} change at the high-to-low transition of Q_{11} with Q_{23} as the complement of Q_{21} , at the same instance FF₁₂ (with input Q_{12}) will have its outputs Q_{22} and Q_{24} undergo no change because its input Q_{12} is making a low-to-high transition. After a half cycle of Q_{11} and Q_{12} the situation is reversed, Q_{11} will have a low-to-high transition at clock input, so no change in Q_{21} and Q_{23} while Q_{12} will have a high-to-low transition so the outputs Q_{22} and Q_{24} will change. Proceeding



in the same manner of analysis, the outputs of higher stages can be worked out as shown in Fig. 5. This arrangement of FF's is so much like the ripple counter except that the two outputs of each FF are used to derive two other FF's. This makes the circuit grows like a binary tree. Because of this similarity, the circuit will be referred to as the Multi-Phase Ripple Counter and denoted to as MPRC throughout this paper.

Assuming that the clock frequency is f_0 , and looking at the outputs Q_{11} and Q_{12} , it can be seen that they have the same frequency $f_1=f_0/2$ and the two outputs are 180° out of phase. While Q_{21} , Q_{22} , Q_{23} and Q_{24} , have the same frequency $f_2=f_1/2=f_0/4$ with $1/4$ cycle time phase shift between each other which is equivalent to 90° phase shift, and for stage 3 $f_3=f_2/2=f_0/8$ with $1/8$ cycle time phase shift.

This can be generalized by expressing the frequency and phase shift of waveforms of each stage by

$$f_n = \frac{f_0}{2^n} \quad (18)$$

$$T_{shift} = \frac{T_n}{2^n} \quad (19)$$

$$\theta_{shift} = \frac{2\pi}{2^n} \quad (20)$$

Where f_n and T_n are the frequency and the cycle time of the outputs of the n^{th} stage, and T_{shift} and θ_{shift} are the lowest time and phase shift between any two different output signals. Notice that all the possible phase shifts between any two output signals can be expressed as a multiple of θ_{shift} , in other words, if we take one signal S_0 as a reference signal with zero phase shift $\theta_0=0$, the phases of the signals of the n^{th} stage can be expressed as

$$\theta_m = (m-1) \frac{2\pi}{M} \quad (21)$$

Where, $M=2^n$ and $m=1, 2, 3, \dots, 2^n$

Which is the exact result required to be achieved

PROPOSED SYSTEM

Now to produce the MPSK signal, the generated waveforms can be multiplexed to one output by the data and the multiplexer output is filtered to be converted into sinusoidal wave. The filtering stage

can be made in the power stage so that high efficiency class D amplifiers particularly current switching or current mode class D amplifiers (CMCD) [8] can be used in the transmitter since such modulator is suitable for constant amplitude modulations. Figure 6 shows a block diagram for the proposed MPSK modulator, where a high frequency clock of frequency f_0 is applied to the MPRC to generate M carriers each with frequency f_0/M and having phase shifts given by eq. (21). These carriers are then applied to an M-lines multiplexer, the select lines of the multiplexer are controlled by the modulating data so that each data code selects one carrier of a particular phase. The fact that these carriers have a frequency value equal to f_0/M and the value of f_0 is already limited by the implementation technology this means that the carrier frequency may not be chosen as desired, in such case, a heterodyne configuration of the modulator where a mixer stage can be used to adjust the carrier frequency as required.

IMPLEMENTATION OF TESTING AND MEASUREMENT SYSTEM

This technique is introduced as an alternative to the IQ modulator to generate MPSK signal to eliminate the IQ imbalance. Regarding the amplitude, the digital multiplexing of the different carriers into one output ensures the elimination of the imbalance in the amplitude. Regarding the phase, the different values of propagation delay of each FF can introduce phase imbalance because each carrier has a different path and hence may encounter a different delay.

An experimental circuit was built using TTL components to practically produce an 8-PSK signal, the circuit schematic is shown in Fig. 7. The IC of 7476 which is a dual JK FF was used to implement the MPRC and the 74151 was used as the 8-to-1 multiplexer. To simulate the data, 3 stages of the binary counter 7493 was used to down scale the frequency of one of the carriers to lower frequency to simulate the data rate, this ensures that the carrier frequency is an integer multiple of the data rate instead of having a different independent clock for the data. The output of the multiplexer was applied to a BPF and compared to a reference signal of the same frequency and the x-y plot of the oscilloscope was viewed as shown in Fig. 8 where, the 8 phase patterns can be seen as 8 different ellipses. This

measurement was made at carrier frequency equals to 160kHz.

To measure the phase error produced due to the different propagation delay, the oscilloscope observation is not suitable because the measurement is taken from the time scale which is considered as an analog measure that may not be an accurately reliable measurement. To make a digital measurement of time, the output of the multiplexer and one of its inputs (considered as a reference signal) are fed to a computer through the parallel port interface. An MS DOS based Turbo C program was run in MS DOS real mode to read these two signals and measure the time difference. This program is run under MS DOS operating system (OS) not under Windows OS because Windows is a multitask OS and it is not a convenient platform for timing critical programs because the processor time is shared among multitasks including the user's program which in turn would affect the time measurement task of the program.

The time measuring Program was tested for the highest sampling frequency possible (which is limited by the speed of the PC), the sampling frequency was found approximately 800 ksample/s. Although, this value of the sampling frequency seems rather high, but it is actually not. Since we are trying to measure time, we need to consider the minimum timing interval which is 1/8 of a cycle and to assign say 20 samples for 1/8 of a cycle, the frequency of the carrier should be

$$(1/f_c) \times (1/8) = 20 \times 1/f_s$$

$$f_c = f_s / (8 \times 20) = 800 / (8 \times 20) = 5 \text{ kHz}$$

This means that the clock frequency should be $f_{\text{clock}} = 8 \times 5 = 40 \text{ kHz}$. Although, the 5 kHz value as a carrier frequency is not practical, but it was chosen due to the limitations imposed by what was available of measurement tools that is the MS DOS based PC.

The basic idea of measuring the phase difference between the two signals is

- 1- Detect two successive low-to-high bit transitions of the first signal and calculate the number of samples in between as the time of one cycle.
- 2- Detect a low-to-high transition of the first signal and a low-to-high of the second

GENERATION OF MPSK SIGNAL USING LOGIC CIRCUITS

signal and calculate the number of samples in between as the time shift.

- 3- Calculate phase = (time shift / cycle time) \times 360

After measuring the phase difference between the output signal and the reference signal, the phase error was calculated as RMS value and the results were as in the table below

As can be seen from the above table that the phase deviation from ideal phase values is rather low, two important factors need to be considered when evaluating these results. The first factor is that the carrier frequency is low and it has been mentioned earlier that the imbalance parameters are in general frequency dependent and for higher frequency values it is expected that the situation is worse but on the other hand the fact that the measurement time is being quantized by the sampling period leads to the generation of certain amount of error that is added to the actual phase imbalance introduced by the circuit. The second factor is that the source of phase imbalance produced by this circuit is due to the different paths that different carriers take and hence different propagation delays are encountered. Theoretically if all paths have equal propagation delay, no phase imbalance will be introduced. In practical situation this is not the case, but the amount of difference in the propagation delays is an implementation technology dependent and the circuit was implemented using TTL technology (which is rather old technology) because of its availability at hand. It is expected that modern implementation technology will have better performance than the TTL technology, like [9]:

- 1- Dynamic Current Mode Logic (DyCML)
- 2- Gate-Diffusion Input (GDI)
- 3- Race Logic Architecture (RALA)

CONCLUSION

In this paper a new technique for generating MPSK signal is presented in which no analog components are used to generate the modulating phase shifts and hence eliminating or reducing the amplitude and phase imbalance. A practical circuit was built using TTL components to generate an 8PSK signal and the results was presented as the 8 ellipses for 8 phase differences, also the time measurements was made for lower frequencies to measure the phase imbalance.



REFERENCES

- 1- Kyongkuk Cho, Jaeyoon Lee, Dongweon Yoon, Sang Kyu Park, and Sanggoo Kim
“The Effect of I/Q Imbalances in OFDM Systems with MPSK Modulation over AWGN Channel,”
The 11th IEEE International Conference on Communications Systems (ICCS) 2008
- 2- Seungkeun Park and Sung Ho Cho “SEP Performance of Coherent MPSK Over Fading Channels in the Presence of Phase/Quadrature Error and I-Q Gain Mismatch” IEEE Transactions On Communications, Vol. 53, No. 7, July 2005.
- 3- Andreas Schuchert and Ralph Hasholzner “A Novel IQ Imbalance Compensation Scheme For The Reception of OFDM Signals” IEEE Transactions on Consumer Electronics, Vol. 47, No. 3, AUGUST 2001.
- 4- Elias Nemer and Ahmed Said “An Iterative Feedback Algorithm for Correcting the I/Q Imbalance in DVB-S Receivers”. ACTA Press Proceedings on Communications Systems and Networks 2004, Spain.
- 5- Chia-Horng Liu “On the Study of End-to-End IQ Imbalance Problem in OFDM Systems” IEEE 68th Vehicular Technology Conference, 2008, Canada.
- 6- S. Mutha, P. Roblin, D. Chaillot, Xi Yang, Jiwoo Kim, J. Strahler, R. Rojas, J. Volakis, “Technique for Joint Balancing of IQ Modulator-Demodulator Chains in Wireless Transmitters” IEEE MTT-S International Microwave Symposium Digest, 2009. Boston, MA, pp 221 – 224.
- 7- Jack Smith, *Modern Communication Circuits*, McGraw-Hill Series in Electrical Engineering, 1986.
- 8- Andrei Grebennikov and Nathan O. Sokal *Switchmode RF Power Amplifiers*, Elsevier Communications Engineering Series, 2007.
- 9- G. Privitera and Francesco Pessolano “Analysis of High-Speed Logic Families” Power and Timing Modeling, Optimization and Simulation, Proceedings of 13th International Workshop, PATMOS 2003, Italy.

Table (1) The measured RMS phase error

Ideal Phase difference in degrees	Respective RMS of phase error in degrees
0	0.00
$1/8 \times 360$	0.57
$2/8 \times 360$	1.14
$3/8 \times 360$	0.58
$4/8 \times 360$	1.13
$5/8 \times 360$	0.57
$6/8 \times 360$	1.14
$7/8 \times 360$	0.57

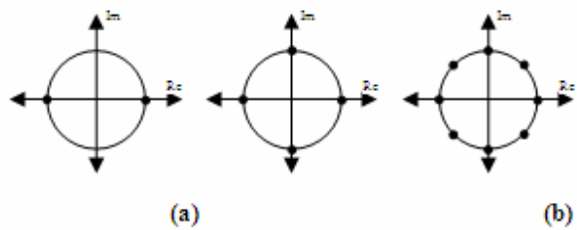


Fig. 1 Signal space diagrams for MPSK signals with (a) $M=2$, (b) $M=4$ and (c) $M=8$.

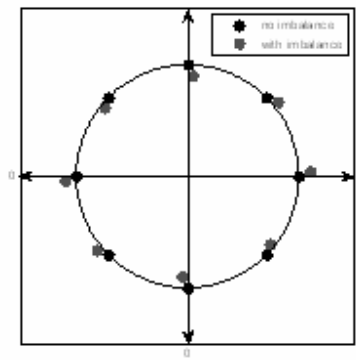


Fig. 2 8PSK constellation with imbalance ($\varepsilon=0.1$, $\Delta\phi=5^\circ$) without and imbalance.

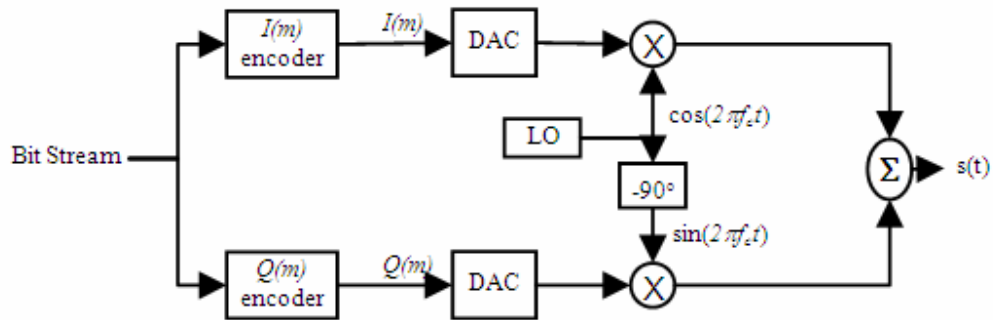


Fig. 3 A typical MPSK modulator.

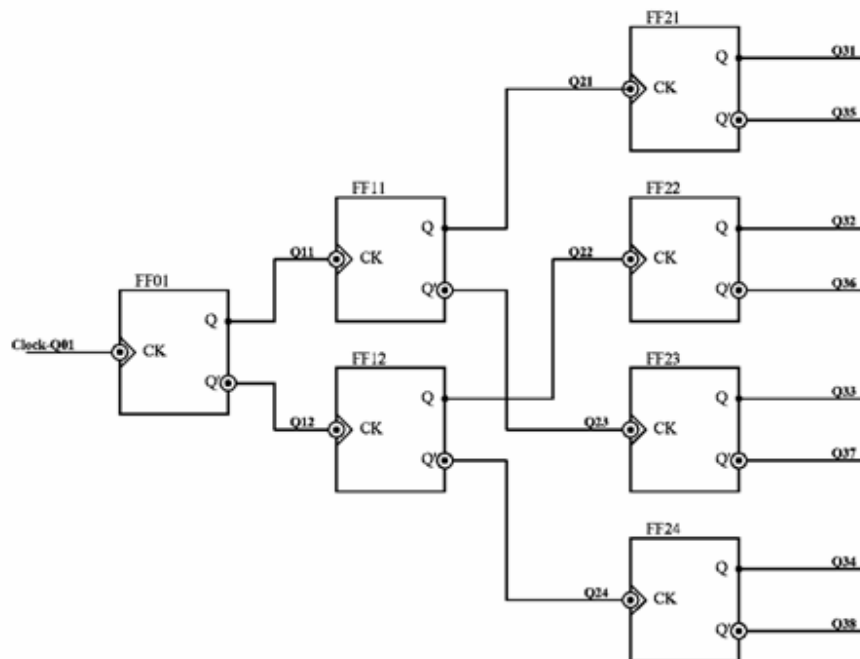


Fig. 4 Multi phase ripple counter.

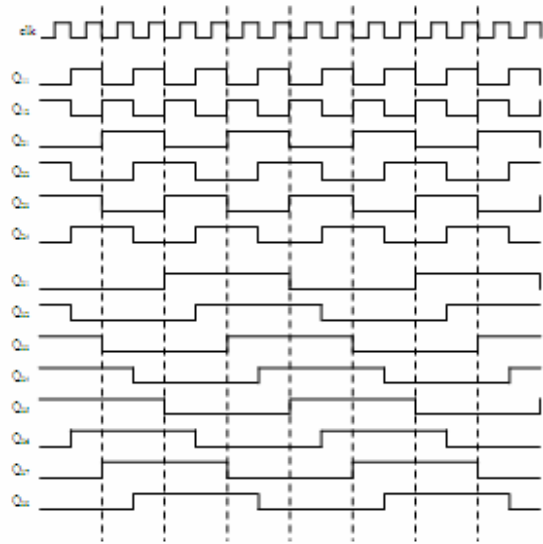


Fig. 5 The waveforms generated by the MPRC

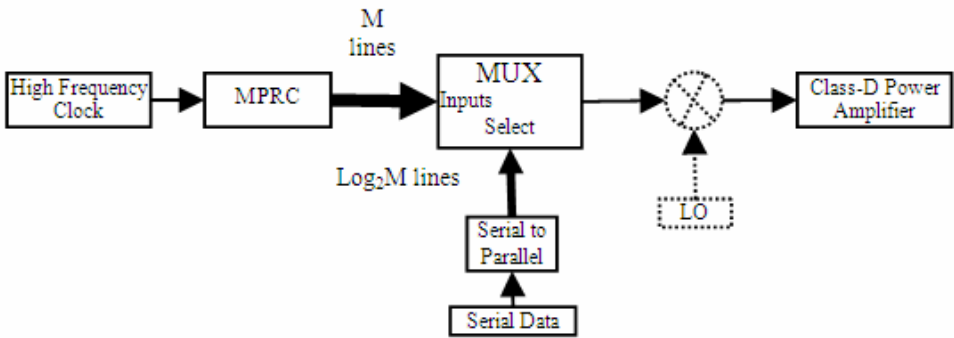


Fig. 6 The proposed system for MPSK transmitter

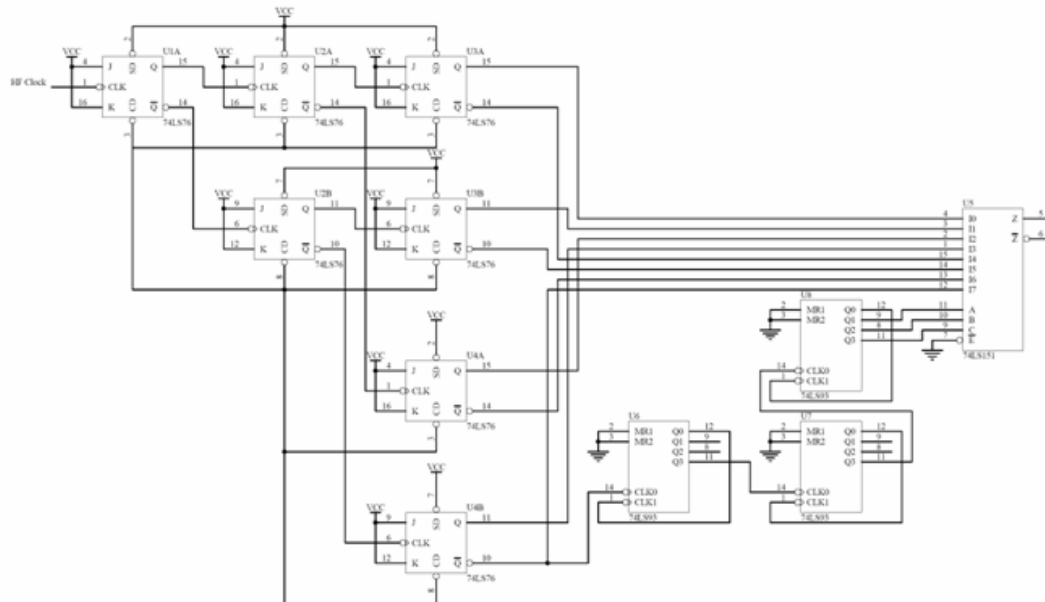


Fig. 7 The test circuit for generating the 8PSK signal.

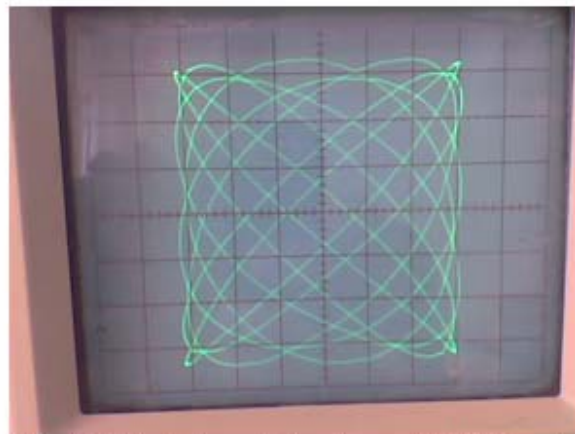


Fig. 8 Eight ellipses of the phases of 8PSK signal.



FACE IDENTIFICATION USING BACK-PROPAGATION ADAPTIVE MULTIWAVENET

Prof. Dr. Waleed Ameen Mahmoud

University of Baghdad/ College of Engineering
Electrical Engineering Department

Ali Ibrahim Abbas

University of Baghdad/ College of Engineering
Electrical Engineering Department

Asst. Prof. Nuha Abdul Sahib Alwan

University of Baghdad/ College of Engineering
Computer Engineering Department

Abstract

Face Identification is an important research topic in the field of computer vision and pattern recognition and has become a very active research area in recent decades. Recently multiwavelet-based neural networks (multiwavenets) have been used for function approximation and recognition, but to our best knowledge it has not been used for face Identification. This paper presents a novel approach for the Identification of human faces using Back-Propagation Adaptive Multiwavenet. The proposed multiwavenet has a structure similar to a multi-layer perceptron (MLP) neural network with three layers, but the activation function of hidden layer is replaced with multiscaling functions. In experiments performed on the ORL face database it achieved a recognition rate of 97.75% in the presence of facial expression, lighting and pose variations. Results are compared with its wavelet-based counterpart where it obtained a recognition rate of 10.4%. The proposed multiwavenet demonstrated very good recognition rate in the presence of variations in facial expression, lighting and pose and outperformed its wavelet-based counterpart.

(Back-Propagation Adaptive Multiwavenet)

(MLP)

ORL

%97.75

.%10.4

Keywords: Face Identification, multiwavelet neural network, Back-Propagation Adaptive Multiwavenet

1. INTRODUCTION

Over the last decade, face recognition has become a popular area of research in computer vision. A general statement of the face recognition problem can be formulated as follows: Given still or video images of a scene, identify or verify one or more persons in the scene using a stored database of faces. A survey of face recognition techniques has been given by (Zhao W., et al., 2003).

In general, face recognition techniques can be divided into two groups based on the face representation they use:

- Appearance-based, which uses holistic texture features and is applied to either whole-face or specific regions in a face image;
- Feature-based, which uses geometric facial features (mouth, eyes, brows, cheeks etc.) and geometric relationships between them.

Among various solutions to the problem (Turk M., et al., 1991) the most successful seems to be appearance-based approaches, which generally operate directly on images or appearances of face objects and process the image as two-dimensional patterns. Most effort in the literature have focused mainly on developing feature extraction methods (Zhao W., et al., 2003), (Zhao W., et al., 1997), (Deniz O., et al., 2003) and employing powerful classifiers such as probabilistic (Moghaddam B., 2002), Hidden Markov models (HMMs) (Othman H., et al., 2003) neural networks (NNs) (Er M.J., et al., 2003), (Er M.J., et al., 2005) and support vector machine (SVM) (Lee K., et al., 2002).

The use of neural networks for face recognition has been addressed in (Pang S., et al., 2005), (Zhang B., et al., 2004), (Fan X., et al., 2005), (Lu X., et al., 2003). Recently, (Li G., et al., 2006) suggested the use of a non-convergent chaotic neural network to recognize human faces. (Lu K., et al., 2006) suggested a semi-supervised learning method that uses support vector machines for face recognition. (Zhou W., et al., 2006) suggested using a radial basis function neural network that is integrated with a non-negative matrix factorization to recognize faces. (Huang L.L., et al., 2006) proposed using two neural networks whose outputs are combined to make a final decision on classifying a face. (Park C., et al., 2006) used a momentum back propagation neural network for face and speech verification.

Back Propagation Wavenet (BPW) is an artificial neural network (ANN) that is integrated

with wavelet techniques and has been used successfully in many fields. Instead of conventional nonlinear sigmoid transfer functions, the transfer function of the nodes in a wavelet neural network is wavelet bases. Because wavelet bases are localized in time and frequency, the ability of a BPW in mapping complicated nonlinear functions is enhanced considerably (Yang X., et al., 2009).

(Shen Y., et al., 2004) used BPW for object recognition. (Ensafi A.A., et al., 2007) applied BPW for the determination of sulfide and thiocyanate in real samples such as tap, waste and river waters with satisfactory results. to improve the detection rate for anomaly state and reduce the false positive rate for normal state in the network anomaly detection. (Liu L., et al., 2009) proposed a novel method based on BPW trained by Modified Quantum-behaved Particle Swarm Optimization (MQPSO) algorithm. (Long-yun X., et al., 2008) used BPW for gear faults diagnosis. (Zhao Y.Z., et al., 2009) used BPW for learning the wear out pattern of the milling machine cutters to predict their remaining useful life. (Bin Z., et al., 2010) applied BPW to solve the problem of tunnel surrounding rock deformation prediction.

As an extension of wavelets, a multiwavelet can preserve all the advantages the wavelet has. Furthermore, it can simultaneously have several properties very useful in practical applications such as orthogonality, regularity, symmetry, and compact support, which is impossible for a scalar wavelet. Therefore, the networks using the dilations and translations of a multiscaling function as node functions have better performances which are worth investigating (Jiao L.C., et al. 2001). Based on the considerations above, a model of multiwavelet-based neural network for face identification is used in this paper.

Section 2 provides an introduction of the Multiwavenet. Section 3 presents a face identification system based on a back-propagation multiwavenet classifier. Section 4 presents experimental results. Conclusions are presented in Section 5.

2. MULTIWAVENET

Suppose a multiplicity- r multiscaling function

$\phi(t) = [\phi^1(t), \phi^2(t), \dots, \phi^r(t)]^T$ satisfies a dilation equation



$$\phi(t) = \sum_{k \in \mathbb{Z}} p_k \phi(2t - k) \quad (1)$$

and the dilations and translations of $\phi^l(t)$ s, denoted by $\phi_{j,k}^l(t) = 2^{j/2} \phi_{j,k}^l(2^j t - k)$, $l = 1, \dots, r$, $k \in \mathbb{Z}$, span the scale space V_j , $j \in \mathbb{Z}$.

We are interested in the case of orthogonal multiscaling functions. In that case, $\{\phi_{j,k}^l(t) | l = 1, \dots, r, k \in \mathbb{Z}\}$ form an orthonormal basis of V_j , and the associated multiwavelet $\psi(t) = [\psi^1(t), \psi^2(t), \dots, \psi^r(t)]^T$ make $\psi_{j,k}^l(t) = 2^{j/2} \psi_{j,k}^l(2^j t - k)$, $l = 1, \dots, r, k \in \mathbb{Z}$, form an orthonormal basis of the orthogonal complementary subspace W_j of V_j in V_{j+1} . From the theory of multiresolution analysis, we know that $\bigcup_{j \in \mathbb{Z}} V_j = L^2(\mathbb{R})$ and hence, for any $f \in L^2(\mathbb{R})$, there exists a natural number J_0 , such that $\|f - f_J\|_2 < \varepsilon$, $J > J_0$ where $\|\bullet\|_2$ is L^2 norm, ε is an arbitrary positive number, and $f_J \in V_J$

$$f_J = \sum_{l=1}^r \sum_{k \in \mathbb{Z}} \langle f, \phi_{J,k}^l \rangle \phi_{J,k}^l(t). \quad (2)$$

From the viewpoint of neural networks, f_J can be learned by a neural network, which is called multiwavelet neural network (multiwavenet) because of its connection with the multiwavelet theory though the node functions used are the associated multiscaling functions (Jiao L.C., et al. 2001).

3. THE PROPOSED FACE IDENTIFICATION SYSTEM

The general structure of the proposed face identification system is shown in **Fig. 1**.

Function of each block is clarified below:

- **Preprocessing:** Locating faces in image and extracting the face part only. This is done manually.
- **Normalization:** Histogram equalization of images to reduce the effect of lightning source amplitude's variations.
- **Feature Extraction:** Down sample the image to a low resolution using a bicubic interpolation method and put the result in a one-dimensional feature vector.
- **Classifier:** Multiwavenet classifier is used. After the training is done, the parameters

of the multiwavenet classifier, namely weights, translations and dilations are stored and are used in the identification stage when the classifier works in simulation mode.

The processing in both training and identification stages is similar except for the classifier, which works in training mode in the training stage and in simulation mode in the identification stage.

In this section, a classifier for the face identification system is proposed. Each output of the multiwavenet classifier corresponds to a class. The position of the output with the highest value determines the class to which the input belongs. For example if there are five classes, five outputs are needed. During the training phase, each data in the training set is presented to the classifier to the classifier along with its desired output, where desired output for an input belonging to class c is an all zero vector with a one in the c th position. When a new input is presented to the classifier, the position of the highest value output determines the class.

The architecture of the proposed Back Propagation Adaptive Multiwavenet (BPAMW) is basically the same as the back propagation neural network, except that the sigmoid function of hidden layer node of the back propagation neural network is replaced with two or more scaling functions of a multiwavelet system. For each distinct individual in the training set, an output is needed and for each output a set of weights is required. A competitive layer is added after the output layer. Function of this layer is to produce the final classification result by choosing the output with the highest value among all outputs as the winner and returning its position as the final classification. The architecture of the BPAMW classifier is shown in **Fig. 2**.

The k th output of the BPAMW classifier before the competitive layer is

$$y_k(U_s) = \sum_{i=1}^M \sum_{L=1}^r w_{iLk} \phi_L \left(\frac{z_{is} - t_i}{\lambda_i} \right) \quad (3)$$

$$k = 1 \dots K, \quad s = 1 \dots P$$

$$z_{is} = \sum_{j=1}^N v_{ji} u_{js}, \quad (4)$$

where M is the number of multiwavelons, r is the multiplicity of the multiscaling function and each multiwavelon has r wavelons, t_i and λ_i are the translation and dilation of i th multiwavelon's scaling functions respectively, ϕ_L is the L 'th scaling function. $U_s = \{u_{1s}, u_{2s}, \dots, u_{Ns}\}$ is the s th input vector of the total P input vectors in the training set, N is the number of elements of each input vector (input dimension), z_{is} is the inner product between the input vector U_s and the i th input weight vector $V_i = \{v_{1i}, v_{2i}, \dots, v_{Ni}\}$ (weights between input nodes and i th multiwavelon), w_{iLk} is the weight between L th wavelon of i th multiwavelon and the k th output, $y_k(U_s)$ is the k th output of the network and there are K nodes in the output layer, K should be equal to the number of individuals in the training database.

(Plonka G., et al. 1998) presented an efficient method for creating multi-scaling functions with given approximation order, regularity, symmetry and short support. In second example of their paper, multi-scaling functions with approximation order 4, compact support (0,2), and symmetry was constructed which will be used in this work. Unlike GHM (Geronimo-Hardin-Massopust) multi-scaling functions, these functions have a closed form expression:

$$\phi_1(u) = \begin{cases} (-2u^3 + 3u^2) & u \in [0,1) \\ (2-u)^2(2u-1) & u \in [1,2] \\ 0 & \text{otherwise} \end{cases} \quad (5)$$

$$\phi_2(u) = \begin{cases} -u^2(3u-3) & u \in [0,1) \\ -(2-u)^2(3u-3) & u \in [1,2] \\ 0 & \text{otherwise} \end{cases} \quad (6)$$

To calculate partial derivatives, the derivative of ϕ_L is also required. Each ϕ_L is composed of two polynomial functions, to obtain the derivative of ϕ_L each polynomial is differentiated as an independent function and results are combined.

$$\frac{d\phi_1(u)}{du} = \begin{cases} -6u(u-1) & u \in [0,1) \\ 6(u-1)(-2+u) & u \in [1,2] \\ 0 & \text{otherwise} \end{cases} \quad (7)$$

$$\frac{d\phi_2(u)}{du} = \begin{cases} -3u(3u-2) & u \in [0,1) \\ -3(3u-4)(-2+u) & u \in [1,2] \\ 0 & \text{otherwise} \end{cases} \quad (8)$$

The output of the competitive layer is

$$c = \arg \max_{k \in \{1 \dots K\}} (y_k) \quad (9)$$

where y_k is the k th output and K is the total number of outputs.

Gradient descent method is used for training of the network parameters. The objective function to be minimized is

$$C_k = \frac{1}{2P} \sum_{s=1}^P (y_k(U_s) - f_k(U_s))^2, \quad k = 1 \dots K \quad (10)$$

where P is the number of training pairs, $y_k(U_s)$ is the k th output of the BPAMW classifier before the competitive layer and $f_k(U_s)$ is the k th desired output. The competitive layer is not included in the training, because it has a fixed function that does not need training and only operates when the classifier is in identification stage where it determines the final classification result.

Batch training mode is used where all training pairs $\{U_s, f_k(U_s)\}$, $s = 1, \dots, P$ should be processed before parameters could be updated. Parameters are modified in the opposite direction of the gradient of C_k . To speed up the convergence rate, momentum term is included in parameter's update.

Let

$$\tau_{is} = \frac{z_{is} - t_i}{\lambda_i}, \quad (11)$$

$$\phi_L(\tau_{is}) = \phi_L\left(\frac{z_{is} - t_i}{\lambda_i}\right), \text{ and} \quad (12)$$

$$e_{sk} = y_k(U_s) - f_k(U_s). \quad (13)$$

Partial derivatives are expressed as follows:



$$\frac{\partial C}{\partial w_{iLk}} = \sum_{s=1}^P e_{sk} \phi_L(\tau_{is}) \quad (14)$$

$$\frac{\partial C}{\partial v_{ji}} = \sum_{s=1}^P \sum_{k=1}^K \sum_{L=1}^r e_{sk} w_{iLk} \frac{\partial \phi_L(\tau_{is})}{\partial \tau_{is}} u_{js} \lambda_i^{-1} \quad (15)$$

$$\frac{\partial C}{\partial t_i} = - \sum_{s=1}^P \sum_{k=1}^K \sum_{L=1}^r e_{sk} w_{iLk} \frac{\partial \phi_L(\tau_{is})}{\partial \tau_{is}} \lambda_i^{-1} \quad (16)$$

$$\frac{\partial C}{\partial \lambda_i} = \sum_{s=1}^P \sum_{k=1}^K \sum_{L=1}^r e_{sk} w_{iLk} \frac{\partial \phi_L(\tau_{is})}{\partial \tau_{is}} \tau_{is} \lambda_i^{-1} \quad (17)$$

Parameters can be updated as follows:
 h = iteration number

$$w_{iLk}^{h+1} = w_{iLk}^h - \eta \frac{\partial C}{\partial w_{iLk}} + \alpha \Delta w_{iLk}^h \quad (18)$$

$$v_{ji}^{h+1} = v_{ji}^h - \eta \frac{\partial C}{\partial v_{ji}} + \alpha \Delta v_{ji}^h \quad (19)$$

$$t_i^{h+1} = t_i^h - \eta \frac{\partial C}{\partial t_i} + \alpha \Delta t_i^h \quad (20)$$

$$\lambda_i^{h+1} = \lambda_i^h - \eta \frac{\partial C}{\partial \lambda_i} + \alpha \Delta \lambda_i^h \quad (21)$$

where $\Delta x^h = x^h - x^{h-1}$.

Parameter initialization has a significant impact on the convergence rate of the BPAMW. A heuristic method for parameter initialization is proposed here. The following equations express the parameter initialization.

$$v_{ji} = \text{rand}() * 4 - 2 \quad (22)$$

for $j = \{1, \dots, N\}, i = \{1, \dots, M\}$

$$w_{iL} = 0 \quad (23)$$

for $i = \{1, \dots, M\}, L = \{1, \dots, r\}$

$$U_{\max} = \max_{s \in \{1, \dots, P\}} (U_s) \quad (24)$$

$$U_{\min} = \min_{s \in \{1, \dots, P\}} (U_s) \quad (25)$$

$$z_{i \max} = V_i^T \cdot U_{\max} \quad (\text{inner product}) \quad (26)$$

$$z_{i \min} = V_i^T \cdot U_{\min} \quad (\text{inner product}) \quad (27)$$

$$\lambda_i = \frac{z_{i \max} - z_{i \min}}{2} \quad (28)$$

$$t_i = \frac{z_{i \max} + z_{i \min}}{2} \quad (29)$$

where $\text{rand}()$ is a function that generates random number in the range (0, 1).

The BPAMW classifier's training is needed to be done only once and after that, it can recognize new and unseen images of the persons in the training set. When operating in the identification mode, the classifier uses the stored parameters from training stage to calculate the outputs. The index of the output with the highest value is the class number of the input that is calculated by the competitive layer.

4. EXPERIMENTAL RESULTS

AT&T "The Database of Faces" (formerly "The ORL Database of Faces") database contains 400 grayscale images of 40 persons. Each person has 10 images, each having a resolution of 92 x 112 and 256 gray levels. For some subjects, the images were taken at different times, varying the lighting, facial expressions (open / closed eyes, smiling / not smiling) and facial details (glasses / no glasses). All the images were taken against a dark homogeneous background with the subjects in an upright, frontal position (with tolerance for some side movement). The first three images from each individual of the database are selected for the test set and the rest of the face images are included in the training set. Therefore, a total of 280 face images are used for training and another 120 face images are used for testing. A sample of the face images are shown in Fig. 3.

Images were resized to size 6*7 and put in a one-dimensional vector, then pixel values were normalized to range (0,1) by dividing each element of the vector by the maximum value of the vector.

For the BPAMW classifier; number of multiwavelons was set to 40, the iteration number was set to 5 and the learning rate was 0.01. The momentum term coefficient was 0.9. Results are

summarized in **Table 1**. **Fig. 4** shows the training performance of the network. An average recognition rate of 97.75% was obtained over ten trials. Each trial involves training and testing. Since training uses the *rand()* function for parameter initialization, the final stored parameters upon convergence may differ slightly. This is why averaging the recognition rate over ten trials is performed to achieve stochastic ensemble averaging.

To compare the performance of the proposed BPAMW classifier with the BPW classifier, the same experiments were performed with the same parameters. Results are summarized in **Table 2**.

Fig. 5 shows the training performance of the network. An average independent recognition rate of 10.4% were obtained over ten trials.

The proposed BPAMW classifier has a very good recognition rate of 97.75% in a very few iterations, which indicates that it has a very good recognition rate when there are variations in the facial expression and limited pose variations. Also the results show that BPAMW classifier is superior to BPW classifier because it achieved a higher recognition rate in the same number of iterations.

5. CONCLUSIONS

In this paper a classifier has been proposed for identification of human faces. The classifier is based on multiwavelet neural network. As an extension of wavelets, a multiwavelet can preserve all the advantages the wavelet has. Furthermore, it can simultaneously have several properties very useful in practical applications such as orthogonality, regularity, symmetry, and compact support, which is impossible for a scalar wavelet. Therefore, the network using the multiwavelet as activation functions has a better performance than the same network with wavelets as activation functions.

Experiments that were performed on AT&T "The Database of Faces" (formerly "The ORL Database of Faces") showed that BPAMW classifier has a very good recognition rate of 97.75% in the presence of facial expression, lighting and pose variations.

REFERENCES

- Bin Z., De-yuan H., and Tao L., "Research on the Application of Wavelet Neural Network in the Surrounding Rock Displacement Prediction," 2nd International Asia Conference on Informatics in Control, Automation and Robotics (CAR 2010), Wuhan, China, pp. 266-269, 6-7 March 2010.
- Deniz O., Castrillfion M., and Hernfiandez M., "Face recognition using independent component analysis and support vector machines", Pattern Recognition letters, vol. 24, pp. 2153-2157, 2003.
- Ensafi A.A., Khayamian T., and Tabaraki R., "Simultaneous Kinetic Determination of Thiocyanate and Sulfide Using Eigenvalue Ranking and Correlation Ranking in Principal Component-Wavelet Neural Network," Talanta, Vol. 71, Issue 5, pp. 2021-2028, March 2007.
- Er M.J., Chen W., and Wu S., "High speed face recognition based on discrete cosine transform and RBF neural network", IEEE Trans. On Neural Network, vol. 16, no.3, pp. 679-691, 2005.
- Er M.J., Wu S., Lu J., and Toh L.H., "face recognition with radial basis function (RBF) neural networks", IEEE Transactions on Neural Networks, vol. 13, no. 3, pp. 697-710, 2003.
- Fan X., and Verma B., "A Comparative Experimental Analysis of Separate and Combined Facial Features for GA-ANN based Technique," Sixth International Conference on Computational Intelligence and Multimedia Applications, pp. 279-284, Aug. 2005.
- Huang L.L., and Shimizu A., "Combining Classifiers for Robust Face Detection," In Lecture Notes in Computer Science, 3972, Springer-Verlag, pp. 116-121, 2006.
- Jiao L.C., Pan J., and Fang Y.W., "Multiwavelet neural networks and its approximation properties," IEEE Transactions on Neural Networks, Vol. 12, Issue 5, pp. 1060-1066, 2001.



- Lee K., Chung Y., and Byun H., "SVM based face verification with feature set of small size", *Electronic letters*, vol. 38, no.15, pp. 787-789, 2002.
- Li G., Zhang J., Wang Y., and Freeman W.J., "Face Recognition Using a Neural Network Simulating Olfactory Systems," In *Lecture Notes in Computer Science*, 3972, Springer-Verlag, pp. 93-97, 2006.
- Liu L., and Liu Y., "MQPSO based on wavelet neural network for network anomaly detection," 5th International Conference on Wireless Communications, Networking and Mobile Computing (WiCom'09), Beijing, China, pp. 1-5, 24-26 Sep. 2009.
- Long-yun X., Zhi-yuan R., and Rui-cheng F., "Gear Faults Diagnosis Based on Wavelet Neural Networks," *Proceedings of IEEE International Conference on Mechatronics and Automation*, Takamatsu, Japan, pp. 452-455, 5-8 Aug. 2008.
- Lu K., He X., and Zhao J., "Semi-supervised Support Vector Learning for Face Recognition," In *Lecture Notes in Computer Science*, 3972, Springer-Verlag, pp. 104-109, 2006.
- Lu X., Wang Y., and Jain A.K., "Combining Classifiers for Face Recognition," *Proceedings of International Conference on Multimedia and Expo (ICME '03)*, Vol. 3, pp. 13-16, 2003.
- Moghaddam B., "Principal manifolds and probabilistic subspaces for visual recognition", *IEEE Transactions on pattern Anal. Machine Intelligence*, vol. 24, no.6, pp. 780-788, 2002.
- Othman H., and Aboulnasr T., "A separable low complexity 2D HMM with application to face recognition", *IEEE Trans. Pattern. Anal. Machie Inell.*, vol. 25, no.10, pp. 1229-1238, 2003.
- Pang S., Kim D., and Bang S.Y., "Face Membership Authentication Using SVM Classification Tree Generated by Membership-Based LLE Data Partition". In *IEEE Transactions on Neural Networks*, Vol. 16, Issue 2, pp. 436-446, 2005.
- Park C., Ki M., Namkung J., and Paik J.K., "Multimodal Priority Verification of Face and Speech Using Momentum Back-Propagation Neural Network," In *Lecture Notes in Computer Science*, 3972, Springer-Verlag, pp. 140-149, 2006.
- Plonka G., and Strela V., "Construction of Multi-Scaling Functions with Approximation and Symmetry," *SIAM Journal on Mathematical Analysis*, Vol. 29, Issue 2, pp. 481-510, March 1998.
- Shen Y., Wang Q., and Yu S., "A Target Recognition of Wavelet Neural Network Based on Relative Moment Features," *Proceedings of the 5th World Congress on Intelligent Control and Automation*, Hangzhou, P.R. China, Vol. 5, pp. 4089-4091, 15-19 June 2004.
- Turk M., and Pentland A., "Eigen faces for face recognition", *Journal cognitive neuroscience*, vol. 3, no.1, 1991.
- Yang X., Kumehara H., and Zhang W., "Back Propagation Wavelet Neural Network Based Prediction of Drill Wear from Thrust Force and Cutting Torque Signals," *Canadian Center of Science and Education (CCSE), Computer and Information Science Journal*, Vol. 2, Issue 3, pp. 75-86, Aug. 2009.
- Zhang B., Zhang H., and Ge S., "Face Recognition by Applying Wavelet Subband Representation and Kernel Associative Memory," In *IEEE Transactions on Neural Networks*, Vol. 15, pp. 166-177, 2004.
- Zhao W., Chellappa R., and Krishnaswamy A., "Discriminant analysis of principal component for face recognition", *IEEE Transactions on Pattern Anal. Machine Intelligence*, vol. 8, 1997.
- Zhao W., Chellappa R., Phillips J., and Rosenfeld A., "Face recognition in still and video images: A literature survey", *ACM Comput Surv* vol. 35, pp. 399-458, 2003.
- Zhao Y.Z., and Li X., "A Dual-Momentum Hybrid Wavelet Neural Net (DM-HWNN): Its Performance Evaluation and Application," 7th IEEE International Conference on Industrial Informatics (INDIN 2009), Cardiff, Wales, UK, pp. 325-330, 23-26 June 2009.
- Zhou W., Pu X., and Zheng Z., "Parts-Based Holistic Face Recognition with RBF Neural

Networks,” In Lecture Notes in Computer Science, 3972, Springer-Verlag, pp. 110-115, 2006.

list of Symbols

$C(\cdot)$	Objective Function to be Minimized in a Neural Network
$f(\cdot)$	Desired Output
J	Resolution Level of Multiscaling Function
K	Number of Output Nodes
L	Index of the Scaling Functions of a Multiscaling Function
M	Number of Wavelons or Multiwavelons
N	Number of Input Nodes (Input Dimension)
P	Number of Training Patterns
U	Input Vector
V	Input Weight Matrix
Z	The Set of All Integers
C	Output of the Competitive Layer
E	Difference Between Desired Output and Actual Output (Error)
H	Iteration Number (Epoch)
I	Index of the Wavelon or Multiwavelon
K	Index of Output Nodes
R	Multiplicity of Multiwavelet
s	Index of the Training Samples
T	Translation
U	Scalar Input
V	Weight Between the Input Layer and the Hidden Layer
W	Output Weight

Y	Output
z	Inner Product Between the Input Vector and the Input Weight Vector
Δ	Difference Operator
Σ	Summation Operator
$\Phi(\cdot)$	Multiscaling Function
$\Psi(\cdot)$	Multiwavelet Function
α	Momentum Coefficient
ε	Training Error Threshold
η	Learning Rate
λ	Dilation
τ	Input to the Wavelet or Scaling Function
$\phi(\cdot)$	Father Scaling Function
$\psi(\cdot)$	Mother Wavelet Function
$\psi'(\cdot)$	Derivative of Wavelet Function

Table 1 Result of the BPAMW Classifier over ORL Database

Average Training MSE	Average Testing MSE	Average Recognition Rate
0.0034	0.0034	97.75

Table 2 Result of the BPW Classifier over ORL Database

Average Training MSE	Average Testing MSE	Average Recognition Rate
0.2490	0.9846	10.4167

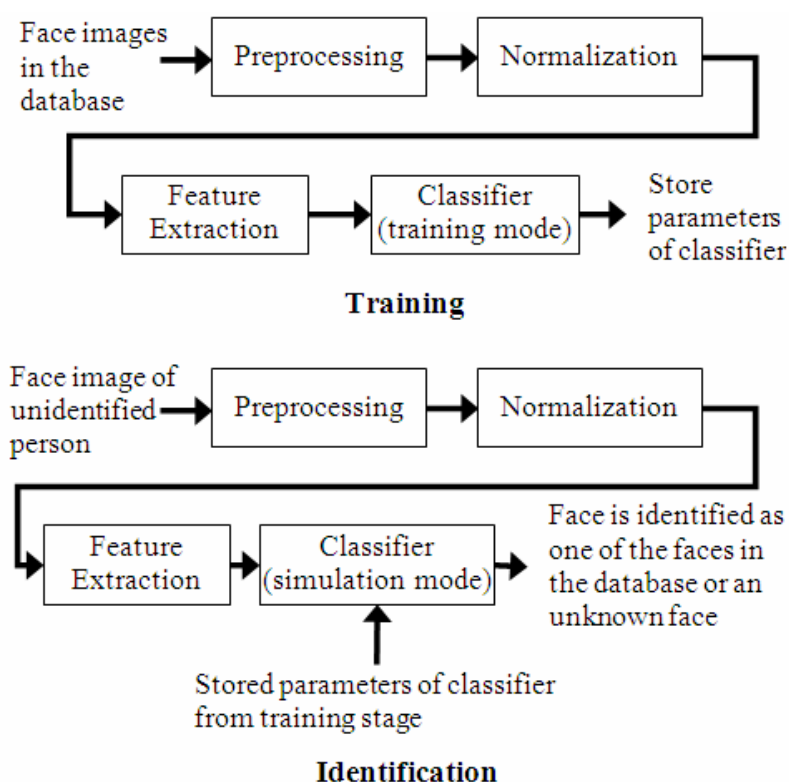


Fig. 1 The Proposed Face Identification System Block Diagram

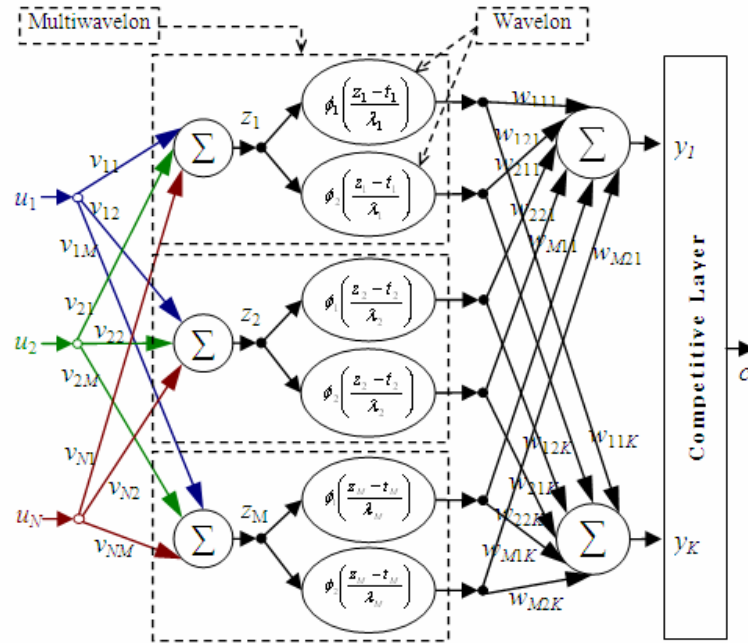


Fig. 2 The proposed BPAMW Classifier



Fig. 3 Sample Images from the ORL Face Database

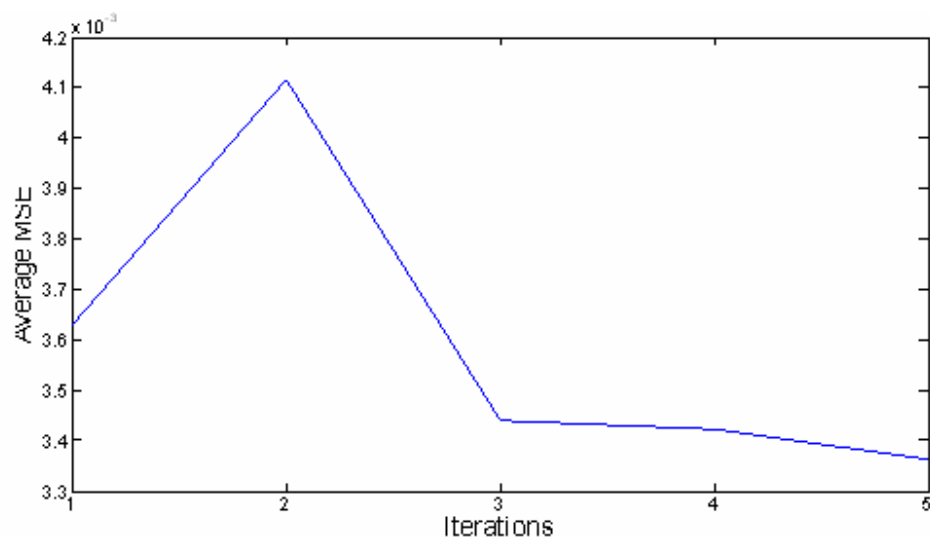


Fig. 4 BPAMW Classifier Performance over ORL Database: Average MSE vs. Iterations

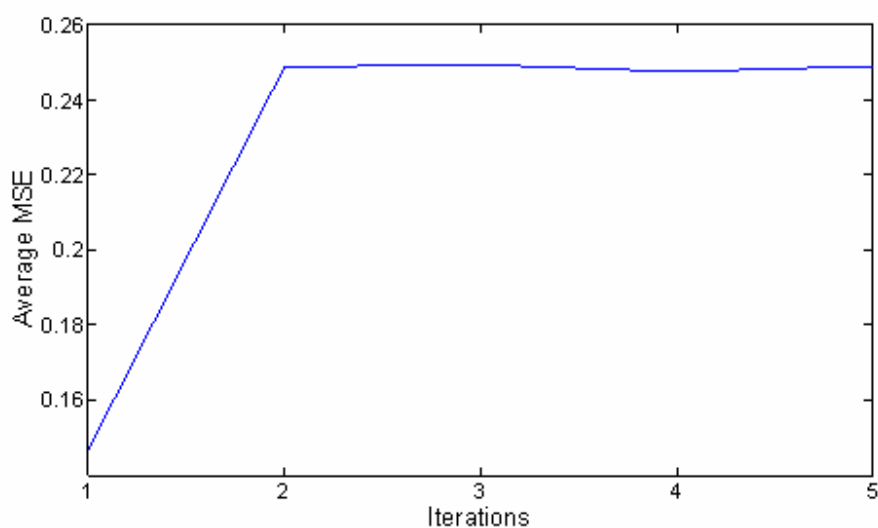


Fig. 5 BPW Classifier Performance over ORL Database: Average MSE vs. Iterations